Fundamental investigation of the transport properties of superacids in aqueous and non-aqueous media.

by

Sophia Suarez

A dissertation submitted to the Graduate Faculty in Physics in partial fulfillment of the requirements for the degree of Doctor of Philosophy, The City University of New York.

2004

UMI Number: 3115293

UMI Microform 3115293

ProQuest Information and Learning Company
300 North Zeeb Road
P.O. Box 1346
Ann Arbor, MI 48106-1346

This manuscript has been read and accepted for the Graduate Faculty in Physics in satisfaction of the dissertation requirement for the degree of Doctor of Philosophy.

1/26/2004 — Date
Professor Steve. G. Greenbaum, Ph.D., Chair of Examining Committee

1/26/2004 — Date
Professor Sultan Catto, Ph.D., Executive Officer

Professor Marten denBoer, Ph.D.

Professor Song H. Chung

Professor Tom Zawodzinski

Professor Godfrey Gumbs

Supervisory Committee

The City University of New York

Abstract

Fundamental investigation of the transport properties of superacids in aqueous and non-aqueous media.

by

Sophia Suarez

Advisor: Professor Steve G. Greenbaum

In the quest to develop more efficient energy providers one of the main focus of research has been on the improvement of ion transport. In lithium battery research this has led to the incorporation of various lithium salts, ceramics and plasticizers into the poly(ethylene)oxide (PEO) matrix, the polymer most used In Proton Conduction Membrane (PCM) fuel cell research this has led to the development of new membranes, which are designed with to replicate Nafion's (© DuPont) proton transport but also improve upon its deficiency of transporting intact fuel molecules and its dependence upon the presence of solvating water molecules.

To better understand the process of ion transport, NMR was used to investigate dynamic properties such as D (self-diffusion coefficient) and T_1 (spin-lattice relaxation time) of various proton and lithium ion-conducting systems. Ionic conductivity and viscosity measurements were also performed. The systems studied includes aqueous superacid solutions (trifluoromethanesulfonic (TFSA), para-toluenesulfonic (PTSA) and bis(trifluoromethanesulfonyl)imide (TFSI)); nano-porous (NP-) PCM's incorporating

various ceramics and 3M fuel/2M H_2SO_4 solutions; and $P(EO)_{20}LiBETI$ ($LiN(SO_2CF_2CF_3)_2$ composite incorporating SiO_2 ceramic nano particles.

The objective of the study of the superacid solutions was to determine the effect of concentration on the transport. It was found that beyond the ionic conductivity maximum, fluctuations in both D and T_1 supports the existence of local ordering in the ionic network, caused by the reduced solvent dielectric coefficient and increasing viscosity. Of the three superacids TFSA was the most conductive and most affected by reduced solvent concentration.

For the $P(EO)_{20}LiBETI$ composite the aim was to determine the effect of the ceramic on the ion transport of the composite in a solvent free environment. Results show that the ceramic causes only modest increase in the lithium transport below 90°C.

The objective in the study of the NP-PCM's was to determine the effect of the ceramic type and concentration on the proton and fuel transport through the polymer/acid system. Results show that the greater the surface area and concentration of the ceramic the greater the proton and fuel diffusion. The results were also shown to be fuel dependent, with dimethyl oxalate giving the lowest fuel diffusion.

Acknowledgements

This thesis would not have been possible without the help of both my family and people that I had the priviledge and pleasure of working with. First and foremost, I would like to thank Professor Steve Greenbaum for his guidance and encouragement over the years. He embodies the word mentor and I am fortunate to have been one of the lucky few to have received his attention. Through you I met a number of people who have contributed to who I am as a researcher and also as a person. My eternal gratitude to you, Professor.

To Dr. Phillip Stallworth, over the years I have bugged you for help with NMR and talked with you about life. You have been a great friend and I hope that though life is taking us on different paths as it should, that I may still call you a friend. To Professor Song Chung, thank you for always asking more questions than I have answers to because it makes me work harder. To Dr. Sabina Abbrent, from you I learned how to manage a laboratory. To Professor Tom Zawodzinski, thank you for the opportunity to work at Los Alamos, the experience gave me a view of what I wanted my career to be. To Professor John Fontanella, thank you for the opportunity to work at the U.S. Naval Academy and your support during my NRL interview.

To Dr. Michael Eikerling, thanks for making available preprints that provided invaluable help. To Dr. Emanuel Peled and his group, thanks for providing samples and for the opportunity to work with you. To Dr. Michele Vitadello, I enjoyed working with you. To Dr. Stefano Passerini, I would like to thank you for sharing your vast knowledge with me and for the opportunity to work with you. To Dr. Bajue, thank you for always

providing help and advise. To past and present lab mates: Illana, Elizabeth, Dr. Xiadong Guo, Eugene Mananga, Victor, and Dr. Jay Jayakodi. Thanks for all your help.

Last but not least, to my family – my mother Joy, brothers Odell and Shane, son Donyele, husband Brian, and grandparents Roy and Pearline, who may be gone but are not forgotten.

To all the groups that provided financial help: LSAMP, MBRS-RISE, and AGEP and a very special thanks to Dr. Gail Smith and Dr. Brathwaite. Your support over the years has been invaluable.

DEDICATION

This Thesis is Dedicated to

The Memory

of

My Grandfather Roy Suarez

for his love, support and lessons taught

Table of Contents

List of Tables

List of Figures

1. Introduction

The development of electrochemical devices such as fuel cells and batteries are dependent upon the transport properties of the ion-conducing polymer electrolytes available. Both fuel cell and battery applications require the use of ion-conducting polymer electrolytes with high ionic conductivity; good chemical, thermal and physical stability; and low cost.

For fuel cell applications the most widely studied proton conducting membrane (PCM) electrolyte is Nafion, a commercial polymer manufactured by DuPont, which is a perfluorosulfonated membrane with a hydrophobic fluorocarbon backbone and hydrophilic sulfonic pendant side chains. Nafion membranes are well known for having the above-mentioned properties, and as such are the benchmark for PCM development. However, their performance is dependent upon their hydration level. This results in a reduction in efficiency at ~ 80 - 100°C, which is the optimum operation temperature for PCM fuel cells being considered for use in electric vehicles and portable electronic devices. In addition to this, Nafion has a high cost, and is very permeable to methanol. The use of Nafion membranes are therefore limited to fuel cell application where cost is not an issue and hydrogen can be used as the fuel. Because of this, new membranes are being sought to replace Nafion.

The most used polymer in lithium battery applications is poly(ethylene)oxide (PEO) incorporating various lithium salts. The resulting electrolytes however, are known to have poor mechanical properties and low ionic conductivities at optimal operating temperatures desired for lithium polymer batteries. There have been numerous efforts directed at improving these deficiencies by the introduction of nano-size ceramic

particles and lithium salts having large anions, into the polymer matrix. The result of such incorporations has led to improvement in both mechanical stability and the ionic conductivity. There are however, disagreements in the literature regarding the latter factor, with contradicting reports on the precise effect of the ceramic filler on the ionic conductivity. In this investigation $LiN(SO_2CF_2CF_3)_2$, commonly known as LiBETI and the ceramic SiO_2 is incorporated into the PEO polymer matrix. LiBETI is the Li- salt form of the superacid $HN(SO_2CF_2CF_3)_2$. The purpose of this study is to investigate the effect of the ceramic filler on the transport properties of the composite polymer in a solvent free environment.

1.1 Fuel cell background

Fuel cells are electrochemical devices, which provide energy through the direct conversion of chemical energy into electricity. Fuel cells have been around for over a century and a half since British physicist William Grove discovered them in 1839. Grove utilized four cells, each containing hydrogen and oxygen, to power the electrolysis of water. Fuel cells became popular in the 1950's when NASA used them as power sources in space missions. From the success of NASA's endeavors, industries became interested in the commercial viability of fuel cells but encountered economic barriers.

The development of electrochemical devices such as batteries and fuel cells are geared towards replacing fossil fuel combustion. Compared with batteries, fuel cells have several advantages including lighter weight, quick refueling and longer range. Fuel cells are grouped according to their electrolytes, of which there are five types: solid

oxides, phosphoric acid, molten carbonate, alkaline and the proton conduction membrane (PCM) or solid polymer electrolyte (SPE).

Of the five the most applicable in portable communication devices and the transportation industry is the PCM or solid polymer electrolyte (SPE) fuel cell. As mentioned previously the PCM most commonly used is *Nafion* (DuPont), which is known for its efficiency as an electrolyte, it's high cost, and its permeability to methanol, a possible fuel. Fuel permeability in PCM's is directly related to crossover, which refers to the transport of the intact fuel molecules through the membrane to the cathode compartment, where they react with oxygen to produce water, carbon dioxide and heat. This results in the consumption of fuel without the production of electricity, thereby reducing the overall efficiency of the fuel cell.

Recent development of new membranes is focused on reducing the overall cost and fuel permeability of the fuel cell, thereby increasing cell efficiency. New generation of membranes must also have high proton conductivity and be relatively insensitive to metal-ion impurities, thus making it possible to use low cost catalysts and housing materials in the fuel cell. To aid in improving the ionic conductivity of new membranes, various methods of development are employed. One method involves the use of additives such as inorganic oxides and aqueous acid solutions. The presence of inorganic oxides solvate the protons and provide the necessary hydrogen bonding to facilitate proton transport whereas the use of acids increase the proton population, both methods results in an improvement in the ionic conductivity.

In an attempt to understand the role acids play when incorporated into PCM's, it is necessary to understand the transport properties of the acids themselves. Investigating

the fundamental transport properties of various acids is the focus of this thesis. In addition to this, various nano-porous proton conduction membranes (NP-PCM's) incorporating the addition of both inorganic oxides and acid solutions will be studied, with focus on their proton dynamics. The final study of this thesis focuses on the PEO polymer matrix containing the LiBETI ($LiN(SO_2CF_2CF_3)_2$ salt and the effect of SiO_2 nano particles on the dynamics of the composite polymer.

1.2 Superacids

A superacid is described as a system that is stronger than 100% sulfuric acid [1]. The relative acidic strength of a superacid cannot be described by the pH scale. Instead, it is indicated by the Hammett acidity function H_o, where for the following reaction:

$$HA + B \rightarrow HB^+ + A^- \quad (1)$$

we have [2]:

$$H_o = pK_{BH+} - \log[BH^+]/\log[B] \quad (2)$$

In the above reaction, B represents the weak base being protonated by the superacid HA. The term pK_{BH+} is $[B][H+]/[BH^+]$, and the $[BH^+]/[B]$ ratio can be determined spectroscopically for suitably chosen indicator acid-base pairs. In an ideal case the protonated base should not interact with the anion A^- formed, as the negative charge is completely delocalized on the anion. In general, H_o may be ≤ -12 for superacids. Some very common superacids includes: $HClO_4$ (perchloric), HSO_3F (fluorosulfonic), HCF_3SO_3 (trifluoromethanesulfonic), and $ClSO_3H$ (chlorosulfonic).

In general, superacids are characterized by low melting points, high boiling points, high dielectric constants, and high $-H_o$, as indicated in Table 1.1 [3]. They are

also very hazardous, being both volatile and toxic (perchloric acid in concentrations above 90% by weight, becomes explosive as it reaches its boiling point). This, in addition to the average cost per gram makes it difficult to perform experimental work on such systems.

Property	**$HClO_4$**	**$ClSO_3H$**	**HSO_3F**	**CF_3SO_3H**
Mp (°C)	-112	-81	-89	-34
bp (°C)	110	151-152	162.7	162
Density g/cm^3 (25 °C)	1.767	1.753	1.726	1.698
Viscosity (cp) (20°C)	---	3.0	1.56	2.87
Dielectric constant	---	60 ± 10	120	---
Specific conductance (20 °C) 1/ohm·cm	---	$0.2 - 0.3 \times 10^{-3}$	1.1×10^{-4}	2.0×10^{-4}
$-H_o$	≈ 13.0	13.8	15.1	14.1

Table 1.1. The physical properties of various Bronsted oxy-superacids.

A Brontsed acid is one that can donate a proton whereas a Lewis acid is one that can accept electrons. Examples of Bronsted superacids are those listed in Table 1.1, whereas Lewis superacids includes SbF_5 (antimony pentafluoride), NbF_5 (niobium pentafluoride), AsF_5 (arsenic pentafluoride), and TaF_5 (tantalum pentafluoride). Much stronger acids with Ho < -15 can be obtained by the combination of a Bronsted and Lewis superacids. The famous Magic Acid, which is a mixture of the Lewis SbF_5 and Bronsted

HSO_3F acids, has a $-H_o$ of 26.5 for 90% SbF_5 content by weight [3]. Magic acid is used in the petroleum industry to break down raw petroleum into high-octane fuel.

The Bronsted superacids mentioned so far are all oxyacids. The anions of these oxyacids, namely ClO_4^-, $CF_3SO_3^-$, FSO_3^-, and $ClSO_3^-$ are all stable species. However, in the presence of strong electrophiles, they facilitate strong interactions through their oxygen and sometimes, fluorine atoms. This interaction often leads to oxidation and fluoride ion transfer. In an attempt to combat such undesirable effects in oxy-superacids, a new breed of superacids was developed. These include $(CF_3SO_2)_2NH$ and $(CF_3SO_2)_2CH$, the parent members of the more general form $(R_fSO_2)_2NH$ and $(R_fSO_2)_3CH$, where R_f represents fluorinated groups. In these acids the negative charge of their anions is delocalized over more atoms than in HCF_3SO_3, thereby making them less reactive and more stable [4].

While there are many applications of superacids, the focus of this thesis is on their protonating ability, specifically their transport properties resulting from their protonation of water as a solvent. The use of superacids for their protonating abilities has led to their incorporation into polymer electrolytes such as Nafion and poly(ether) ketone ketone (PEKK) membranes where they enhance the ionic conductivity of such systems, thereby allowing their use as electrolytes in proton conduction devices such as fuel cells.

The superacids investigated in this study are: trifluoromethanesulfonic (TFSA), bis(trifluoromethanesulfonyl)imide (TFSI), and para-toluenesulfonic (PTSA), whose chemical structures are depicted in Figure 1-1.

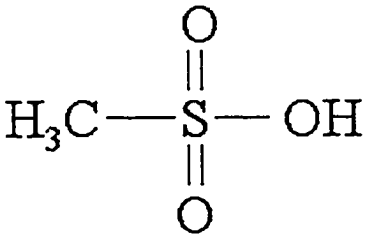

TFSA

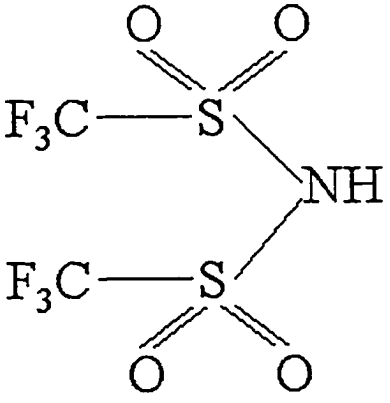

TFSI

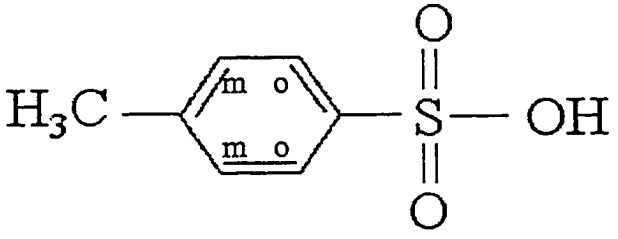

PTSA

Figure 1-1. The chemical structure of the superacids: TFSA, TFSI, and PTSA respectively.

1.2.1 Model of Aqueous solutions

Ions in aqueous solution are said to consist of a primary and secondary solvation shell, a disordered or fault zone, and the bulk solvent regions as depicted in Figure 1-2 [5]. The primary solvation shell of the ion contains water molecules directly interacting with the ion. The secondary solvation shell also consists of water molecules, which interact indirectly with the ion through hydrogen bonds in the primary solvation shell. The fault zone is disordered and separates the ordered regions A and B from D. The bulk solvent consists of the remaining water molecules not participating in solvating the ions. This picture only applies to very dilute 1:1 electrolytes where the dielectric permittivity of the bulk water is high to provide the necessary shielding.

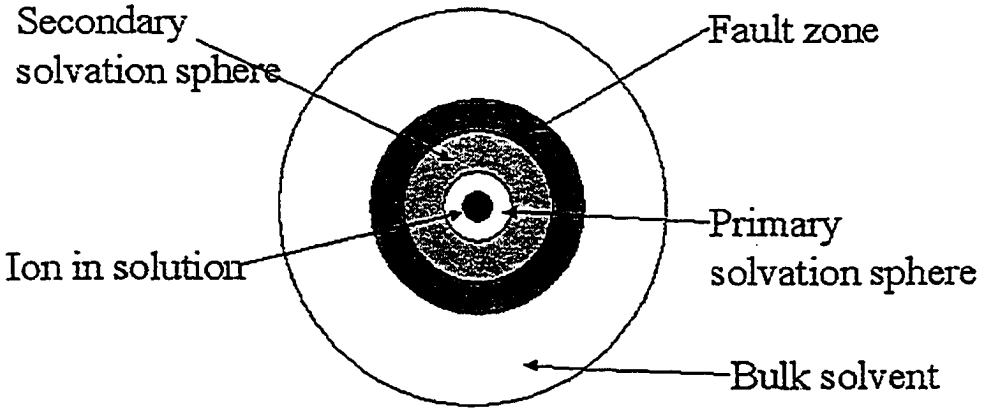

Figure 1-2. The environment of the ion in solution.

As the concentration increases however, there is a reduction in both ion-ion separation distances and the dielectric permittivity of the bulk and solvating water molecules. This result in an increase in the electrostatic interactions and leads to the formation of ion pairs, ionic clusters, and aggregates, just to name a few.

1.2.2 NMR studies of aqueous solutions.

Nuclear Magnetic Resonance (NMR) spectroscopy is one of the primary tools used in the investigation of ionic solutions. The information obtained from NMR – chemical shifts, and linewidths - provides direct information about the ion-solvent interactions. One of the most important pieces of information is the ion solvation number, which is the number of coordinating solvent molecules. To obtain this information the NMR spectrum must consist of separate peaks for each chemically inequivalent nuclear environment. Because NMR yields nuclei population, the ratio of the areas of the peaks yields the ion solvation number [5]. In the event of slow exchange of solvent molecules, it is possible to obtain separate NMR signals corresponding to the presence of solvent molecules in the various environments. In order to observe separate peaks a nucleus must remain in a particular environment for a time greater than the inverse of the nuclei's resonant frequency. This time could be on the order of milliseconds and corresponds to slow exchange of the solvent molecules. In most cases however, the NMR study of solutions yields a single line, corresponding to fast exchange on the NMR timescale. In this case a direct measure of the primary solvation number is unobtainable.

In general, for diamagnetic cations, the ^1H chemical shifts of the primary cation water and the 'bulk' water are on the order of 100 Hz apart. For paramagnetic cations, the difference is thousands of hertz [5].

1.3. Nafion

Nafion membranes are the most investigated polymer electrolytes. They were developed by E.I. du Pont de Nemours and Co. in the 1960's, and have since been made available in various forms for study and application as electrolytes in fuel cells. Structurally, Nafion consists of a polytetrafluoroethylene (PTFE) backbone with pendant sidechains of perfluorinated vinyl ethers, which terminate in sulfonic (SO_3H) acid groups, as shown in Figure 1-3.

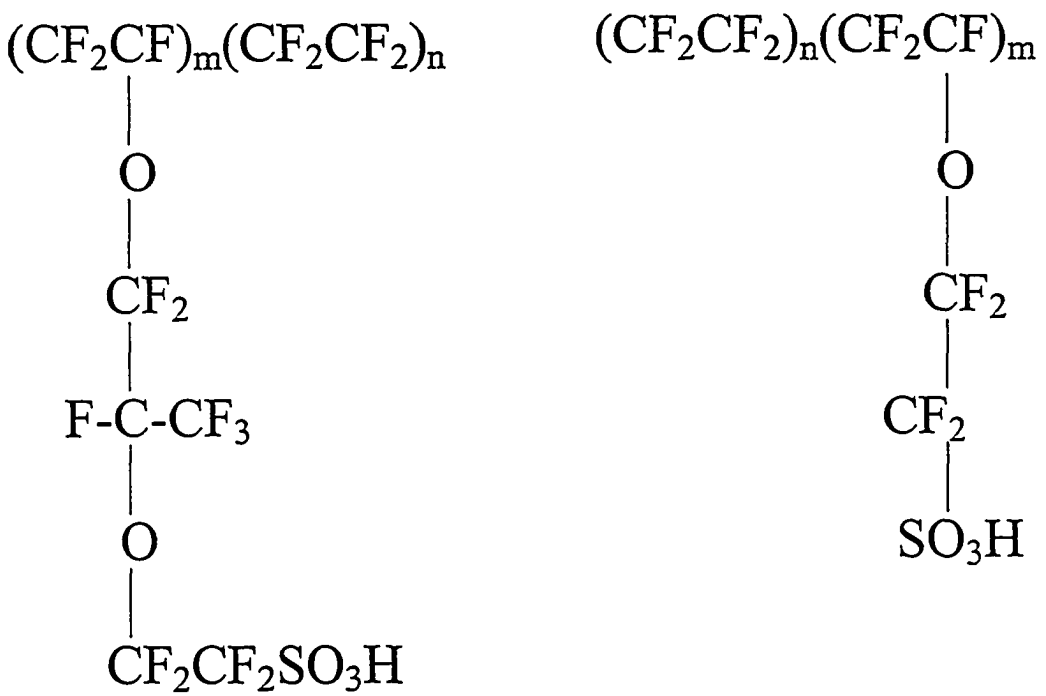

Figure 1-3. The general formula of Nafion in acid form.

For commercial use, m is usually one and n varies from 5 to 11. This results in an equivalent weight (EW) of about 1000 to 1500 grams of dry hydrogen ion form polymer per mole of exchange sites. As such the membranes are often named according to their EW: Nafion 117 (EW = 1100), and Nafion 105 (EW = 1000). The greater the EW, the lower the ionic conductivity, and the higher the morphological stability.

Nafion membranes are able to absorb large amounts of water and other solvents (10-50% by weight), depending upon their EW, counterion form, and temperature of equilibration. This ability both supports and hinders their performance when used as electrolytes in fuel cells. They exhibit thermal stability up to about 200°C, (depending on counterion form), and are also chemically and physically stable.

There are numerous models of the Nafion structure, however there is no universal agreement on the validity on any of them. The most prominent model put forth is the Ionic Cluster-Network by Gierke in 1977 [6]. Based upon the existence of ion clustering in perfluorinated sulfonate ionomers reported by Eisenberg and Yao in 1975 [7] and experimental evidence from various techniques, including but not limited to NMR spectroscopy, infrared (IR) spectroscopy, and X-Ray scattering experiments, Gierke proposed the existence of almost spherical clusters (3nm diameter), interconnected by short, narrow channels (1nm diameter) in the fluorocarbon backbone network. Since the inception of this model, several corrections have been put forth, for example it has been said that the clusters are not spherical in shape and are actually smaller than suggested by Gierke [8]. In addition to this, ^{19}F NMR spectroscopic evidence has supported the existence of a three-phase system in which the fluorocarbon backbone consists of both

crystallites and amorphous regions of roughly equal amounts, and ionic hydrophilic clusters not necessarily spherical in shape [9].

1.4 Nano Porous-PCM's

The membranes investigated in this research were new nano-porous proton conduction membranes (NP-PCM's), developed at Tel Aviv University by Emanuel Peled's group for use in fuel cells, in particular the direct oxidation fuel cell (DOFC). The DOFC is a device in which an aqueous solution of the organic fuel rather than hydrogen is fed directly into the fuel cell. Advantages of the DOFC include reduced weight, volume and cost compared with indirect fuel cells in which the fuel is reformed into hydrogen before use. The most popular DOFC employs methanol as the fuel. However, as mentioned previously methanol easily permeates PCM's used as electrolytes therefore reduces the cell efficiency. In an attempt to improve the efficiency of the DOFC, replacement membrane and fuels were being sought.

In order to improve the efficiency of the DOFC, it is necessary to: (1) use less permeable proton conduction membranes, and (2) replace methanol with an alternative fuel. Because of this, extensive effort has been directed towards finding new low-cost solid polymer electrolytes with high ionic conductivity, and low fuel permeability. New membranes must also have physical, chemical and thermal stability, and be relatively insensitive to metal-ion impurities (as the presence of such impurities reduces the membrane's ionic conductivity), thus making it possible to use low cost catalysts and hardware materials.

The NP-PCM's consists of a poly(vinylidene) fluoride (PVDF) matrix, high surface area inorganic oxides such as silicates, aluminates, or titanates, and an aqueous acid that fills the nano-pores [10]. When employed as electrolytes in DOFC's utilizing various organic fuels, the NP-PCM's gave lower fuel permeability and higher proton conductivities than *Nafion*. In addition to this the NP-PCM's also cost less and are relatively insensitive to metal-ion impurities, thus making it possible to use less expensive catalysts and housing materials for the DOFC. Properties as compared with *Nafion* are given in Table 1.2 [11].

The fuels investigated were dimethyl oxalate (DMO), ethylene glycol (EG) and methanol (MeOH). DMO is a solid fuel, is relatively insoluble in water below 30°C, has a high boiling point and yields 14 electrons for complete oxidation reaction. EG, also has a high boiling point, and yields 10 electrons for complete oxidation reaction. EG is closely related to the well-known antifreeze in the automotive industry. As such it enjoys an already existing distribution infrastructure, and therefore its adaptation as a fuel is relatively easy.

	Nafion TM117	**NP-PCM**
Cost ($/m^2)	780	4 + acid cost
Typical pore size (nm)	3	1.5 – 3
MeOH crossover (mA/cm^2)	125 – 150 at 60°C 250 – 300 at 90°C	12 at 60°C 30 at 95°C
Acid	-SO_3H fixed to the polymer	Various dissolved in aqueous solution
RT conductivity (S/cm)	0.1	Up to 0.45

Table 1.2. NP-PCM's properties and a comparison of its properties to *Nafion*.

These fuels were chosen based on their reported 94 - 95% direct oxidation in the DOFC [12]. The goal of this investigation was to study the mobility of water and the methyl (CH_3) or methylene (CH_2) group associated with the fuel, in new proton conducting membranes equilibrated in aqueous solutions of 2M fuel in 3M acid. This mixture was chosen because of its similarity to that used in actual DOFC's, except that the fuel concentration has been doubled so as to allow visibility by NMR spectroscopy.

1.5. Lithium polymer electrolytes

Today's society demands the availability of energy to accommodate their portable communication, entertainment and computing needs. Currently this energy is made available mostly by lithium ion (Li-ion) batteries. In general a battery is comprised of several electrochemical cells that are connected in series or parallel depending on the voltage requirement. A battery is similar to a fuel cell in that it consists of a positive and negative electrode, separated by an electrolyte. Compared with other batteries Li-ion batteries have higher energy densities and offers wider range of application.

Present-day electrolytes are organic solutions with dissolved salts that allow fast ion transport between the electrodes. There is a large worldwide effort to replace these by solid polymers, leading to the Li-solid polymer electrolyte (Li-SPE) batteries. The most used polymer electrolyte is polyethylene oxide (PEO) incorporating various lithium salts. The main goal of such a merger was to improve the ionic conductivity while lowering the composite's melting temperature. Salts used includes $LiCF_3SO_3$, $LiClO_4$, more recently $Li(CF_3SO_2)_2N$ (LiTFSI) and $LiN(SO_2CF_2CF_3)_2$ (commonly known as LiBETI). While the addition of such salts improved the ionic conductivity there were

compromises in the mechanical stability. To improve the mechanical stability most efforts have been directed at the introduction of nano-size inorganic particles into the composite polymer/salt system. In addition to improving the mechanical stability, it was reported that they increase the Li transference number [13-16].

1.6. Effect of ceramic fillers on PEO polymer matrix.

Since the first introduction of ceramic fillers into polymer electrolytes by Weston and Steel [13], several reports have indicated improvements in the ionic conductivity, due to the enhanced segmental motion of amorphous regions, and interfacial stability of PEO-based polymer electrolytes by the incorporation of nano-size ceramic fillers [14-18].

In this investigation the ceramic chosen was SiO_2, which has been widely used because it has excellent merits both with regard to structure and large surface areas, which in turn may lead to a high disorder of the polymer chains and high ionic mobility. In particular, the addition of modified SiO_2 particles with different surface groups in polymer electrolytes has revealed a considerable enhancement in ionic conductivity [19-21].

Walls et al. [20] have demonstrated high conductivities at room temperature and stable interfaces with lithium metal by the addition of fumed silica to low molecular weight poly(ethylene glycol) dimethyl ether PEGDME-LiX electrolytes. The conductivity, however, showed a tendency to decrease above 20 wt.% fumed silica, and no discernable changes in the conductivity of polymer electrolytes with different types of fumed silica were observed. Recently, Chung et al. [17] have reported the effect of the addition of nano-size TiO_2 ceramic fillers on the ionic conductivity and cation transport

properties in $P(EO)_8LiClO_4$ polymer electrolytes. The enhancement of the ionic conductivity has been attributed to a weakening of the polyether oxygen-cation interaction. The NMR investigation showed a surprisingly higher degree of crystallinity in the TiO_2-containing $P(EO)_8LiClO_4$ electrolyte. This is in strong contrast with other reports in which the enhanced conductivity of filler-containing polymer electrolyte was attributed to the higher degree of disorder resulting from the prevention of local PEO chain reorganisation. More recent results on PEO-based polymer electrolytes prepared by a solvent-free procedure [22] showed only a very modest effect on the ionic conductivity by the incorporation of the filler. In addition to this, Appetecchi et al. [23] reported no substantial enhancement in the conductivity of PEO-$LiCF_3SO_3$ electrolytes with 5 or 10 wt.% of nanometric silica and alumina additives, prepared in solvent-free conditions.

In view of these conflicting results, the question of the effect of the filler's interaction with the polymer matrix and the ions needs to be addressed. Are these effects due to the filler itself or to the solvent and/or other impurities trapped on the filler interfaces? Nanosize fillers are characterised by very high surface areas with a large number of active sites, i.e., unsaturated bonds on the particle surface, on which polar molecules, for example solvent molecules, can be strongly adsorbed. To investigate this issue we have performed an extensive NMR investigation of the effect of nanosize silica on the properties of $P(EO)_{20}$LiBETI polymer electrolytes.

1.7. Mechanisms of proton transport.

The mechanisms of proton transport have been the focus of numerous experimental and theoretical studies [24-29]. From these and other studies it has been accepted that there are two main mechanisms of proton transport, namely the Vehicle [30] and Grotthuss mechanisms [31]. The first mechanism involves the translational assisted motion of protons by vehicles such as solvent molecules. The second mechanism involves the transport of protons within hydrogen bonds from one vehicle to another, and involves the structural reorganization of the molecules to facilitate the proton transport. Both mechanisms are dependent on the presence and relative strength of hydrogen bonds.

The more prominent of the two is the Grotthuss mechanism, which is made possible by hydrogen bonds breakage and formation in the first and second solvation spheres respectively. The form the solvated proton takes during this process has been and is still under discussion. Bernard and Fowler [32] suggested proton hopping from one H_3O^+ species to a freely rotating nearest-neighbor water molecules. This model has been deemed unfavorable based upon the fact that water is not a free rotator but is instead involved in tetrahedral hydrogen bonds [33-34]. Other suggestions have the proton as part of either the Zundel ($H_5O_2^+$) or Eigen ($H_9O_4^+$) ion. Quantum Molecular Dynamics (MD) simulation [35-36] of an extra proton in water has the resulting complex fluctuating between the Zundel- and Eigen- ions. High pressure mass spectrometry [37] has provided evidence of proton solvation by many water molecules and of the most probable structure of the hydrated proton, being the Zundel ion solvated by four weakly bonded water molecules, as shown in Figure 1-4.

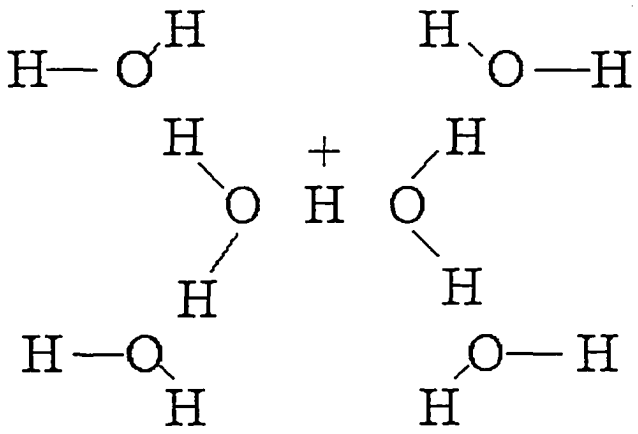

Figure 1-4. The solvated Zundel ion.

More recent MD simulations [26] investigating one proton in the presence of 100 water molecules at various temperature showed that at 300K the proton is more likely to be coordinated as the Zundel ion, whereas at higher temperatures the Eigen ion becomes more favorable. While it is outside the scope of this thesis to provide information on the specific form of the solvated proton structure, the general behavior governing the solvation of the protons in aqueous solutions, and how it relates to the proton transport mechanism is one of the goals.

Chapter 2. Methods of Investigation - Theory

2.1 Nuclear Magnetic Resonance (NMR) spectroscopy

2.1.1 Theoretical

Nuclear Magnetic Resonance (NMR) is a powerful non-invasive technique used for investigating the structural and dynamical aspects of molecular systems. The basis of this technique is the use of nuclei possessing magnetic moments as direct probes of the system in question. To be used as probes, nuclei must interact with static magnetic fields. This interaction is dependent upon an intrinsic property called the spin angular momentum, represented by operator **I**. The first observation of NMR is credited to two groups: Purcell, Torrey and Pound at Harvard and Bloch, Hansen and Packard at Stanford. Both groups in 1946 reported independently their discovery of the NMR detection of protons in bulk materials such as water and paraffin. For this discovery, Bloch and Purcell were both awarded the 1952 Nobel Prize in Physics. While NMR has long been associated with the molecular beam experiments of the Rabi group at Columbia University (during the 1930's), it is recognized more as a tool described above. More information on the NMR phenomenon can be found in the following references [38-40].

In this section the classical approach of NMR will be presented. According to classical mechanics a moving charge produces a current, which itself produces a magnetic field. The magnetic moment of the charge represented by μ is related to the current i produced and the area A swept out by:

$$|\mu| = iA/c \qquad \text{Eq. (1)}$$

where c is the speed of light. This magnetic moment is related to the angular momentum **L** by the relation:

$$\mu = \gamma \mathbf{L} \qquad \text{Eq. (2)}$$

where γ is the gyromagnetic ratio of the nuclei. In the presence of a static magnetic field **B**, the moment will experience a torque given by:

$$\tau = \mu \times \mathbf{B} \qquad \text{Eq. (3)}$$

which may be re-written as the following using the fact that torque is the time derivative of the angular momentum **L**:

$$\frac{d\mathbf{L}}{dt} = \mu \times \mathbf{B} \qquad \text{Eq. (4)}$$

Using the relationship between μ and **L** given in Eq. (2), and taking **B** to be along the z-axis, the equation of the motion of in Eq. (4) may be solved to give:

$$\begin{aligned} d\mu_x/dt &= \gamma\, \mu_y B \\ d\mu_y/dt &= -\gamma\, \mu_x B \\ d\mu_z/dt &= 0 \end{aligned} \qquad \text{Eq. (5)}$$

The three components of μ in Eq. (5) suggest a picture of a vector μ rotating about **B** with angular frequency $\omega = -\gamma \mathbf{B}$, tracing out a cone as depicted in Figure 2-1. This frequency ω is known as the Larmor frequency and is given in units of rad/s. Since in NMR one is concerned with a large number of spins as opposed to a single one, it is necessary to introduce the magnetization **M**, which is simply the vector sum of the ensemble of moments within the spin system's volume and is given by: $\mathbf{M} = \Sigma\mu_i$.

Once in the static magnetic field the magnetization μ will have available to it various orientations of energy levels, according to the relation:

$$E = -\gamma \mathbf{L} \cdot \mathbf{B} \qquad \text{Eq. (6)}$$

The energy of μ is dependent upon the magnitude of the field and its orientation with respect to the field. The resulting interaction between the static field and the moment is called the Zeeman interaction. Perturbation of the spin system from equilibrium and the processes by which equilibrium is once again obtained is the basis of NMR as it yields information about the spin system's interactions and environment, both on a local and long-range scale.

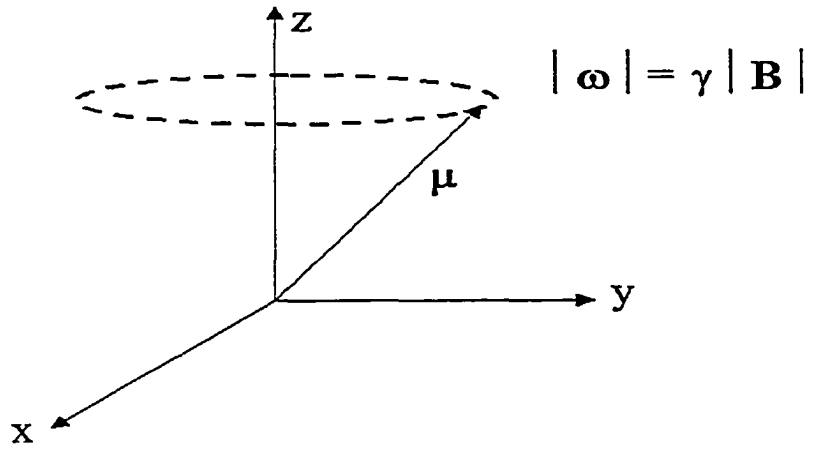

Figure 2-1 The Larmor precession of a magnetic moment in a static magnetic field.

2.1.2 Relaxation

To observe NMR signals, the spin system must absorb electromagnetic energy (in the radio frequency range) that allows transitions between the energy levels. Equilibrium is achieved through the process of relaxation, which is due to the interaction between the

spins and their environment. There are two main types of relaxation: longitudinal or spin-lattice (T_1), and transverse or spin-spin lattice (T_2). If one considers the spin system as isolated thermodynamically, then upon the absorption of 'heat' energy from the rf pulse, the temperature of the spin system will increase. To restore equilibrium to the system there must be a removal of this excess heat to the lattice bath. The time constant T_1, characterizes the rate of return to equilibrium of the z-component of the magnetization after perturbation. The time constant T_2, determines the time it takes for the x and y components of the magnetization to attain equilibrium after perturbation.

In order to include the relaxation effects on the magnetization Felix Bloch proposed that simple first order kinetics with time constants T_1 and T_2 be included in the equations of motion, known as the Bloch equations and given in Eq. (5). The result is the following:

$$\frac{dM}{dt} = -\frac{M_x}{T_2}i - \frac{M_y}{T_2}j - \frac{M_z - M_o}{T_1}k + \mathbf{M} \times \gamma\mathbf{B} \qquad \text{Eq. (7)}$$

whereby the components of **M** are:

$$dM_x/dt = \gamma M_y B - (M_x/T_2)$$

$$dM_y/dt = -\gamma M_x B - (M_y/T_2) \qquad \text{Eq. (8)}$$

$$dM_z/dt = (1/T_1)(M_z - M_o)$$

Solution of the above equations yields the behavior of M_z as that of an exponential approach towards equilibrium, as shown in Figure 2-2. Solution of the x and y components of **M** are obtained with the aid of the raising and lowering magnetization operators, and are observed to be oscillating about the static field at the Larmor

frequency. In the rotating reference frame however (to be described later), the oscillations of M_x and M_y are observable, and are shown in Figure 2-3.

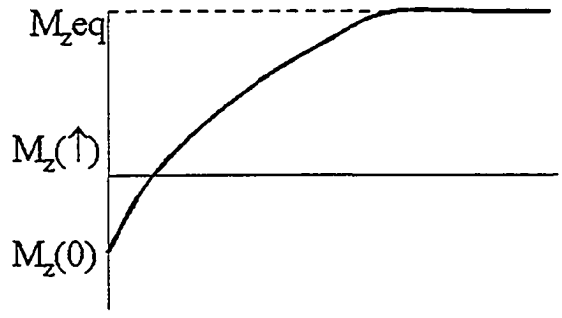

Figure 2-2. Relaxation of the longitudinal magnetization.

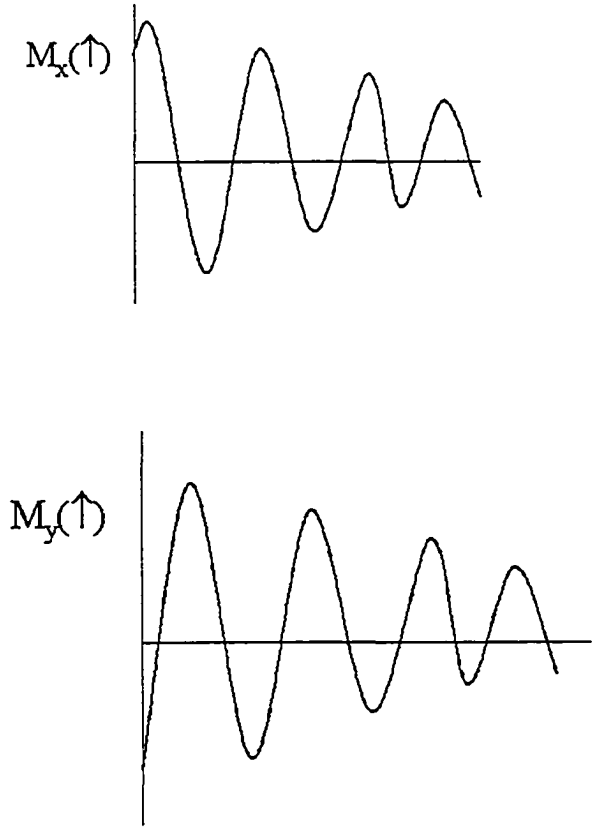

Figure 2-3. Relaxation of the transverse components of the magnetization.

2.1.3 The rotating frame

To describe the observation of NMR signals it is useful to refer to the rotating frame rather than the laboratory frame. This is necessary so as solve the equations of motion of **M** in the static **B** field, as given by Eq. (5) with μ replaced by **M**. The laboratory and rotating frames are indicated by x-y-z, and x'-y'-z', axes respectively, as shown in Figure 2-4.

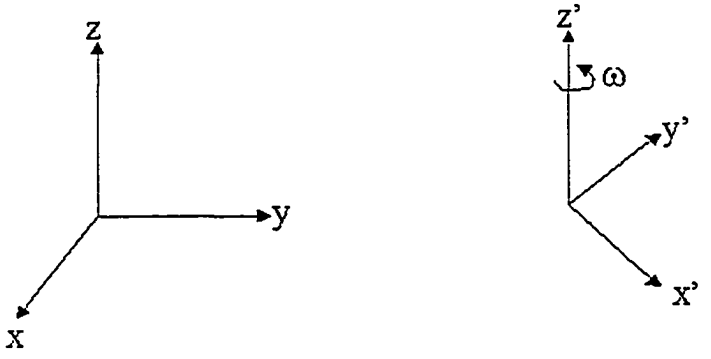

Figure 2-4. Laboratory and rotating reference frames.

In a rotating frame moving at frequency ω, it can be shown that the vector **M** is given by:

$$\partial M / \partial t = \gamma \mathbf{M} \times \mathbf{B} + \omega \times \mathbf{M} = \gamma \mathbf{M} \times (\mathbf{B} + \omega/\gamma) \qquad \text{Eq. (9)}$$

If the angular frequency of the rotating frame coincides with the Larmor frequency, the magnetization will be stationary with respect to the rotating frame.

In order to perturb the magnetization a time-varying radio-frequency (rf) field - $\mathbf{B}_1$, must be applied. $\mathbf{B}_1(t)$ must be perpendicular to the static field and have constant magnitude. This field may be taken as $\mathbf{B}_1 = 2\,|\mathbf{B}_1|\cos(\omega t)$ directed along the x-axis, and may be decomposed into two counter-rotating fields. In the presence of such a field the total external magnetic field becomes:

$$\mathbf{H} = (\mathbf{B})_z + 2\,|\,\mathbf{B_1}\,|_{x'}\cos(\omega t) \qquad \text{Eq. (10)}$$

where **H** represents the sum of the magnetic fields. One component of the rotating field will be static while the other component will rotate with frequency 2ω, and can be ignored, as it does not satisfy the resonance condition. With this, Eq. (9) becomes:

$$\partial M / \partial t = \gamma\,\mathbf{M} \times [(|\,\mathbf{B_o}\,| + \omega/\gamma)_{z'} + |\,\mathbf{B_1}\,|_{x'}] = \mathbf{M} \times \gamma\,\mathbf{H_{eff}} \qquad \text{Eq. (11)}$$

where $\mathbf{H_{eff}} = (|\,\mathbf{B}\,| + \omega/\gamma)_{z'} + |\,\mathbf{B_1}\,|_{x'})$.

When $\omega_o = -\gamma B_o$, the effective magnetic field becomes $\mathbf{H_{eff}} = |\,\mathbf{B_1}\,|_{x'}$. Including the effective field and the equation of motion for the relaxation of **M** in Eq. (7), gives:

$$\partial M / \partial t = \mathbf{M} \times \gamma\mathbf{H_{eff}} - (M_x x' + M_y y')/T_2 - (M_z - M_o)/T_1\, z' \qquad \text{Eq. (12)}$$

A change in the orientation or angular displacement θ of **M** by the application of an rf field, is given by given by:

$$\theta = \gamma\,|\,\mathbf{B_1}\,|\,t_p \qquad \text{Eq. (13)}$$

where t_p is the time during which the rf field is applied. The excitation frequency range and t_p are indirectly related, and therefore for a large frequency range, one needs to apply as short a t_p as possible.

If **M** is rotated through $\theta = 90^{\circ}$, **M** will be aligned in the x'-y' plane and precesses about **B** in the laboratory frame at the Larmor frequency ω_o. As shown in Figure 2-5, the orientated **M** will dephase in the x'-y' plane while simultaneously re-growing in the z-z' direction. The reasons for the decay back to equilibrium form the bulk of NMR analysis.

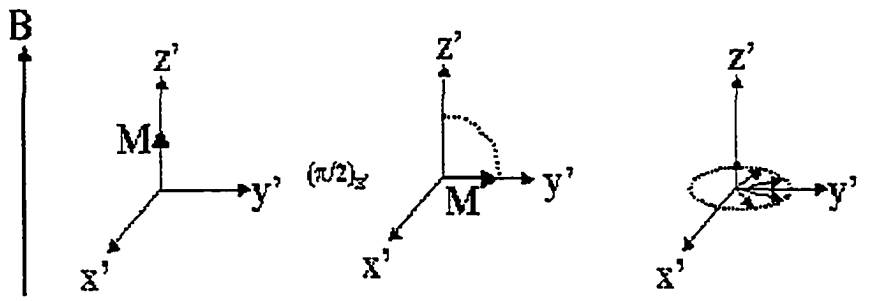

Figure 2-5. Effect of rf pulse on **M**.

A receiver coil oriented in the x'-y' plane receives a signal, which is called a free induction decay (FID), which refers to the time decay of **M** in the absence of the rf field. This FID (*f(t)*) may be Fourier transformed from the time domain to the frequency domain to get the desired information, which is a spectrum ($F(\omega)$), both of which are shown in Figure 2-6 and given by the following equation:

$$F(\omega) = \int_{-\infty}^{+\infty} f(t) e^{-i\omega t}\, dt = v - iu \qquad \text{Eq. (14)}$$

where u and v are the real and imaginary parts of the spectrum.

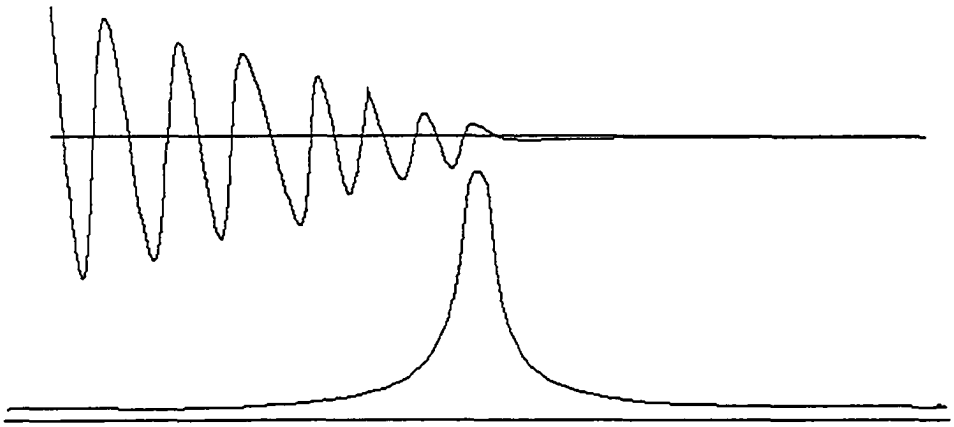

Figure 2-6. Relationship between the FID (top) and the resulting absorption spectrum (bottom).

2.1.4 Quantum Mechanics view

The nuclear Zeeman Hamiltonian and is given by the following equation:

$$H_Z = -\mu \cdot \mathbf{B} = -\gamma m_I \hbar B \qquad \text{Eq.(15)}$$

where m_I represents the magnetic quantum number of spin I. For each value of m_I there will be a corresponding energy level, each differing by $\gamma\hbar B_o$ as depicted in Figure 2-7.

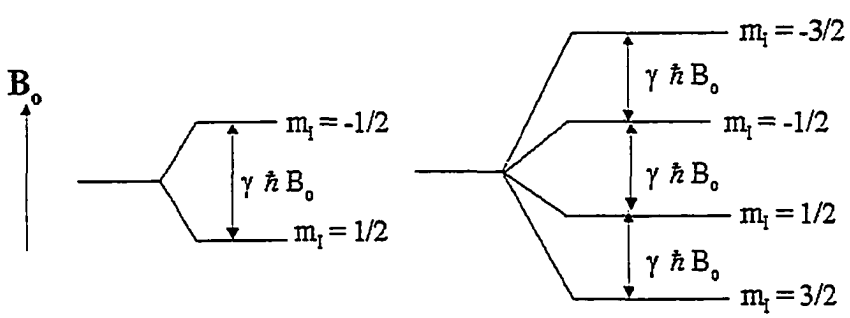

Figure 2-7. Zeeman energy levels splitting for spin ½ and 3/2 nuclei.

Transitions between adjacent energy levels may be induced by the application of a sinusoidal radio-frequency (rf) pulse, represented by $\mathbf{B_1}$ ($|\mathbf{B_1}| << |\mathbf{B}|$) of frequency ω and applied perpendicular to B. The Hamiltonian of the interaction then becomes:

$$H = -\gamma\hbar\,\mathbf{I}\cdot\mathbf{B} - \gamma\hbar\,\mathbf{I}\cdot\mathbf{B_1} \qquad \text{Eq. (16)}$$

For $\mathbf{B}$ along the z-axis and $\mathbf{B_1}$ along x-axis the Hamiltonian becomes:

$$\begin{aligned} H &= -\hbar\, I_z\omega_o - \gamma\hbar\, I_x\,(2|\mathbf{B_1}|\,\mathrm{Cos}\,\omega t) \\ &= -\hbar\, I_z\omega_o - 2\hbar\,\omega_1 I_x\,\mathrm{Cos}\,\omega t \end{aligned} \qquad \text{Eq. (17)}$$

where $\omega_o = \gamma|\mathbf{B}|$ and $\omega_1 = \gamma|\mathbf{B_1}|$.

Since $|\mathbf{B_1}| << |\mathbf{B}|$ the effect of $\mathbf{B_1}$ may be treated as a time dependent perturbation, giving the transition rate as:

$$P_{mm'} = \gamma^2 |\mathbf{B_1}|^2 |\langle m|\mathbf{I_x}|m'\rangle|^2\,\delta(\nu_{mm'} - \nu) \qquad \text{Eq. (18)}$$

where

$$\nu_{mm'} = \frac{\Delta E_{mm'}}{h} = \frac{\gamma|B_o|\|m'-m|}{2\pi} \qquad \text{Eq. (19)}$$

From Eq. (18) the following can be concluded:

1. $\mathbf{B_1}$ must be perpendicular to $\mathbf{B}$ in order to induce transitions between the adjacent energy levels.
2. the conditions $m - m' = \pm 1$ and $2\pi\nu_{mm'} = \gamma |\mathbf{B}|$ must be satisfied in order for transitions to be induced.
3. the transition rate is proportional to γ^2 and the amplitude of the rf field $\mathbf{B_1}$.

The condition $2\pi\nu_{mm'} = \gamma |\mathbf{B}|$ is the resonance condition with the Larmor frequency given by $\omega_o = 2\pi\nu_{mm'} = \gamma |\mathbf{B}|$.

2.2. NMR Interactions in solids

The interaction of the nuclei with their environment may be represented by:

$$H = H_Z + H_Q + H_D + H_{CS} + H_J + Other \qquad \text{Eq. (20)}$$

Where H_Z, H_Q, H_D, H_{CS}, and H_J represents the Zeeman, quadrupolar, dipole-dipole, chemical shift, and scalar or indirect coupling Hamiltonians respectively. The Zeeman interaction refers to the coupling of the spins with the static magnetic field. At a field of 7.1 and 11.7 Tesla, the proton resonance frequency is 300 and 500 MHz respectively. This interaction is the most dominant and because of this the other interactions may be treated as perturbations.

2.2.1. Dipolar interactions

The interaction of neighboring nuclear spins results in dipolar interactions. For two spins the Hamiltonian is given by:

$$H_D = \frac{\mu_1 \bullet \mu_2}{r^3} - \frac{3(\mu_1 \bullet r)(\mu_2 \bullet r)}{r^5} \qquad \text{Eq. (21)}$$

where $\boldsymbol{\mu}_1 = \gamma\hbar\mathbf{I}_1$ and $\boldsymbol{\mu}_2 = \gamma\hbar\mathbf{I}_2$ and r is the internuclear vector as shown in Figure 2-8.

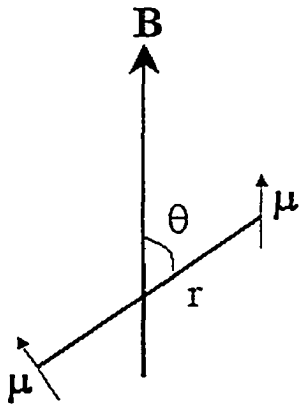

Figure 2-8. Dipolar interaction between two spins in static B field.

The dipole-dipolar (DD) Hamiltonian consists of interactions between both like and unlike nuclei. For protons, which have 99.8% abundance, the like term is often the largest (in the absence of unpaired electrons). For example, the homonuclear proton-proton interaction for a separation distance of 2 Å may be estimated by $\omega_D = \gamma_1\gamma_2\hbar/r^3$ and has magnitude 94 kHz. For a ^{13}C- proton dipolar interaction with a separation distance of 1 Å however, we have magnitude of 176 kHz. The carbon-proton interaction in a C-H bond is therefore comparable to that of the proton-proton, except for molecular H_2. This is because of the $1/r^3$ dependence of the interaction.

The dipolar Hamiltonian may be written as:

$$H_D = \mathbf{I}_1 \cdot \mathbf{D} \cdot \mathbf{I}_2 = \omega_D [A + B + C + D + E + F] \qquad \text{Eq. (22)}$$

where the terms A through F have the following form:

$$A = I_{1z}I_{2z}(1 - 3\cos^2\theta)$$

$$B = -\tfrac{1}{4}(1 - 3\cos^2\theta)[I^+_1I_2 + I_1I^+_2]$$

$$C = -3/2 \sin\theta\cos\theta\, e^{-i\phi}\,[I_{1z}I^+_2 + I^+_1I_{2z}]$$

$$D = -3/2 \sin\theta\cos\theta\, e^{-i\phi}\,[I_{1z}I_2 + I_1I_{2z}]$$

$$E = -\tfrac{3}{4} \sin^2\theta\, e^{-i2\phi}\,[I^+_1 I^+_2]$$

$$F = -\tfrac{3}{4} \sin^2\theta\, e^{i2\phi}\,[I_1 I_2]$$

Only terms A and B are used to calculate the effect of the dipolar interaction on the Zeeman eigenstates. These effects vanish under Magic Angle Spinning (MAS) because of their dependence on the factor $(1 - 3\cos^2\theta)$. For unlike spins only term A needs to be considered. The terms C through F are off diagonal, their effect is to introduce admixtures of the zero-order states into the exact states.

2.2.2 Quadrupolar interactions

All nuclei with spin $I > \frac{1}{2}$ have electrical quadrupole moments, which interacts with the electric field gradient produced by the asymmetric electron cloud density at the site of the nucleus, and the charge distribution external to the nucleus. Classically the interaction energy E of a charge distribution of density ρ with a potential V is given by:

$$E = \int \rho(\mathbf{r})\, V(\mathbf{r})\, d\tau \qquad \text{Eq. (23)}$$

Expanding the electrostatic potential in a series gives:

$$V(x,y,z) = V_o + \sum_i \left(\frac{\partial V}{\partial x_i}\right)_{=0} x_i + \frac{1}{2}\sum_{i,j}\left(\frac{\partial^2 V}{\partial x_i x_j}\right)_{=0} x_i x_j + \ldots \qquad \text{Eq. (24)}$$

Inserting this potential into Eq. (23) yields the multipoles, of which the first two parts are the potential of the overall charge distribution and the electric dipole moment of the charge distribution. The third part corresponds to the electron quadrupole moment, defined as V_{ij}. V_{ij} corresponds to the component of the electric field gradient (EFG) tensor at the site of the nucleus. The electric quadrupole moment tensor defined as $\underline{Q}_{ij}$, is given by:

$$\underline{Q}_{ij} = \int (3x_i x_j - \delta_{ij} r^2)\, \rho(\mathbf{r})\, dV \qquad \text{Eq. (25)}$$

The quadrupole energy is therefore given by:

$$E_Q = \frac{1}{6}\sum_{ij} V_{ij} Q_{ij} \qquad \text{Eq. (26)}$$

The quantum mechanical treatment of this may be expressed as:

$$H_Q = \mathbf{I}\cdot\mathfrak{Q}\cdot\mathbf{I}, \text{ where } \mathfrak{Q} \text{ is given by } \frac{eQ}{2I(2I-1)\hbar}V \qquad \text{Eq. (27)}$$

where V now corresponds to the electric field gradient. In expanded form Eq. (27) becomes:

$$H_Q = \frac{eQ}{6I(2I-1)\hbar}\sum_{ij} V_{ij}\left[\frac{3}{2}(I_i I_j + I_j I_i) - \delta_{ij} I(I+1)\right] \qquad \text{Eq. (28)}$$

where eQ is the quadrupole moment of the nucleus. In the principal axis system of EFG (x,y,z) V_{ij} becomes diagonal and H_Q reduces to:

$$H_Q = \frac{e^2qQ}{4I(2I-1)\hbar}[3I_z^2 - I^2 + \eta\,(I_x^2 - I_y^2)] \qquad \text{Eq. (29)}$$

where $eq = V_{zz}$, the largest component of EFG and η is called the asymmetry parameter, which ranges between [0,1] and is defined as:

$$\eta = \frac{V_{xx} - V_{yy}}{V_{zz}} \qquad \text{Eq. (30)}$$

For a magnetic field applied along the laboratory Z-axis, the angles θ and ϕ between the principal axis coordinate (x,y,z) and the laboratory frame (X,Y,Z), is shown in Figure 2-9.

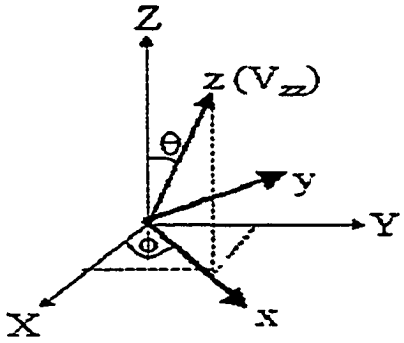

Figure 2-9. The orientation of the principal-axis frame of EFG (x,y,z) relative to the laboratory frame (X,Y,Z). The V_{zz} component of the EFG tensor aligned along the z-axis.

In an electric field with axial symmetry $\eta = 0$, H_Q becomes:

$$H_Q = \frac{e^2qQ}{4I(2I-1)\hbar}[3I_z^2\cos^2\theta + 3I_x^2\sin^2\theta + 3(I_zI_x+I_xI_z)\sin\theta\cos\theta - I(I+1)] \quad \text{Eq. (31)}$$

Treating H_Q as a perturbation on the Zeeman interaction, the first order perturbation on the energy levels in a symmetric field gradient is given by:

$$E_m = \frac{e^2qQ}{8I(2I-1)}(3\cos^2\theta - 1)[3m^2 - I(I+1)] \quad \text{Eq. (32)}$$

The energy-level schemes and theoretical single crystal absorption spectrum for spin 1 nucleus is shown in Figure 2-10.

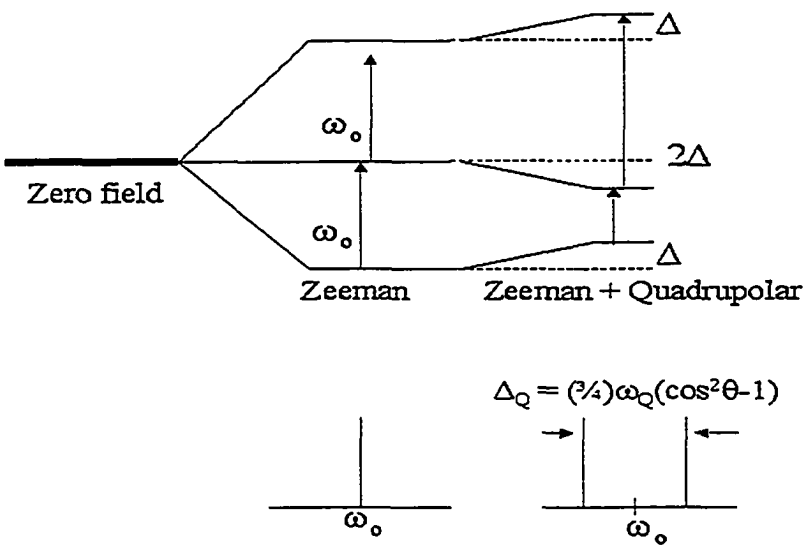

Figure 2-10. The energy levels and single crystal spectrum for spin I = 1 nucleus with quadrupole interaction.

In the case of an asymmetric field gradient $\eta \neq 0$, the first order energy shift becomes:

$$E_m = \frac{e^2qQ}{8I(2I-1)}(3\cos^2\theta - 1 + \eta\sin^2\theta\cos 2\phi)[3m^2 - I(I+1)] \qquad \text{Eq.(33)}$$

The first order frequency shift for the m $\rightarrow$ m-1 transition is:

$$\omega_{m\leftrightarrow m-1} = -\frac{\omega_Q}{4}[(3\cos^2\theta - 1) - \eta\sin^2\theta\cos 2\phi)](2m-1) \qquad \text{Eq. (34)}$$

where $\omega_Q = \frac{3e^2qQ}{2I(2I-1)\hbar}$ is the quadrupole frequency. When the EFG is small the first order interaction is observable. However as the interaction increases, splitting in the central transition may be observed. For the ½ $\leftrightarrow$ -½ transition this is given by:

$$\omega_{1/2\leftrightarrow -1/2} = \frac{\omega_Q^2}{16\omega_o}\{(9\cos^2\theta - 1)(1 - \cos^2\theta)[I(I+1) - 3/4]\} \qquad \text{Eq. (35)}$$

In first order perturbation the central transition has no frequency shift, and the central transition is therefore only dipolar broadened. In second order however, the central transition is broadened asymmetrically. When the interaction becomes strong enough, the satellites and the central transition may be broadened beyond the detection range.

For the work presented in this thesis, most is on the proton and fluorine nuclei, which are spin I = ½ and therefore lack quadrupole interactions. Lithium however is spin I = 3/2 and as such has a quadrupole moment. The lithium spectra contains 2I = 3 lines, corresponding to a central transition with accompanying satellites.

2.2.3 Chemical shift interactions

The interaction of the nuclei with the static magnetic field by way of the surrounding electron density constitutes the chemical shift. Due to the motion of the electrons at the site of the nucleus, which is caused by the electrons interactions with the static magnetic field, the field experienced by the nucleus will be the vector sum of static **B** field and the local induced field caused by the motion of the electrons. This modification of the effective field results in a shielding or de-shielding of the nucleus. Quantum mechanically this interaction may be represented as:

$$H_{CS} = \gamma \, \boldsymbol{I} \cdot \boldsymbol{\sigma} \boldsymbol{B}_o \qquad \text{Eq. (36)}$$

where $\boldsymbol{\sigma}$ is the "shielding tensor" which describes the orientation dependence of the interaction. The shielding tensor may be divided into three parts: an isotropic, symmetric and asymmetric part. In general the shielding tensor consists of nine terms, whereby upon transformation to the principal axis system (PAS) it becomes diagonal with terms: σ_1, σ_2, and σ_3. The components of the diagonal σ are defined such that $\sigma_1 \leq \sigma_2 \leq \sigma_3$. The first order shift in Zeeman frequency is:

$$\Delta\nu_{\text{chemical shift}} = -\,\nu_{\text{Zeeman}} \left[\sigma_{\text{isotropic}} + \sigma_{\text{anisotropic}} \left(3\cos^2\theta - 1\right) + \sigma_{\text{axial}} \sin^2\theta\cos 2\phi\right] \qquad \text{Eq. (37)}$$

where:

$$\sigma_{\text{isotropic}} = 1/3(\sigma_1 + \sigma_2 + \sigma_3)$$

$$\sigma_{\text{anisotropic}} = 1/6(2\sigma_3 - \sigma_1 + \sigma_2)$$

$$\sigma_{axial} = 1/2(\sigma_2 - \sigma_1)$$

In the event of molecular motion averaging, this reduces to:

$$\Delta\nu_{chemical\ shift} = -\nu_{Zeeman}\sigma_{isotropic}$$

where the dependence upon the nuclei's orientation with respect to the static B field is removed.

2.2.4 Scalar or Indirect coupling

The interaction between neighboring nuclei by way of the bonding electrons is termed indirect or scalar coupling. There are two terms that can result from such interaction: the coupling of the nuclear spins with the static **B** field by way of the electron orbital angular momentum; the other is by way of the electron spin and is termed the Fermi Contact interaction, and is specific to metals. Both interactions are represented in Eqs. 38 and 39.

$$H_J = g\beta\sum_N\sum_k\gamma_N\{\frac{3(S_k\bullet(r_k-r_N))(I_N\bullet(r_k-r_N))}{|r_k-r_N|^5}-\frac{S_k\bullet I_N}{|r_k-r_N|^3}\} \qquad \text{Eq. (38)}$$

$$H = \frac{16\pi}{3}\beta\sum_N\sum_k\gamma_N S_k\bullet I_N\delta(r_k-r_N) \qquad \text{Eq. (39)}$$

J couplings give direct information about chemical bonds and are completely intramolecular. They are orientation dependent but field independent. J couplings are usually overshadowed by other interactions such as dipole-dipole couplings in solids, however their contribution increases in the liquid state.

2.2.5 Relaxation Mechanisms

Determining the relaxation mechanism is one of the most important goals in NMR as it can yield information not only about the motional processes in the molecules but also about their interactions. In determining relaxation mechanisms it becomes necessary to introduce the correlation time and correlation function. Random molecular motion results in fluctuations of both the magnitude and orientation of the externally applied rf field and the local field at the site of each nucleus. These fluctuations result in relaxation of the spin system as the system experiences motion. The fluctuating field is related to the correlation function $G(\tau)$ that is given by:

$$G(\tau) = G(0)e^{-\tau/\tau_c} \qquad \text{Eq. (40)}$$

where $G(0)$ represents the mean square of the fluctuating field, and τ_c is the correlation time. The purpose of this function is to give the position of a molecule at time τ relative to its position at an earlier time, $G(0)$. The correlation time is defined as the time in which a molecule remains in any given position before a collision causes it to change position or orientation. Rapid fluctuations results in small τ_c, while slow fluctuations have large τ_c. The correlation time is dependent on the physical parameters of the system, such as temperature. To obtain information in the frequency range one needs to use the Fourier transform of the correlation function. This is known as the spectral density, $J(\omega)$ and is given by:

$$J(\omega)=\int_{-\infty}^{\infty} G(\tau)\, e^{-i\omega\tau}\, d\tau = A[\tau/(1+\omega^2\tau^2)] \qquad \text{Eq. (41)}$$

where A is a constant related to the mean square of the fluctuating field. For a rapidly fluctuating field τ_c is short and therefore is $J(\omega)$ broad. For slow fluctuations τ_c is large, resulting in narrow $J(\omega)$. This relationship is depicted in Figure 2-11.

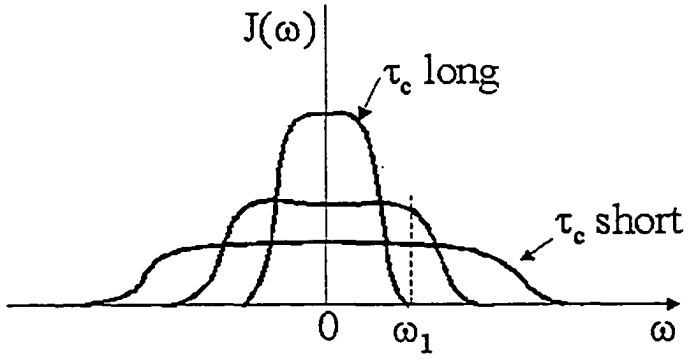

Figure 2-11. Illustration of the relationship between $J(\omega)$ and τ_c.

2.3. NMR interactions in liquids

In isotropic liquids the main terms of Eq. (22) that contribute to the resulting NMR spectrum are H_{CS}, and H_J,. The reduced dipolar contribution containing the factor $(1 - 3\cos^2\theta)$ averages to zero due to the rapid motion of the molecules. This results in zero contribution from the intramolecular dipole-dipole (DD) couplings. In addition to this, due to the translational motion of the molecules the short-range intermolecular DD couplings also averages to zero. The long-range DD couplings do not average to zero. Their intensities are however very small, and may therefore be ignored. For non-isotropic

liquids such liquid crystals, there are preferred orientations dependences, thus the intramolecular DD couplings do not average to zero.

The quadrupolar interaction in an isotropic liquid averages to zero due to the rapid motion of the molecules. This interaction does not influence the position of the NMR peaks. They do however influence the relaxation of the nuclear spins > ½ in isotropic liquids. In anisotropic liquids the quadrupolar interactions do not average to zero, again this is due to the preferential alignment of the spins.

The chemical shift interaction in isotropic liquids averages to give only the $\sigma_{isotropic}$ term. For anisotropic liquids this is not the case, thus the motionally chemical shift is not the same as the isotropic chemical shift. Thus monitoring the chemical shift can give information on possible phase changes.

J-couplings in liquids are averaged due to molecular motions. In isotropic liquids the J-coupling tensor averages to the trace of the diagonal terms, and becomes independent of orientation.

2.4. AC impedance spectroscopy

The ionic conductivity σ, is a measure of charge transport under the influence of an externally applied electric field. It is usually measured by the method of AC impedance spectroscopy (IS). The method involves measuring the impedance Z directly in the frequency domain by the application of a frequency dependent voltage to the electrodes and observing the response of the system being investigated. This response is in the form of a current and is also frequency dependent. Typically the electrolyte is capacitively coupled to the electrodes. The test cell may also contain capacitive and

inductive components in addition to the resistive components. In general, the total complex impedance Z has the form:

$$Z = R - j/\omega C + j\omega L \qquad \text{Eq.(42)}$$

where C is the capacitance, R is the resistance, L is the inductance and j is $\sqrt{-1}$. The data is represented in the complex plane with the real component arising from the resistances and the imaginary component from the capacitances and inductances. The system's resistance is obtained from the impedance arc's intersection with the real-axis. The ionic conductivity is then calculated through the relationship:

$$\sigma = \text{geometrical factor}/R \qquad \text{Eq. (43)}$$

where R is the resistance, and the geometrical factor is related to the cell dimension. The conductivity is measured in units of Siemens per centimeters (S/cm), and the resistance is in Ohms (Ω).

In measuring the ionic conductivity a test cell in conjunction with lead wires, electrodes and interfaces is used. This results in a coupling of the electrolyte's conductivity with that of the external peripherals. An equivalent circuit for this complex impedance system is shown in Figure 2-12. Here R_∞ and C_∞ represent the bulk resistance of the system and the cell geometrical capacitance respectively, whereas R_2 and C_2 represents the interfacial resistance and diffuse double layer response capacitance of the polarization region near the electrode [41]. The measured total impedance will therefore

include contributions from system charge transfer, mass transport, effect of interface between electrodes and the system. The mass transport components are superior at low frequency whereas the charge transfer resistance takes over at high frequency.

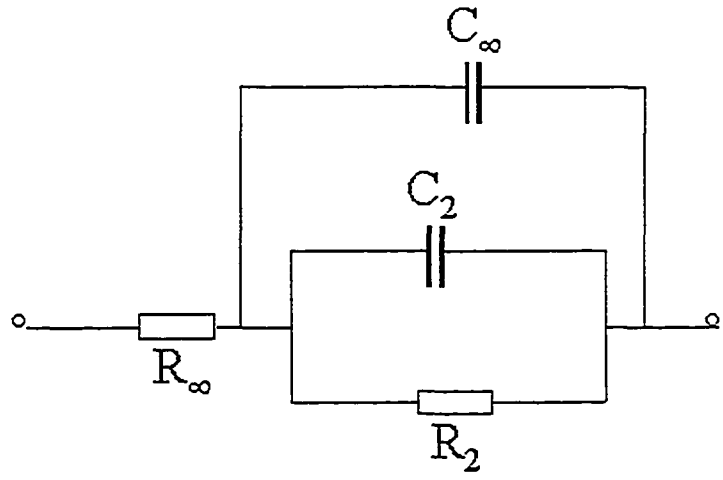

Figure 2-12. Equivalent circuit of an electrochemical cell with aqueous acid solutions.

The response of the leads of the measuring cell will be eliminated by calibration of the system by using an aqueous solution of known ionic conductivity at the desired temperature.

The ionic conductivity (σ), the viscosity (η) and the self –diffusion coefficient (D) are related through the Nernst-Einstein and Stokes-Einstein equations, as given below respectively:

$$\sigma = \frac{Dq^2c}{kT} \qquad D = \frac{kT}{4r\pi\eta} \qquad \text{Eq. (44)}$$

Here D represents the sum of the anion and cation diffusion coefficients, q is the charge of the carrier, k is the Boltzmann constant, c is the concentration, T is the absolute temperature, and r is the hydrodynamic radius of the spherical. Both equations were developed for application to very dilute solutions. In these systems the ions are depicted as hard non-interacting spheres, moving through a continuum of viscosity η under the influence of an applied electric field. Because of this, large errors are often obtained from the application of either equation to concentrated systems, with the calculated values being higher than the experimental ones.

The main sources of errors are due to: concentration, relaxation or drag, and electrophoretic effects. As the concentration increases there is a greater probability for ion association due to inter-ionic effects caused by electrostatic interactions. The result of this may be the formation of ion pairs and larger aggregates, therefore reducing their involvement in the transport process. The relaxation effect arises from the dissolution of symmetry of the ionic atmosphere about the central ion in an electric field. Since positive and negative charges move in opposite directions in an electric field, the ionic atmosphere will be pulled away from the central ion, thus creating an asymmetric environment. This in turn 'drags' the central ion and reduces its mobility. The electrophoretic effect refers to the movement of solvent molecules with the ions in the electric field. Again, because anions and cations move in opposite directions under an externally applied electric field, this result in every ion being subjected to the friction that result from moving against such a flow. This reduces the ionic conductivity.

Chapter 3. Experimental

3.1. NMR Hardware

NMR information was obtained at both 300 and 500 MHz. At 300 MHz the system used was a *Chemagnetics* CMX spectrometer with a 7.1 Tesla Japan Magnet Technology superconducting magnet. The Larmor frequencies of ^{1}H, ^{7}Li and ^{19}F at this field are 301.02, 116.98 and 283.2 MHz, respectively. The probe used was a 5mm triple resonance Nalorac Z-Spec gradient probe with two observation/excitation coils. The outer one was for protons and fluorine while the inner one was for the X-channel. The power capability for the proton and X-channel is 30 and 150 Watts respectively. Magnetic gradients are applied along the z-axis, with gradient strengths ranging from 0.2 - 1.2 T/m. At 500 MHz the system used was a Varian Unity spectrometer in conjunction with an 11.7 Tesla narrow bore magnet. The probe was a 5mm reversed detect triple resonance z-axis gradient probe. The proton coil was located on the inside, while the outer coil is for the X-channel. Both spectrometers had built-in Fourier transform capabilities.

The parameters investigated were chemical shifts, line-widths, spin-lattice relaxation times and self-diffusion coefficients. Spectral information was obtained by Fourier transforming the resulting free induction decay (FID) obtained by a single $\pi/2$ pulse. In addition to this, the Fourier transform of the maximum echo signal obtained from the quadrupolar echo $[(\pi/2)_x - \tau - (\pi/2)_y]$ pulse sequence was also used. Self-diffusion coefficients (D) were determined by the NMR Pulse Gradient Spin Echo technique and spin lattice relaxation times (T_1) were determined by Inversion Recovery.

3.2. NMR Techniques

3.2.1. NMR Pulse Gradient Spin Echo (PGSE)

Using NMR as a tool for measuring the self-diffusion coefficients (D) of diffusing species was first developed by Hahn (1950) [42]. Originally the technique involved the use of a typical spin echo pulse sequence, which consisted of two *rf* pulses: one 90° and the other a 180°, separated by time τ. In addition to this a constant magnetic gradient was applied along the z-axis. The method was later modified by Stejskal and Tanner (1965) in which they replaced the constant magnetic gradient by pulsed magnetic gradients [43]. The application of pulsed gradients as opposed to one that is constant eliminates the need for wider-bandwidth receivers and reduces the duty cycle associated with the long gradient pulse. The modified version is referred to as the Nuclear Magnetic Resonance Pulse Gradient Spin-Echo (NMR PGSE) technique and is shown in Figure 3-1 in time sequential form.

The NMR PGSE technique consists of two *rf* pulses: first a 90°, then a 180°. Following each *rf* pulse are magnetic gradients of strength g and duration δ, separated by time Δ. The core of the NMR PGSE technique lays in the fact that in the presence of a magnetic field with superimposed magnetic gradients a diffusing nucleus will experience changes in the magnetic field it experiences and its resulting phase. This change in phase results in attenuation of the magnetization **M** and the resulting attenuation factor is given by [44]:

$$M(t)/M(0) = \exp\left(-\gamma^2 g^2 D \delta^2(\Delta-(\delta/3)\right) \qquad \text{Eq. (1)}$$

where D is the self-diffusion coefficient of the diffusing species and t is the time of the pulse sequence.

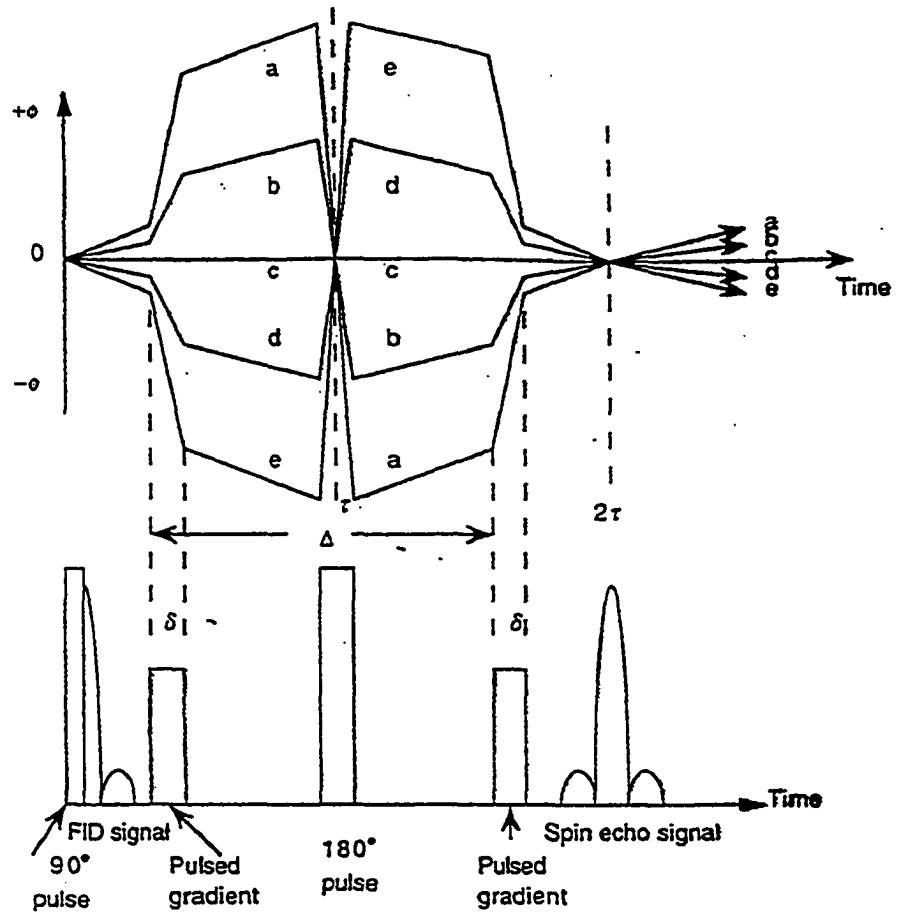

Figure 3-1. PGSE pulse sequence showing the experimental times, δ, Δ and τ.

The attenuation of the spin echo vs. gradient strength is shown for a representative system in Figure 3-2. In order to obtain D, g, Δ, τ and γ must be known. Typical values of δ are a few milliseconds, while Δ ranges from a few milliseconds to a few hundred milliseconds. Typical π/2 pulse width of 15 μs for ^{1}H, 6μs for ^{7}Li and 11 μs for ^{19}F were used. Uncertainties in self-diffusion measurements are ~3-10%.

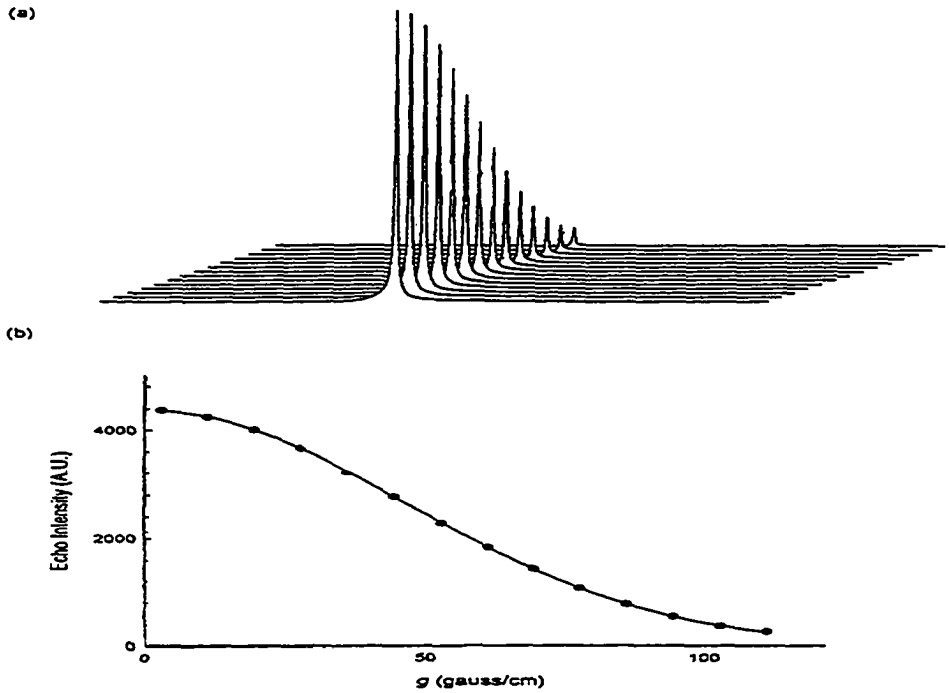

Figure 3-2. A representative ^1H PGSE NMR decay profile and plot from which the diffusion coefficient is obtained.

3.2.2. Spin-Lattice relaxation times - T_1

To determine the longitudinal relaxation time T_1, the inversion recovery technique is used. The pulse sequence for this technique is π - τ - $\pi/2$. The time interval τ is varied using about 12 – 15 values. Immediately following the π pulse the **M** is inverted. During the time interval, **M** relaxes back to thermal equilibrium at a rate of T_1^{-1}. The application of the $\pi/2$ cause **M** to rotate from the z-axis into the x-y plane where the signal may be picked up by a receiver. From the Bloch equations the time dependence of M_z is as follows:

$$\frac{dM_z}{dt} = -\frac{M_z - M_o}{T_1} \qquad \text{Eq. (2)}$$

Integration of this leads to:

$$M_z = M_o(1-2\exp^{-\tau/T_1}) \qquad \text{Eq. (3)}$$

The time interval between each τ increment must be at least 5 of the longest T_1 to be measured as it takes this length of time for the system to be fully recovered from the application of the π pulse. Failure to do so can result in significant errors in T_1 measurement. T_1 was obtained by fitting the exponential recovery to $[A_\infty - A(\tau)]/A_\infty = C \exp(-\tau/T_1)$ where A_∞ and C are fitting constants.

3.3 Conductivity Hardware

The ionic conductivity of all aqueous solutions was determined by measuring the ionic resistivity using a Schlumberger SI 1260 IMPEDANCE / GAIN-PHASE ANALYZER with frequency in the range: 1Hz to 10 MHz, with stainless steel blocking electrodes. The conductivity cells used were made of polypropylene and Teflon. Both real and imaginary components of the impedance were measured. Temperature was maintained at 30°C by an external temperature bath in which the cells containing the aqueous acid solutions were allowed to equilibrate for 30 minutes. Solutions with known ionic conductivities such as potassium chloride at varying concentrations were used to gain confidence in the procedure. Errors in respective measurements were less than 5%.

3.4. Viscosity measurements

The viscosity η was obtained by the Falling sphere method. Gilmont brand viscometers were purchased from Cole Palmer, and consisted of a glass tube with a Teflon cover. There were three viscometer flask sizes and three choices of falling balls, each combination able to cover a specific viscosity range, as indicated in Table 3.1. Each viscometer was calibrated by the manufacturer, the calibration constant taking into account surface tension and other effects, that can hinder the passage of the falling ball and thus affect the results. Reference solutions used to check the accuracy of the constants included methanol, ethylene glycol, and acetic acid.

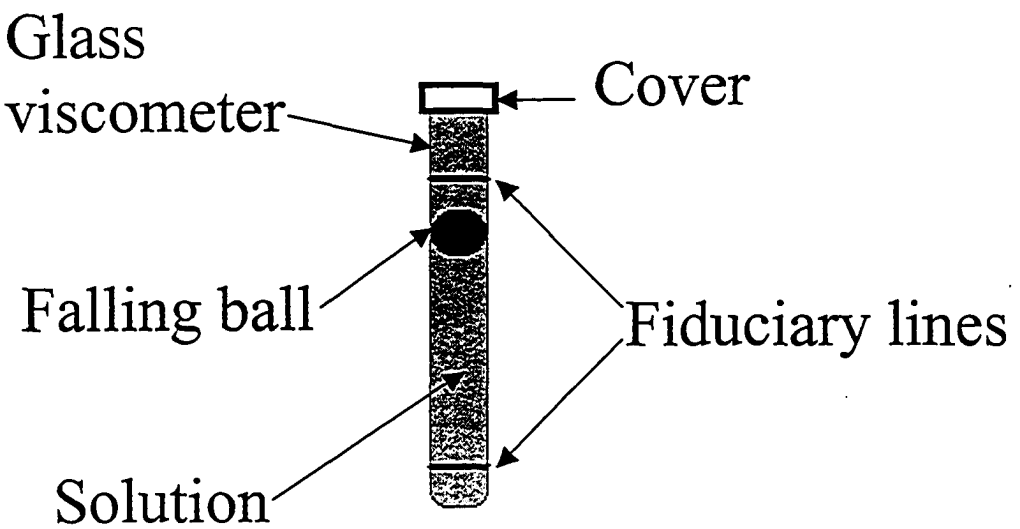

Figure 3-3. Viscometer setup.

Viscometer size	Viscometer range (cP)		
	Glass	Steel	Tantalum
1	0.2 – 2	1 - 10	2 - 20
2	2 – 20	10 - 20	20 - 200
3	20 – 200	100 - 1000	200 - 2000

Table 3.1. Viscosity size and viscosity range.

The viscosities were calculated from the following formula:

$$\eta = \kappa(\rho_b - \rho_f)t \qquad \text{Eq. (4)}$$

where:

κ = the viscometer constant

ρ_b = the density of the falling ball

ρ_f = the density of the solution

t = time of descent in minutes

The viscometer flask was held vertically upright by the use of a clamp stand during measurements. The viscometers containing the samples were placed in constant temperature water baths, with time intervals of 25-30 minutes allowed for equilibration. Three sets of measurements were taken and the data presented here is the average of all such measurements. Errors in respective measurements were between 2 – 15%.

3.5 Density measurements

In order to calculate the viscosity, the solution's density is needed. This was determined by using the simple mass and volume relationship. 10 ml volumetric flasks were filled with the solution and weighed. Before this method was used for the

superacids, measurements of the density of known systems, such as water, methanol and phosphoric acid provided confidence in the technique. Deviation of the calculated densities with the accepted values for each system was less than 1%.

The solution density was found to increase as the concentration increased. The highest densities of the PTSA and TFSA systems correspond to the pure acids, and those values were taken from the literature. However, there is no published density value for TFSI. The TFSI system has no published density therefore no such comparison is possible.

3.6 Sample preparation

3.6.1 Aqueous superacid solutions.

The superacids TFSA (99%), TFSI (95%), and PTSA (99%) were obtained from Sigma Aldrich. Both the PTSA and TFSI are solids at room temperature while the TFSA is in liquid form. Solutions of PTSA and TFSI were prepared by dissolving the necessary mass of the acids into 10ml of distilled water to obtain the required mole ratio of water to acid sites. The TFSA solutions were prepared by combining the required mass of the acid to make 10ml solutions, which were prepared in 10ml volumetric flasks. The molar ratio of water to acid molecules was used as the concentration scale because of the limits in solubility encountered in making concentrations higher than 4M for both TFSI and PTSA. As TFSA is a liquid at room temperature, no such difficulty was encountered and the molar concentration was used in sample preparation. However, for comparison reasons the molar ratio scale was chosen and calculated accordingly for each aqueous solution. Due to the very hygroscopic and viscous nature of the acids, solutions were

stored in glass flasks with glass stoppers in a dry box at less 1ppm moisture content, under a constant flowing nitrogen atmosphere.

For NMR measurements the solutions were packed into 5 mm OD and 20 mm length glass NMR tubes sealed with plastic covers and parafilm. In between measurements the samples were stored in the dry box. For ionic conductivity measurements the solutions were packed into Teflon (US Naval Academy) and polypropylene (Los Alamos National Laboratory) conductivity cells, in a dry box under nitrogen atmosphere. The cells were then removed from the dry box, and allowed to equilibrate at 30°C. For viscosity measurements approximately 8ml of solution was placed into the viscometer flask, sealed and allowed to equilibrate at 30°C in a water bath. For all measurements intervals of 20-25 minutes were allowed for temperature equilibration.

For all ^{1}H measurements done at 300 MHz the reference solution used was distilled water, while that for both ^{7}Li and ^{19}F was a saturated solution of $LiCF_3SO_3$.

3.6.2 DMSO Lock

For measurements at 500 MHz an external lock was used as the reference. The reference chosen was 99.9% DMSO (dimethyl sulfoxide), obtained from Sigma Aldrich. The DMSO was placed into a 5 mm OD NMR tube, which consisted of a rubber cover with a 4 mm ID hole its surface. The samples to be measured were placed into 4 mm OD capillary end NMR sample tube and secured into place in the DMSO containing tube, as depicted in Figure 3-4.

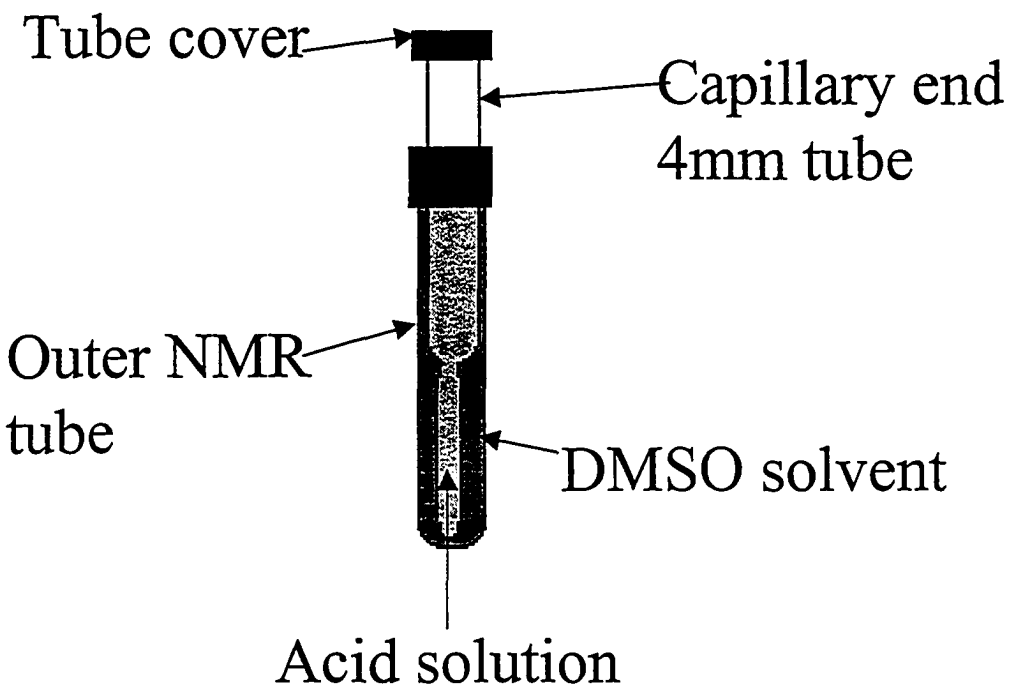

Figure 3-4. Sample setup used in ^{1}H NMR measurements at 500 MHz.

3.6.3 NP-PCM's

Three aqueous solutions consisting of 2 M fuel in 3 M sulfuric acid were prepared. All reagents were all obtained from Sigma-Aldrich. Five nano-porous proton conduction membranes (NP-PCM's) were investigated; their compositions (based upon volume %) are given in Table 2. All NP-PCM's consist of 60% free volume; membrane differences are based upon the ceramic type and ceramic concentration. The membranes were made by our collaborators at Tel Aviv University and further details can be found in ref [10-12]. The dry membranes were each cut into small strips, weighed, immersed and allowed to equilibrate in the three aqueous fuel/acid solutions for 48 hours. Excess liquid

was removed from the membranes, after which they were weighed and placed into sealed 5 mm (OD) NMR sample tubes for measurement.

Table 3.2. NP-PCM's composition by volume and room temperature ionic conductivity.

NP-PCM	Ceramic	Ceramic Powder %	PVDF %	Porosity %(as casted)	Conductivity RT (S/cm)
A	Aerosil 130	16	24	60	0.136
B	Aerosil 130	12	28	60	0.050
C	Aerosil 200	16	24	60	0.200
D	Aerosil 200	12	28	60	0.059
E	TiO_2	16	24	60	0.045

3.7. Error Analysis

All D, T_1, σ and η measurements reported are the average of several trials (at least three) done on various sets of samples over the course of more than a year. The errors in the measurements are based on the difference with respect the average value and falls between 1 and 15%, depending on the parameter.

Chapter 4. Superacids in water - Results and Discussion:

The results are analyzed in three parts: above 40 Molar Ratio (MR), MR between 20 and 40, and MR below 20, where MR refers to the ratio of water to acid molecules present in the solution. Thus low MR refers to high acid concentration and high MR refers to low acid concentration. The three concentration regimes will be referred to as regions 1-3 respectively.

4.1 Ionic Conductivity

Impedance spectra for the three superacids are shown in Figures 4-1 and 4-2. At low acid concentrations the spectra consisted of an inclined straight line that intersected the real axis at low resistance. This is typical of capacitive behavior of blocking electrodes (the electrolyte/electrode double layer capacitance) and is present for all the acids. As the concentration increased however, the intersection point moved to higher resistance, signifying the reduction in ionic conductivity. This effect was more evident for the TFSA system, as the semi circle component of the spectra, which is indicative of, increased ionic resistance, became observable as shown in Figure 4-2. The lack of the semi circle component for other solutions is due to its occurrence at higher frequencies outside the available range.

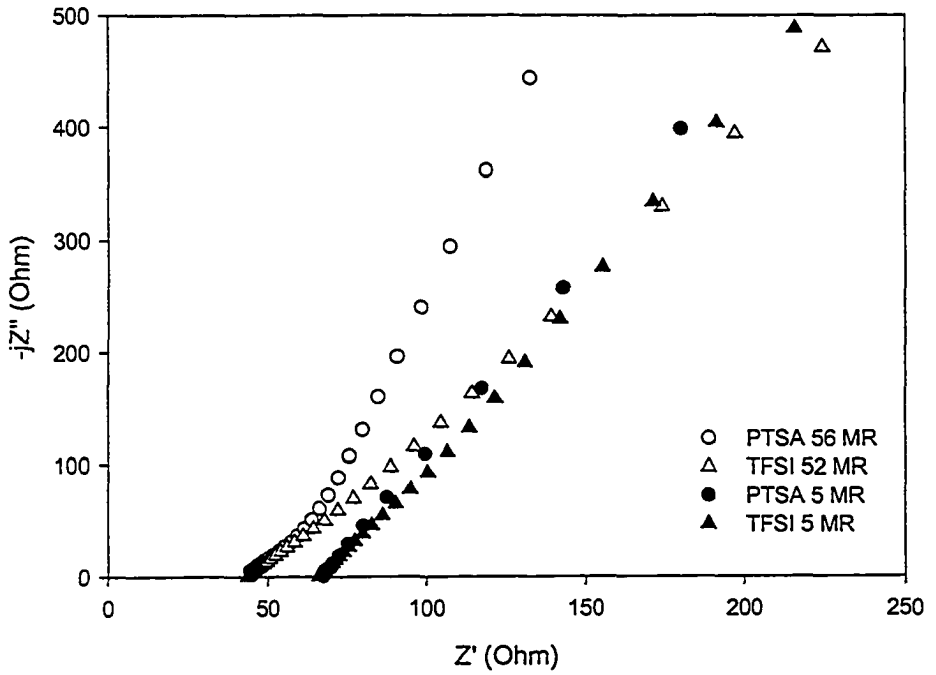

Figure 4-1. Impedance spectra of superacid solutions.

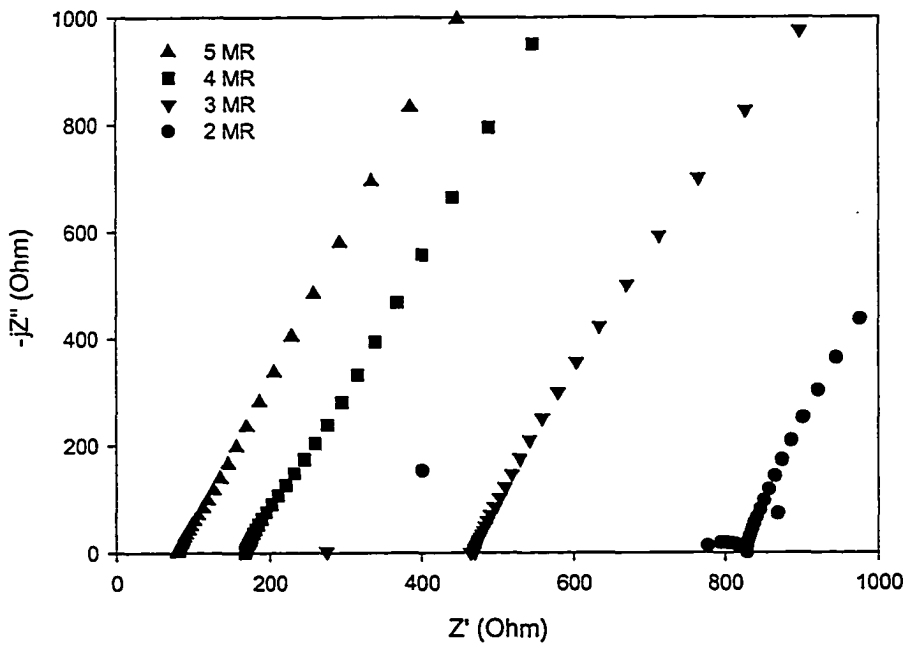

Figure 4-2. IS spectra for TFSA.

The ionic conductivity (σ) results for the three superacids are shown in Figure 4-3. All three acids displayed the same behavior, namely that of a conductivity maximum for a MR of 15-20. From the Nernst-Einstein and Stokes-Einstein equations shown respectively below (terms are described in Chapter 2), at a fixed temperature an increase in σ results from an increase in the number of charge carriers and/or an increase in the self-diffusion coefficient - D.

$$\sigma = \frac{Dq^2c}{kT} \qquad D = \frac{kT}{4r\pi\eta}$$

As D was observed to decrease with increasing concentration the increase observed in σ is attributed to an increase in the number of charge carriers. The reduction that follows the maximum is due to a number of factors. As the concentration increases, the solution η increases, and the solvent permittivity decreases. An increase in the solution viscosity results in a decrease in D, which in turn lowers σ. The reduction in the solvent permittivity causes reduced ion shielding, which augments ion-association into pairs and aggregates. These lead to relaxation and electrophoretic effects, both of which affect the ionic conductivity. The relaxation effect gain in significance as the concentration increases and the ionic atmosphere that surrounds the ion is no longer able to relax at a sufficient rate, thereby impeding the ionic conductivity. The electrophoretic effect also increases as the concentration increases and accounts for the increasing friction as the ions along with their solvating solvent molecules moves past each other under the influence of the externally applied electric field.

Of the three superacids the TFSA gave the highest ionic conductivity, as shown in Figure 4-3(a). Since the cationic species in any acid are the same at lower

concentrations, the difference in ionic conductivity in this region is attributed to the anions. Of the three superacids, the TFSA anion is the smallest, which accounts for TFSA having the highest ionic conductivity. In region 1 (MR > 40) both TFSI and PTSA gave similar σ. However, as the acid concentration increased, the PTSA σ's became higher, then once again merged with that of the TFSI system. This behavior of the TFSI acid may be attributed to it having the largest anion. In addition to this, the PTSA anion has the hydrophobic benzene ring, which reduces the friction (electrophoretic effect) as the solvated ions move past each other.

Of the three superacids, the TFSA system experienced the most dramatic decrease in ionic conductivity as the molar ratio was reduced. This was an indication that the TFSA system is more dependent on the level of hydration than the PTSA and TFSI systems, and that is more affected by increasing ionic association that results from increasing acid concentrations.

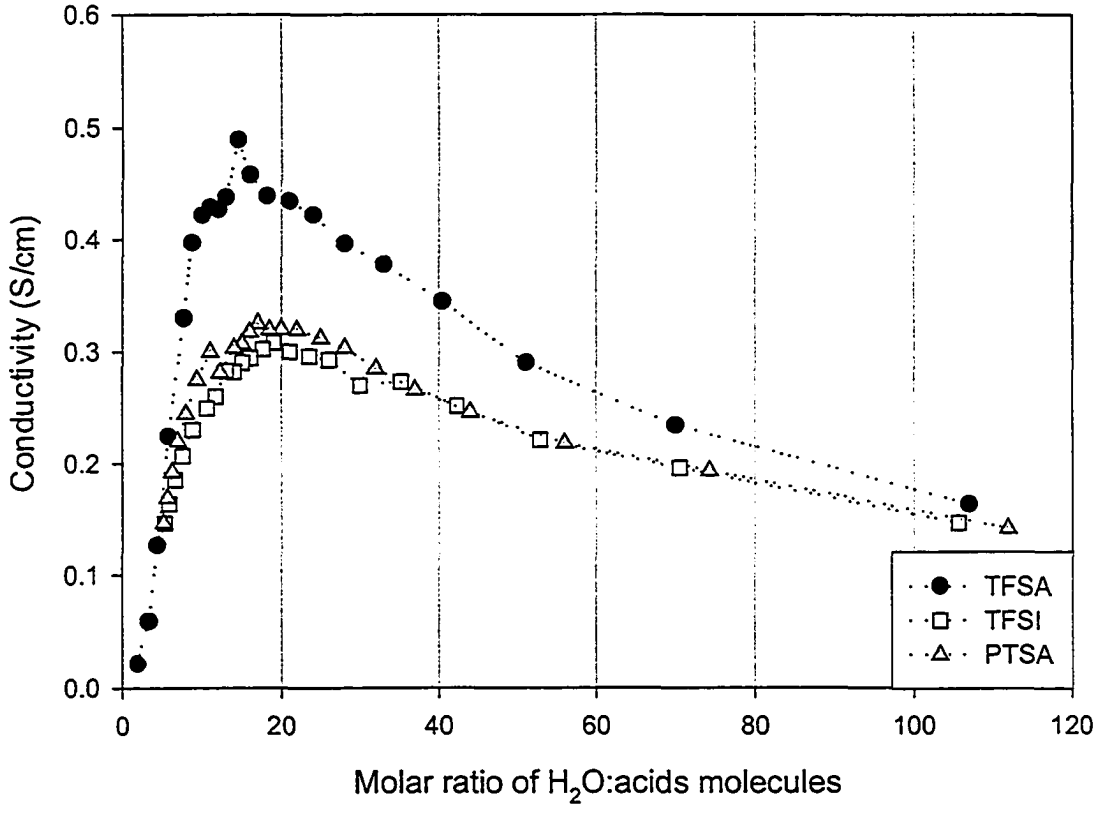

Figure 4-3 (a). Ionic conductivity of the three superacids.

At higher acid concentration the cationic species are no longer the same for all the acids, therefore the significant reduction that was observed for the TFSA system cannot be attributed solely to the anions. Instead, this behavior now includes the effect of reduced shielding from a low water concentration that augments ion interactions, which can result in ion-pairs and clusters formation. In addition to this the TFSA anion has greater charge density than that of both PTSA and TFSI. This makes the TFSA system more prone to electrostatic interactions (Coulomb and dipole-dipole), which can affect the transport parameters. This is supported by MD simulation results for TFSA [25, 45],

which showed that it takes at least six water molecules to properly shield the proton. Below this number there is a strong tendency for TFSA and PTSA to form contact-ion pairs. In addition to this the protons remain within 150 - 170 pm of the anions. Shown in Figure 4-3(b) is the expanded range of 0 - 10 MR. It can be stated that if the plots are extrapolated within this range to about 1 MR, one would expect that TFSI would give higher σ. While it was not possible to obtain experimental results for PTSA and TFSI below MR = 5 due to solubility limitation, MD simulation [46] results of TFSI molecule with up to six water molecules showed that TFSI needs only about 2 water molecules to dissociate. In addition, the dissociated proton is shielded with the addition of only 4 water molecules with separation distances of 250 - 260 pm. The results also showed that TFSI has a reduced tendency to form contact-ion pairs.

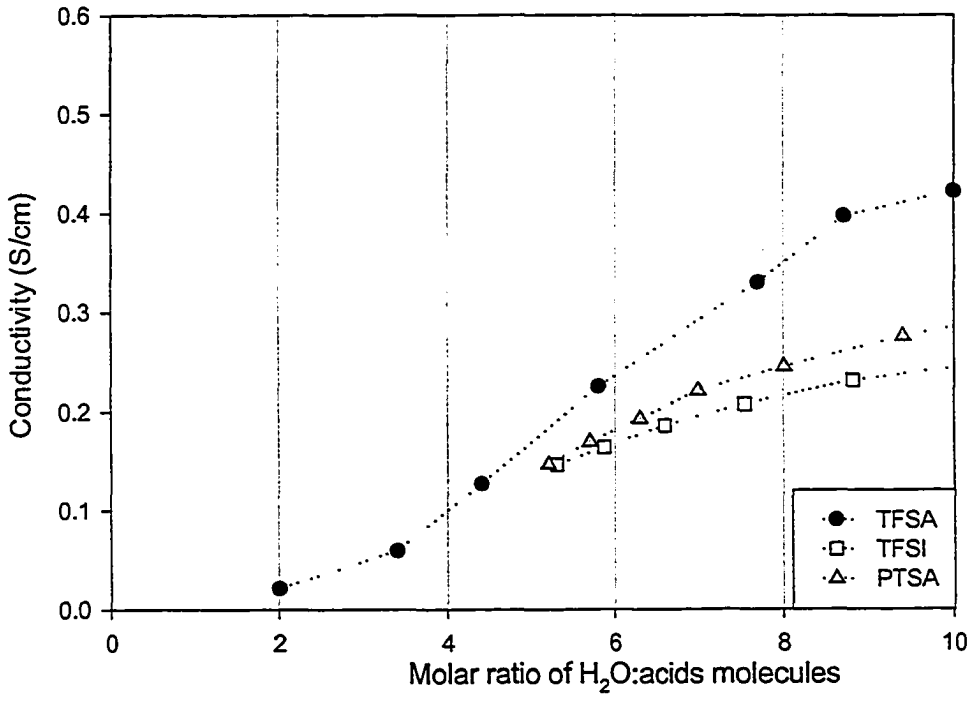

Figure 4-3(b). Expanded region of the ionic conductivity for TFSA, TFSI, and PTSA.

NMR Results

4.2 Spectra

The ^1H NMR spectra for both the TFSA and TFSI aqueous solutions consisted of a single peak, while that of the PTSA consisted not only of a main peak, but peaks assigned to the CH_3 and ring C_6H_4 protons, as shown in Figures 4-4(a) – (c). Present in all spectra are the reference d-DMSO's closely spaced (1ppm splitting) proton peaks. For the measurements the reference was set at 2.5 ppm corresponding to the 0.1% protons present in the DMSO solvent. The other DMSO peak that of the absorbed water and resulted due to the hygroscopic nature of DMSO. The intensity of this peak was dependent upon the amount of water absorbed, because of this it should not be used as a measure of comparison for the solution peak/s. This peak became useful in measurements of the chemical shift for the PTSA acid system, as the spectral window used was limited and the peak assigned to the 0.1% protons was not observed. In these measurements the chemical shifts were determined based on the fact that the DMSO's water and 0.1% proton signals in the 99.9% DMSO are known to occur within 0.85 ppm of each other.

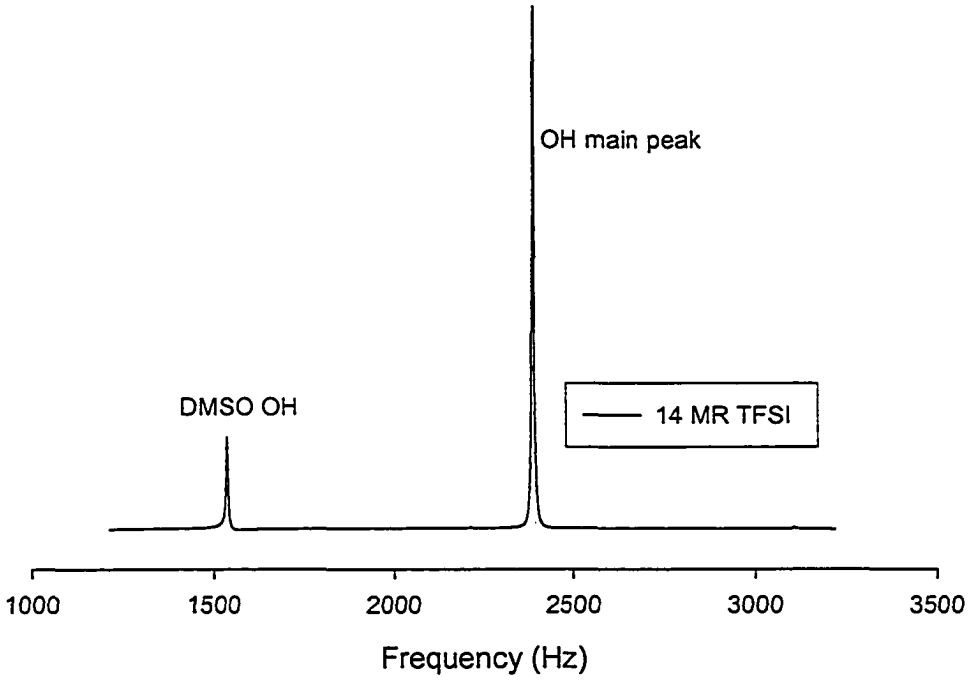

Figure 4-4(a). ^{1}H NMR spectrum of 14 MR TFSI with DMSO as the external reference.

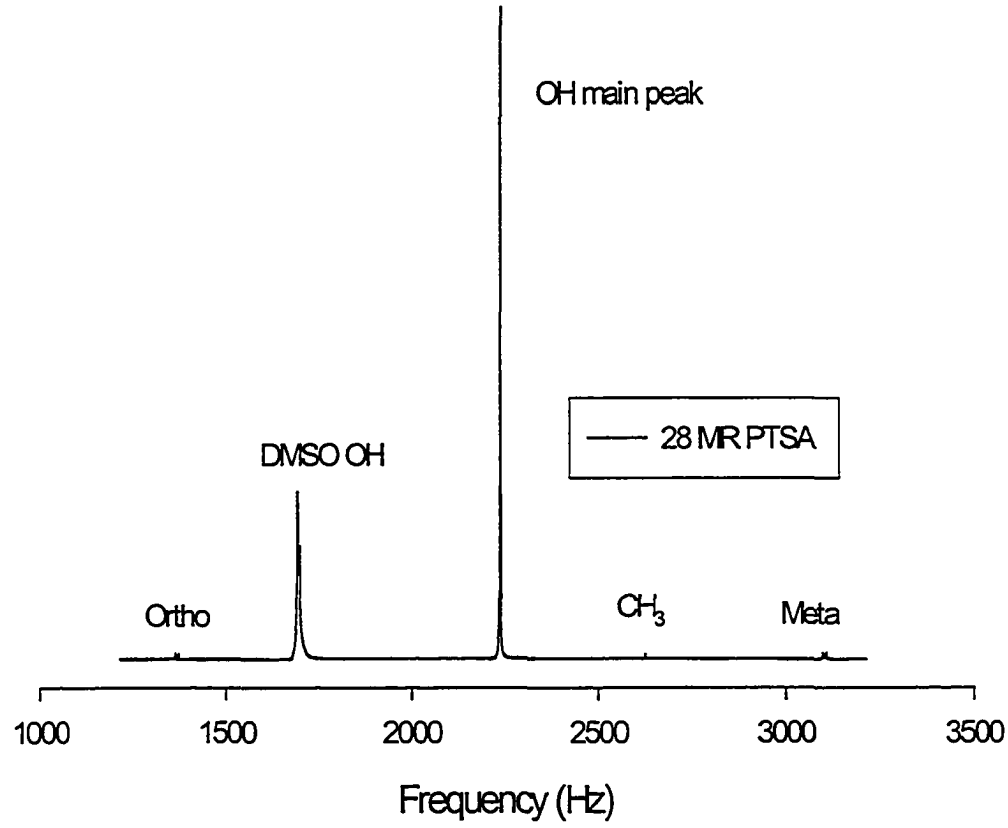

Figure 4-4(b). ^{1}H NMR spectrum of 28 MR PTSA with DMSO as the external lock.

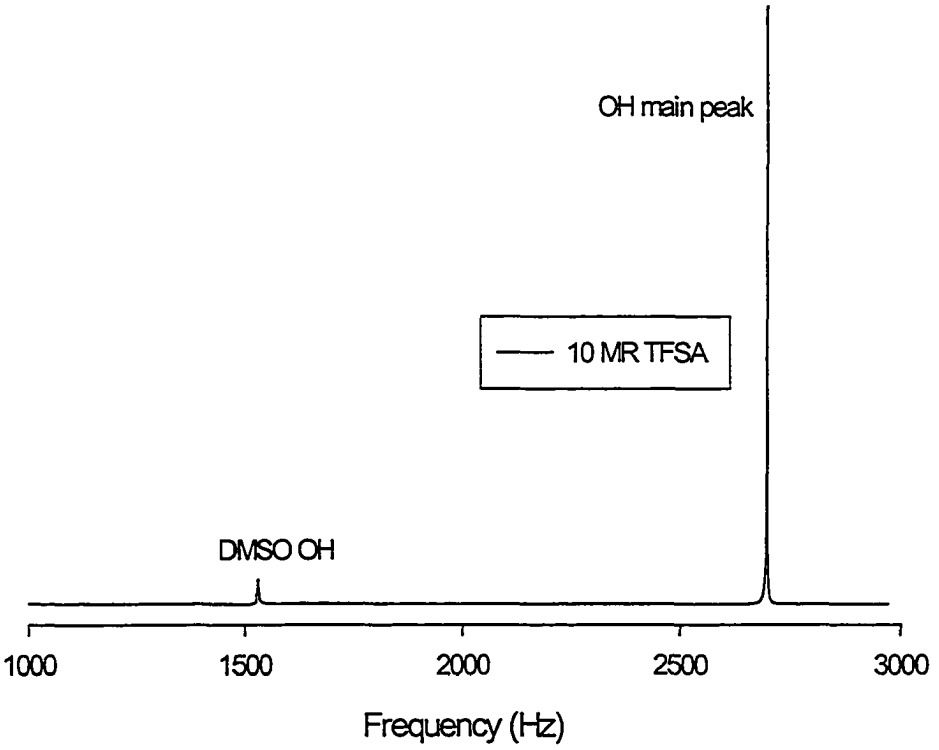

Figure 4-4(c). ^{1}H NMR spectrum of 10 MR TFSA with DMSO as the external lock.

The main peak is due to the protons from both the cation's primary and secondary solvation spheres, and those of the bulk water environment. The presence of a single peak signifies fast exchange between the various proton environments. In order to observe separate peaks for each environment the rate of exchange between the environments must be slow compared with to the NMR timescale, in addition to having the electron spin relaxation time being short compared with the hyperfine interaction between the electron cloud and the relevant nucleus. Over the concentration range investigated no splitting was observed for the various proton environments. It is expected

that an increase in concentration results in an increase in interactions between the ions, thus there should be a reduction in the fast exchange process between the bulk and solvation protons. However, at the temperature studied (30°C) no such effect was observed.

J-coupling was observed between the Ortho and Meta proton pairs on the PTSA ring. This is shown in Figure 4-4(d) for the Meta protons. Average coupling constants ranged from 14-18 Hz, and was concentration independent. This indicates that the ring part of the anion is uninvolved in the solvation process. This is supported by MD simulation results [45], which shows the charge being localized on the ring and the solvation process being accomplished through the SO_2-OH group. The magnitude of the coupling constants falls within the range (0-30 Hz) of geminal coupling (^2J) for both H-H and C-H bonds and that of vicinal (^3J, 0-18 Hz) H-H coupling. While it is possible that the protons and carbons may couple it seems more likely that if such an interaction were to occur that it be through direct bonding (^1J) as opposed to a ^2J kind. Because of this, the more likely explanation is a bonding between the Meta and Ortho proton pairs on the ring, which would result in ^3J coupling. Due to the symmetry of the PTSA molecule as shown in Figure 4-4(e), the Meta protons are equivalent, as are the Ortho proton. Each pair will view the other as an in-equivalent neighbor, and will split according to the multiplicity rule resulting in doublets ($2nI + 1$ lines) for each pair. This is shown for the Meta proton pair in Figure 4-4(d).

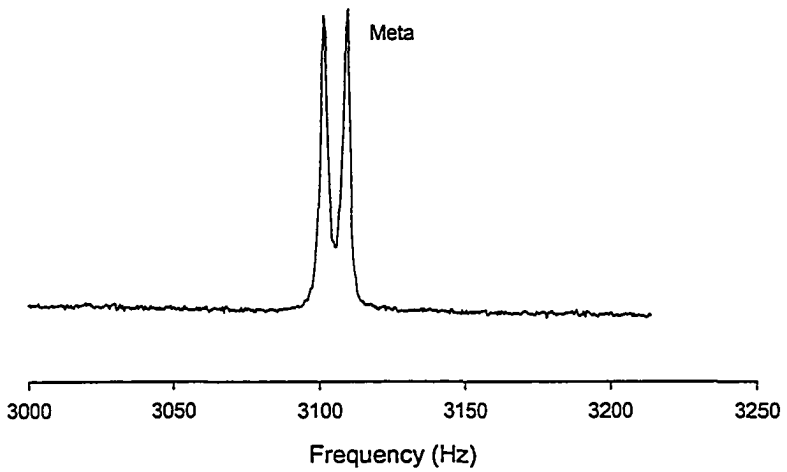

Figure 4-4(d). ^{1}H NMR expanded spectrum of the Meta proton of the PTSA ring.

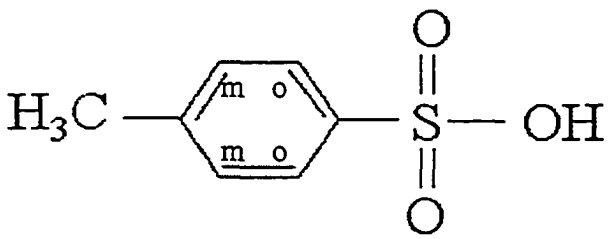

Figure 4-4(e). The chemical structure of PTSA.

4.3. Chemical Shift

As previously mentioned, a single peak was observed that was independent of concentration and due to all OH species present in the solutions. Because no splitting was observed between the chemically inequivalent proton environments, cation and anion solvation numbers were unobtainable.

The OH chemical shifts taken at 500 MHz with respect to the 0.1% proton signal in DMSO are shown in Figure 4-5, and they increased as a function of concentration, going from about 1.5 to 7 ppm over the range investigated. As shown in regions 1 and 2, there was only moderate increase in the chemical shift as the acid concentration increased. TFSA experienced the greatest shift to higher field, with that of PTSA being the lowest. This indicates greater de-shielding for TFSA compared with PTSA, and is attributed to the different chemical structure of the acids. Whereas the PTSA system has the hydrophobic benzene ring, the TFSA has the very electronegative TFSA anion. The result of this is that the free water molecules in the PTSA system are more able to interact and solvate the cation groups, therefore they experienced less de-shielding. Thus the chemical shift of the OH groups were as follows: TFSA > TFSI > PTSA.

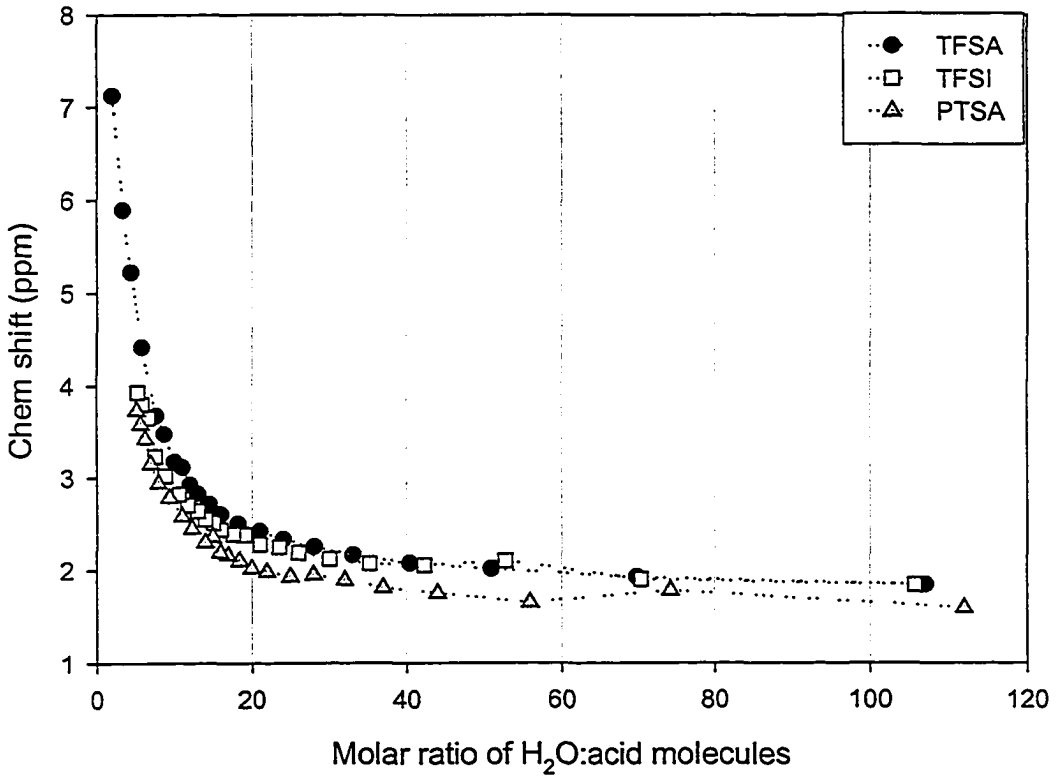

Figure 4-5. ^1H NMR chemical shift at 500 MHz with DMSO as the reference.

Compared with TFSA, the TFSI acid had smaller chemical shifts. This can be understood as follows. The TFSI anion affords greater charge delocalization, thus the anions are less interactive with each other or with the cations than in the TFSA system. This is supported by MD simulation [46] results, which showed that the negative charge of the anion is centralized on the SO_2NSO_2 skeleton, which accounts in part for the greater charge delocalization and less ion-pair formation. The TFSI cations are less de-shielded than that of TFSA, as demonstrated by the chemical shifts. This suggests that the TFSI anions are less solvated than that of the TFSA and that the excess water molecules form part of the bulk water, which screens the cations.

The effect of concentration on the chemical shifts of the anion in the PTSA system is shown in Figure 4-6(a). For comparison the OH results are also included. The general trend observed for the anion was a decrease in the chemical shift with increasing acid concentration. This says that the anions are becoming more shielded as the concentration increases. Therefore the water molecules are solvating the anions more so than the cations. Again this is supported by MD simulation results [45] that showed the tendency of PTSA to form contact-ion pairs with less than 6 water molecules present. In addition to this, experimental evidence [26, 37] has shown that a minimum of 6 water molecules is necessary to solvate protons in aqueous solutions. One therefore expects that below this number the anions are being solvated more by the undissociated acid molecules that by the water molecules.

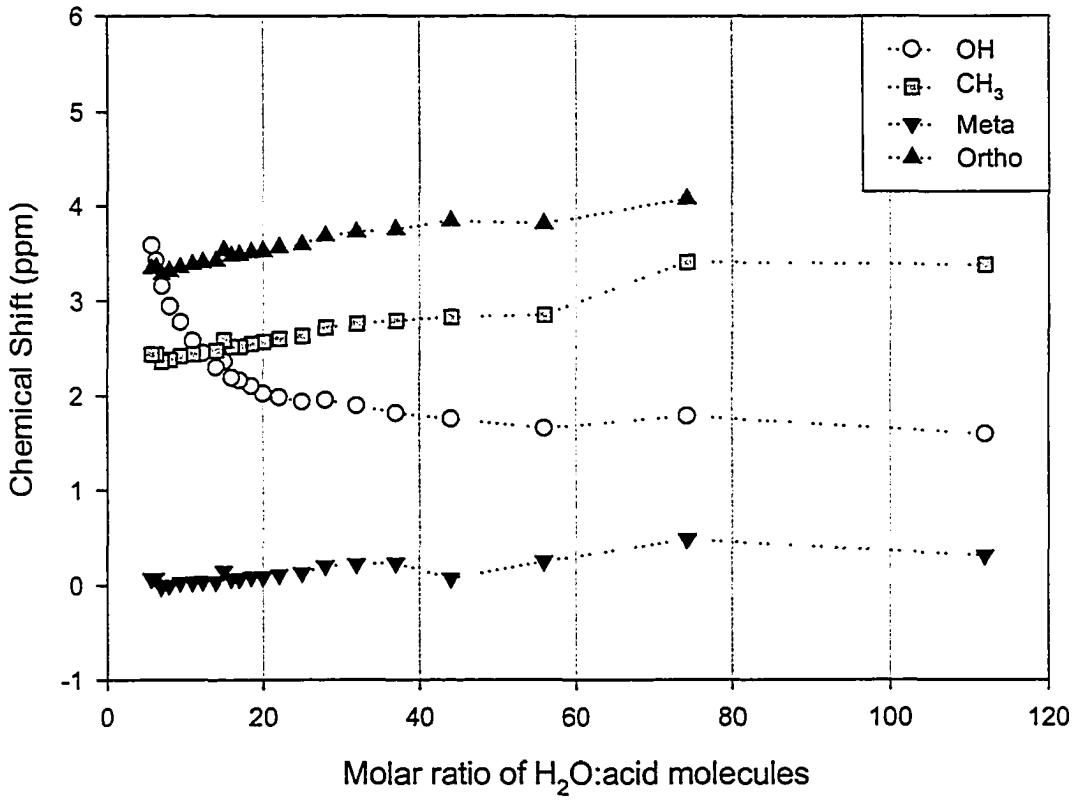

Figure 4-6 (a). ^{1}H NMR chemical shifts for PTSA obtained at 500MHz.

The ^{19}F chemical shift for TFSA and TFSI obtained at 300 MHz are displayed in Figure 4-6(b). The ^{19}F reference was a saturated $LiCF_3SO_3$ solution in water centered at 0 ppm. Again the chemical shift of the anion was observed to decrease with increasing acid concentration, as for the PTSA system. The TFSA anion chemical shifts were greater than that of TFSI, indicating that the TFSI anion is more shielded than that of TFSA. In addition to this, the TFSA anion appears to be more affected by the reduction in solvent molecules, experiencing a larger decrease in chemical shift than that of TFSI. Again this point to TFSI's reduced dependence on the presence of water molecules.

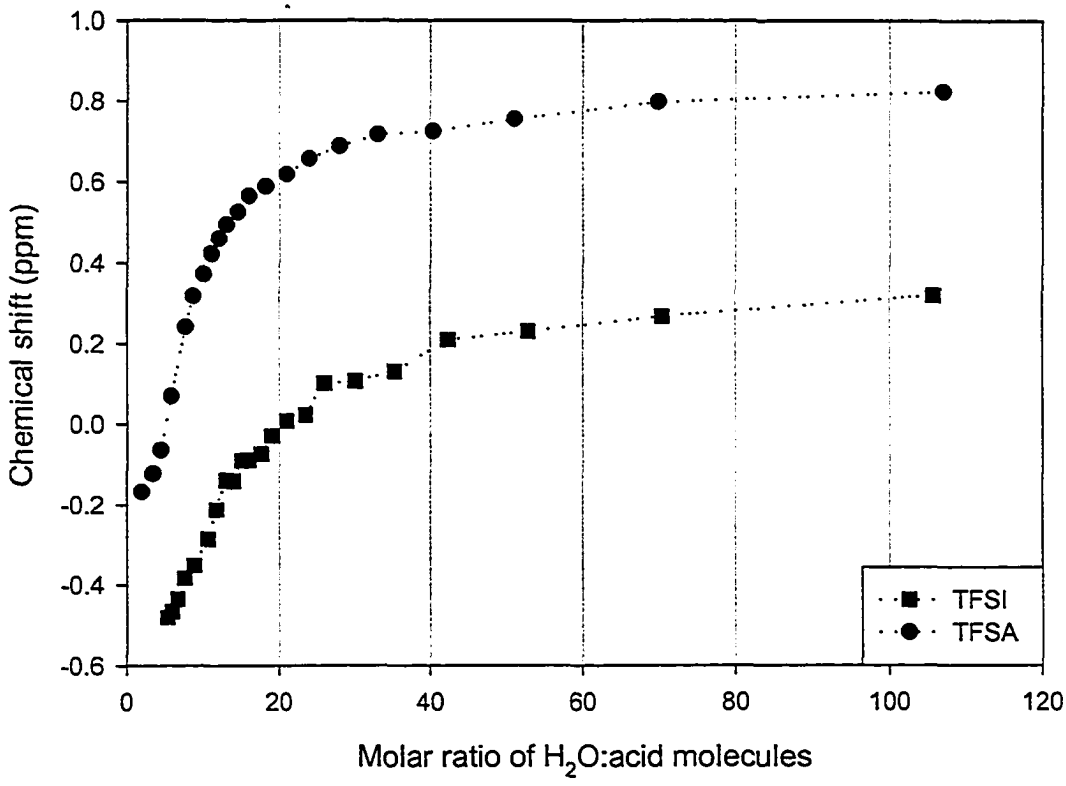

Figure 4-6 (b). ^{19}F NMR chemical shifts for TFSA and TFSI obtained at 300MHz.

4.4 Self-diffusion Coefficients - D

The proton D results for the anion and OH species for the three superacids are shown in Figures 4-7 (a) and (b). The general trend observed for both the anion and OH groups was a decrease in D as the acid concentration increased. This behavior is expected since the viscosity of the solutions was observed to increase with concentration, thereby reducing D.

For each superacid the OH D's were greater than that of its respective anion, at most by a factor of 2, with the difference decreasing as the concentration increased. The

OH D's ranged from 0.1 - 2.6 x 10^{-5} cm^2/s, with only modest differences between the three superacids, except in regions 2 and 3 where TFSA gave D's higher than both TFSI and PTSA. The anion D's ranged from 0.1 - 1.5 x 10^{-5} cm^2/s, where again TFSA had the higher D in regions 2 and 3.

Minima in D were observed for both the OH and the anion species in regions 2 and 3, the location of which appeared to be acid dependent. Such minima are an indication of restricted local motion that may be accompanied by an increase in viscosity as predicted by the Stokes-Einstein equation. While there was a general increase in viscosity for the superacids, no maxima were observed such as might have been expected from the behavior in D. This suggests that the origin of such restriction may be ordering on a local scale as opposed to the formation of large clusters. This is in contrast to minima in D that was observed for phosphoric acid/water system, and attributed to large cluster formation [47]. Similar fluctuations were observed in the T_1 results, which are discussed below.

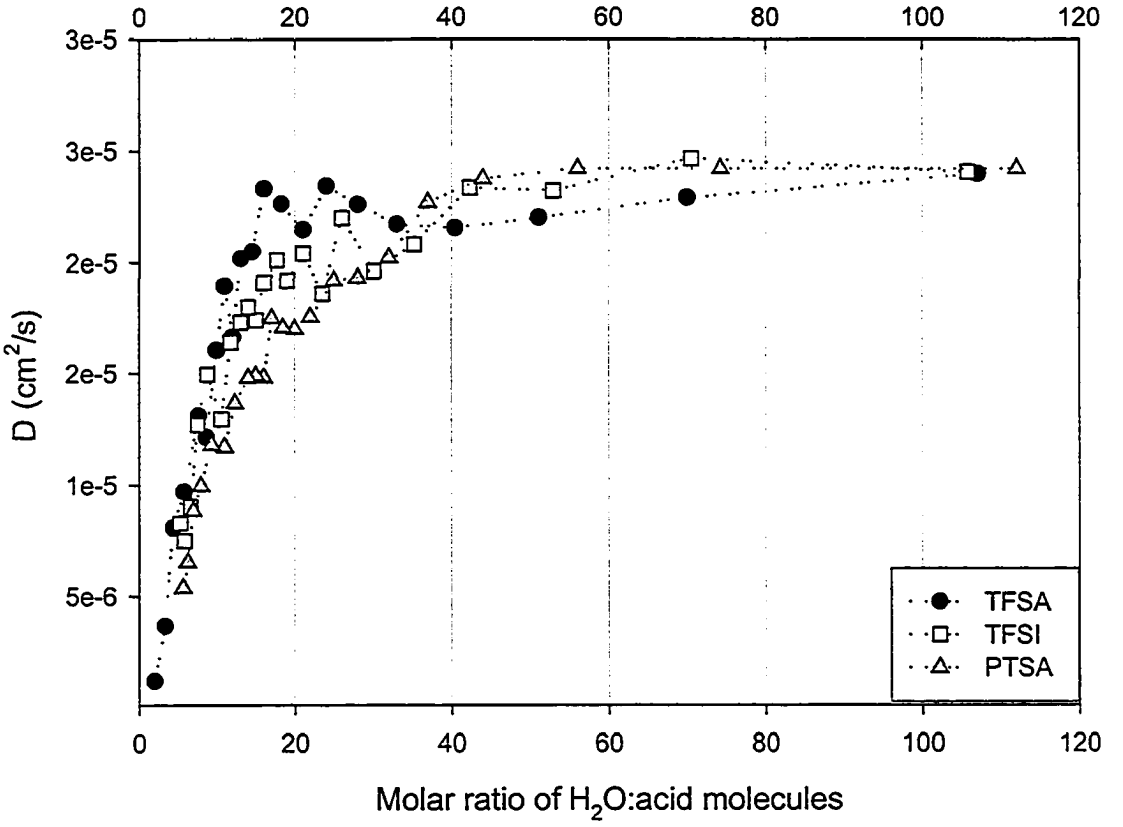

Figure 4-7(a). Proton D's for TFSA, TFSI, and PTSA.

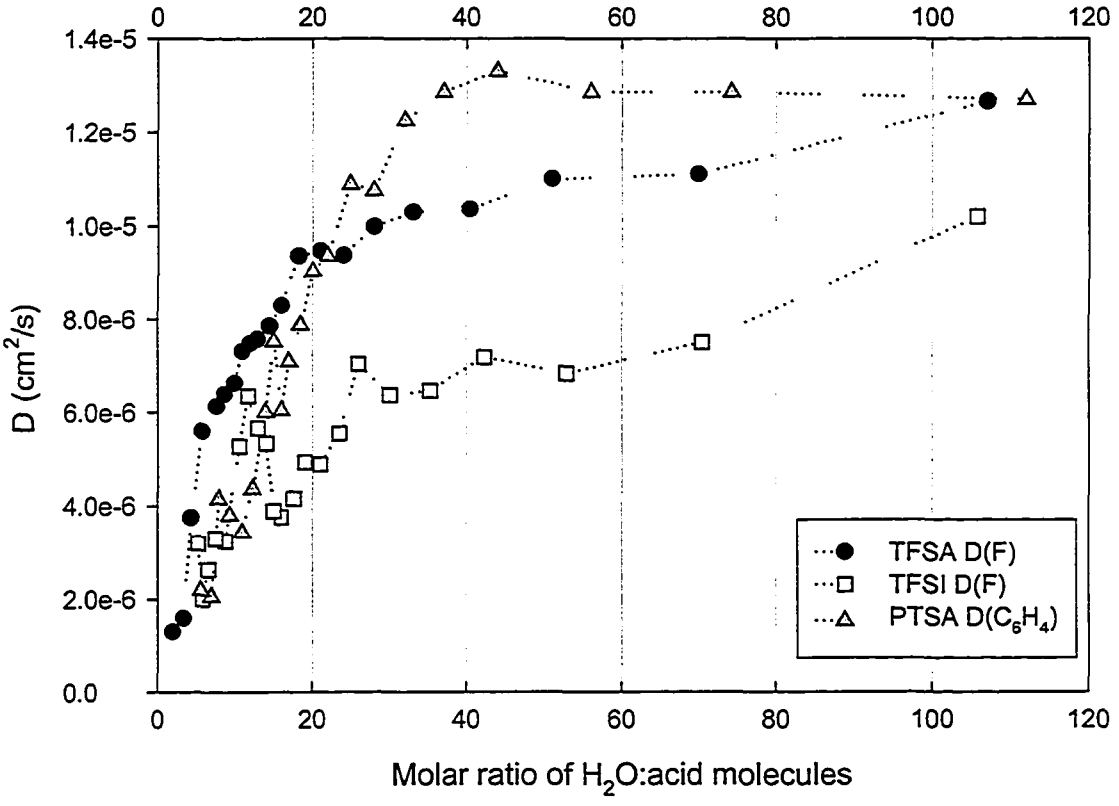

Figure 4-7(b). Anion D for TFSA, TFSI, and PTSA.

4.5 Spin-lattice relaxation times - T_1

The spin-lattice relaxation times taken at the ^1H frequency of 300 MHz for both the OH and anion species of the three superacids are shown in Figure 4-8 (a) and (b). The general trend observed was a decrease in T_1 for both the OH and the anion as the concentration increased. This type of behavior is expected since the solution viscosity is increasing with concentration, thus the motion of the nuclei become more hindered. The OH T_1's ranged from 0.2 - 3.7s and like D showed fluctuations that were concentration dependent. Minima were observed at about 40, 20 and below 20 MR for the OH groups.

The anions T_1 however, ranged from 0.4 - 5s, and did not display such a strong dependence on concentration, displaying only modest minima and plateaus in regions 2 and 3.

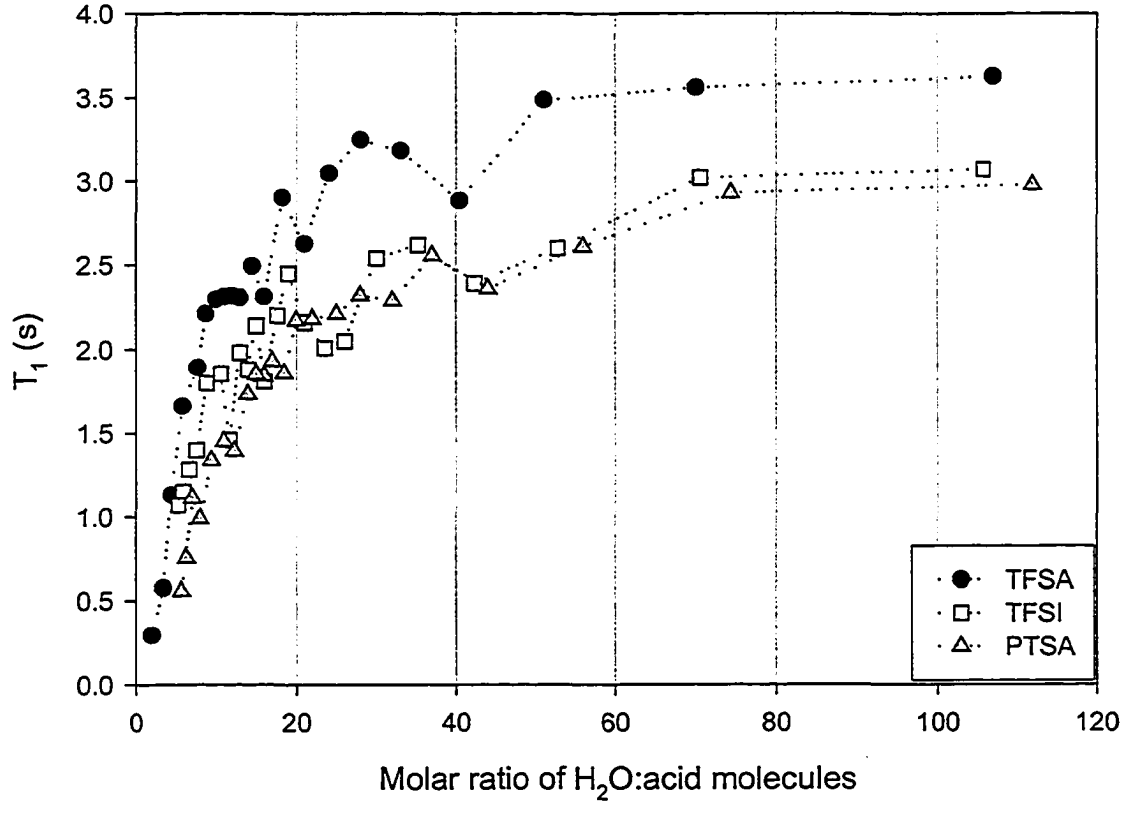

Figure 4-8 (a). Proton T_1 for TFSA, TFSI, and PTSA.

A comparison of both the OH and anion T_1 showed that of TFSA being longer than both TFSI and PTSA. Minima and plateaus in regions 2 and 3 were observed in the OH T_1 profile, whereas the anion's showed only modest changes in the slope. The

plateau observed between 10 and 16 MR was however, common in the anion profile as well.

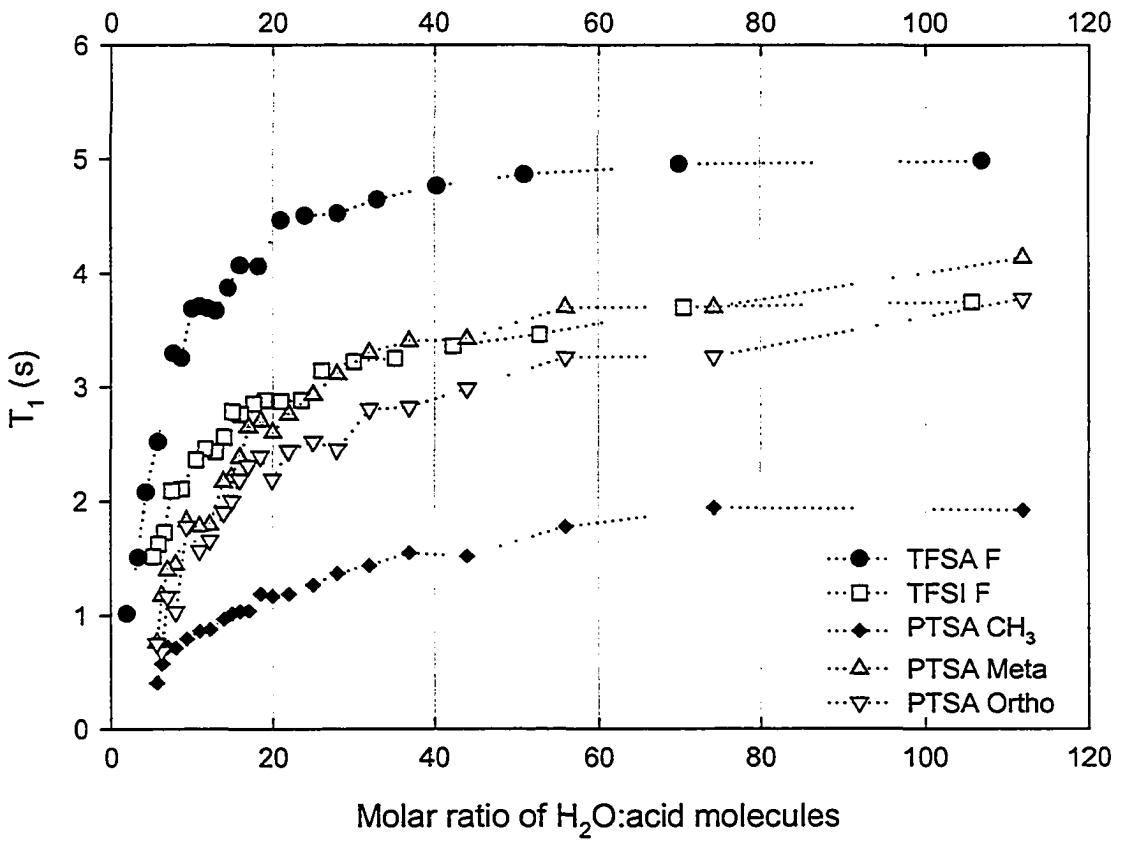

Figure 4-8 (b). Anion T_1 for TFSA, TFSI, and PTSA.

The TFSI anion profile displayed a plateau that extended from about 15 - 24 MR that was not observed in the OH profile. The Ortho and Meta signals of the PTSA anion gave longer T_1's than the methyl group, except at the very high acid concentrations where the values became similar.

4.6 Viscosity measurements

Density and viscosity results for the three superacids are shown in Figures 4-9(a) and (b) respectively. Solution density measurements were necessary in order to properly calculate the solution viscosities. The general trend observed for the density was an increase as the solution concentration increased. Results show the TFSI and TFSA solutions being the most and least dense of the three superacids respectively. Manufacturer values of density for TFSA and PTSA are 1.69 and 1.24 g/ml respectively. From the results, it was observed that as the acid concentration increased, the density approached that of the pure acid. No published value was available for the pure TFSI at the time of writing but from the trend observed for TFSA and PTSA, it would be correct to assume that the density of the pure TFSI falls within the range of 1.5 - 1.6 g/ml.

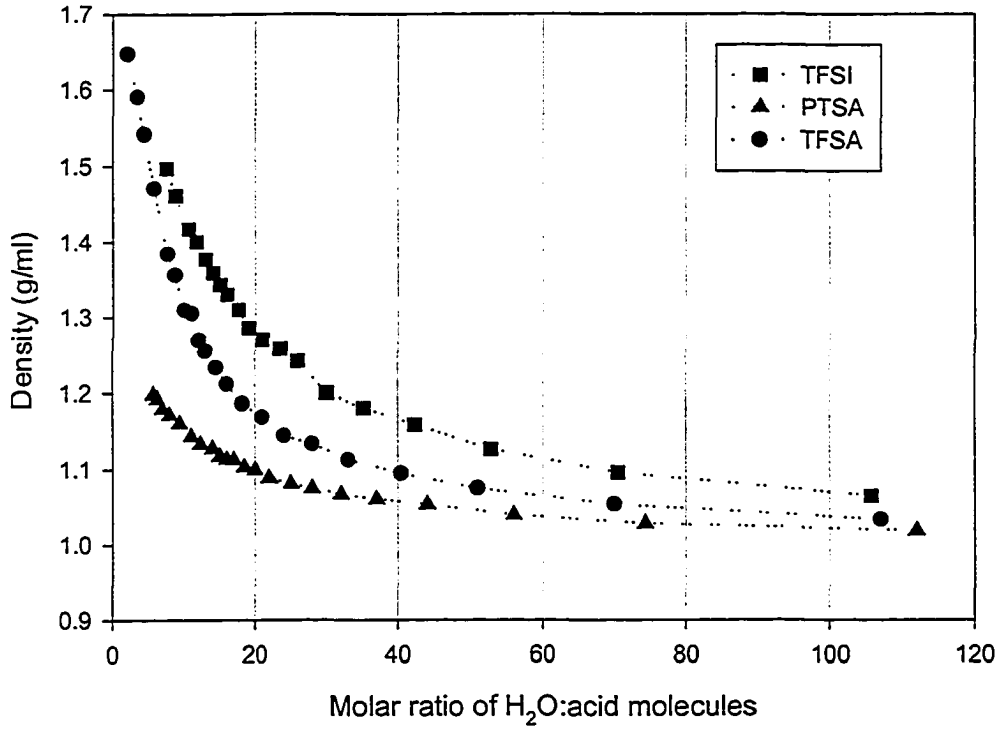

Figure 4-9(a). Density results for TFSA, TFSI and PTSA.

Viscosity results are shown in Figure 4-10(b). As with the density results the general behavior of η was to increase with acid concentration. Of the three superacids TFSA was the least viscous. As mentioned previously no maxima were observed for any of the superacid solutions. Below 5 MR the viscosity of TFSA approached 20 cP. Again it is not possible to compare this behavior with TFSI and PTSA in this range because of solubility limitation.

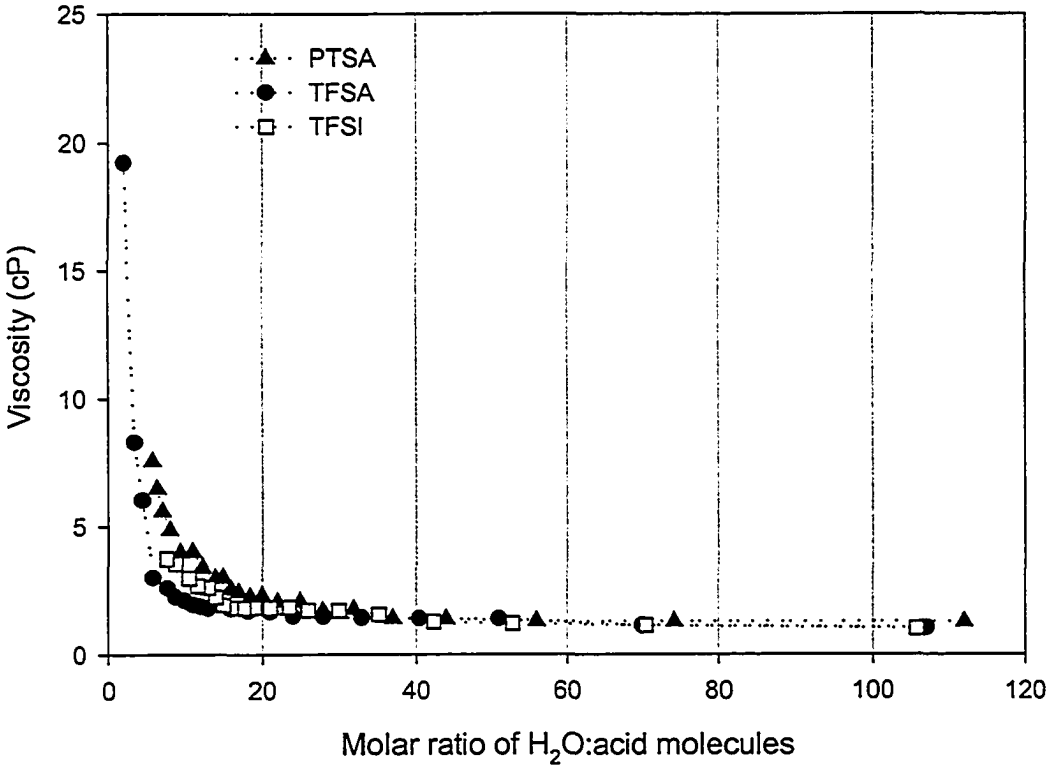

Figure 4-9(b). Viscosity results for TFSA, TFSI, and PTSA.

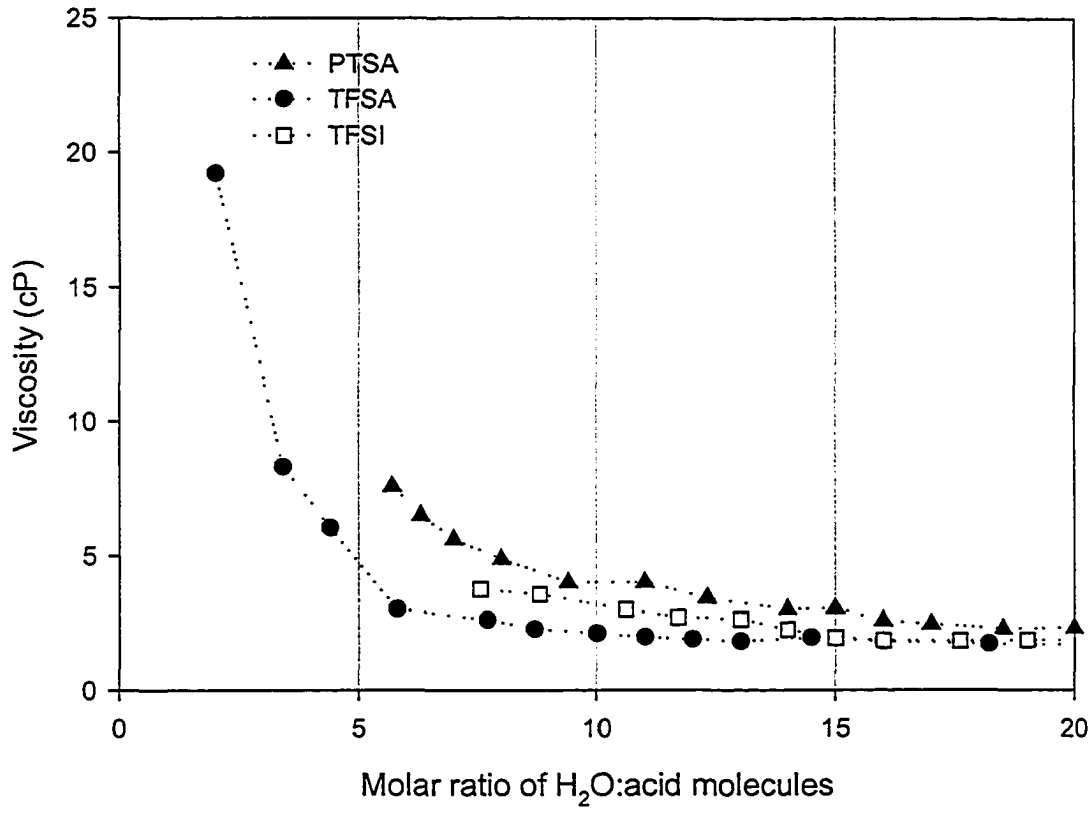

Figure 4-9(c). Expanded range of η for TFSA, TFSI and PTSA.

4.7 TFSA

The self-diffusion coefficients for the anion and OH of the TFSA system are displayed in Figure 4-10(a) and (b). The OH self-diffusion was greater than that of the anion by about a factor of 2 over almost the entire concentration range investigated. This is an indication of the difference in size and transport mechanism of the anion and OH species. This factor approached 1 however at very high acid concentrations, specifically below 5 MR and indicates the coupling of the anion and OH groups. The OH D's were more affected by concentration effects than those of the anion. This behavior was also observed in the T_1 measurements.

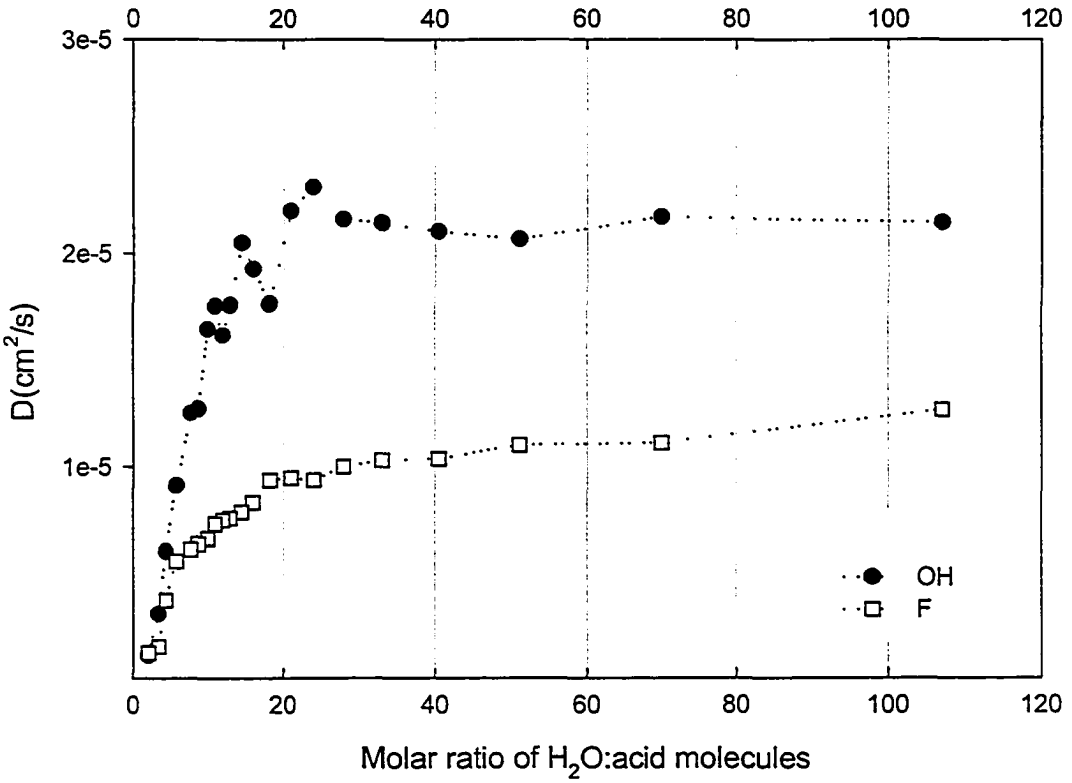

Figure 4-10(a). Anion and OH D for the TFSA system.

The T_1 measurements for the TFSA system are shown in Figure 4-10(b). The anion T_1's ranged from 1 – 5s depending on the concentration. The anion T_1's showed a moderate decrease in regions 1 and 2. However, in region 3 this changed to a steeper decline. The OH T_1's showed fluctuations that was present at both 300 and 500 MHz. T_1 values at 300 MHz were greater than at 500 MHz in regions 1 and 2. At higher acid concentrations (region 3) however, there was little difference between them. Both the anion and OH T_1's show a plateau in region 3 followed by a dramatic decrease. The

position of the plateau coincides with the region of σ maximum observed for TFSA as shown in Figure 4-10(c).

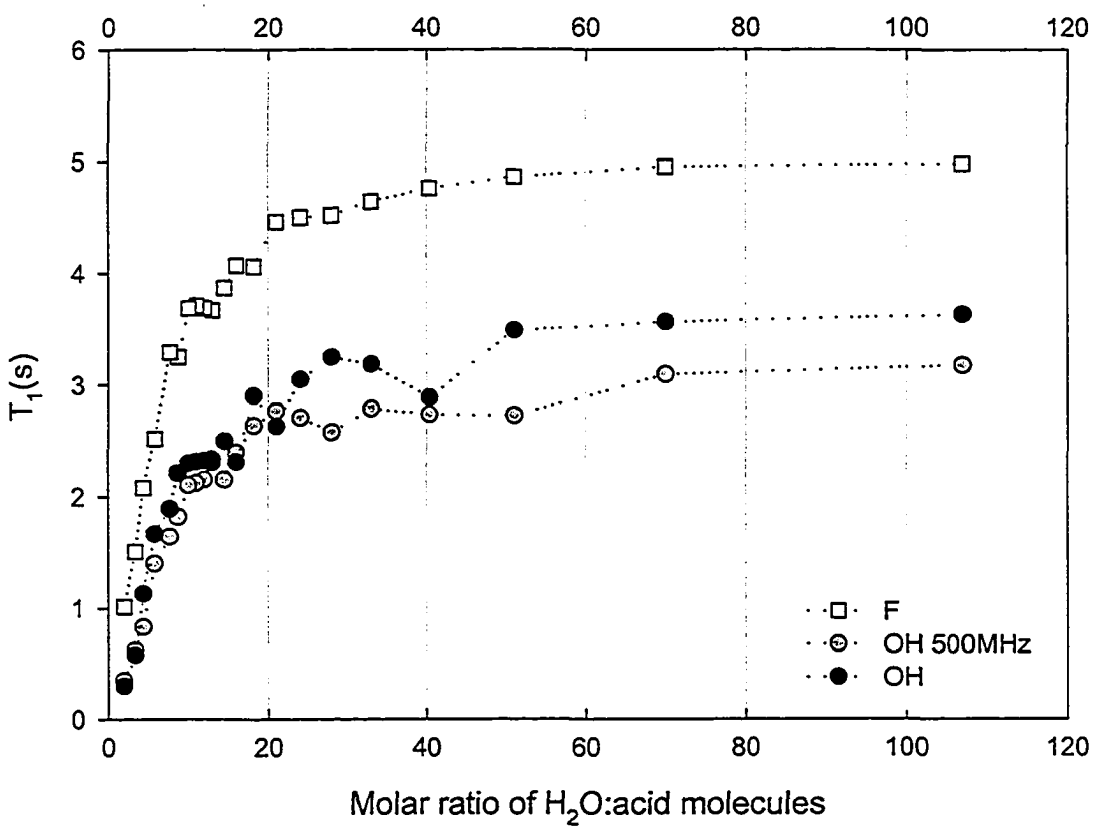

Figure 4-10(b). Anion and OH T_1 for the TFSA system.

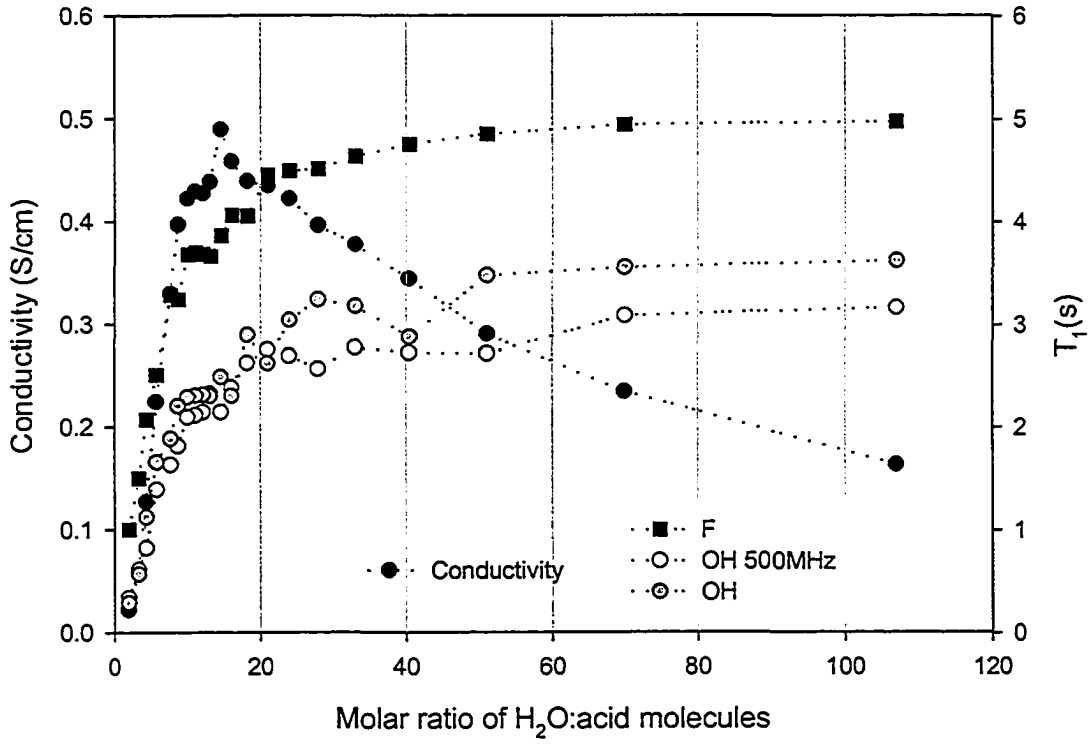

Figure 4-10(c). Conductivity and T_1 for the aqueous TFSA solutions.

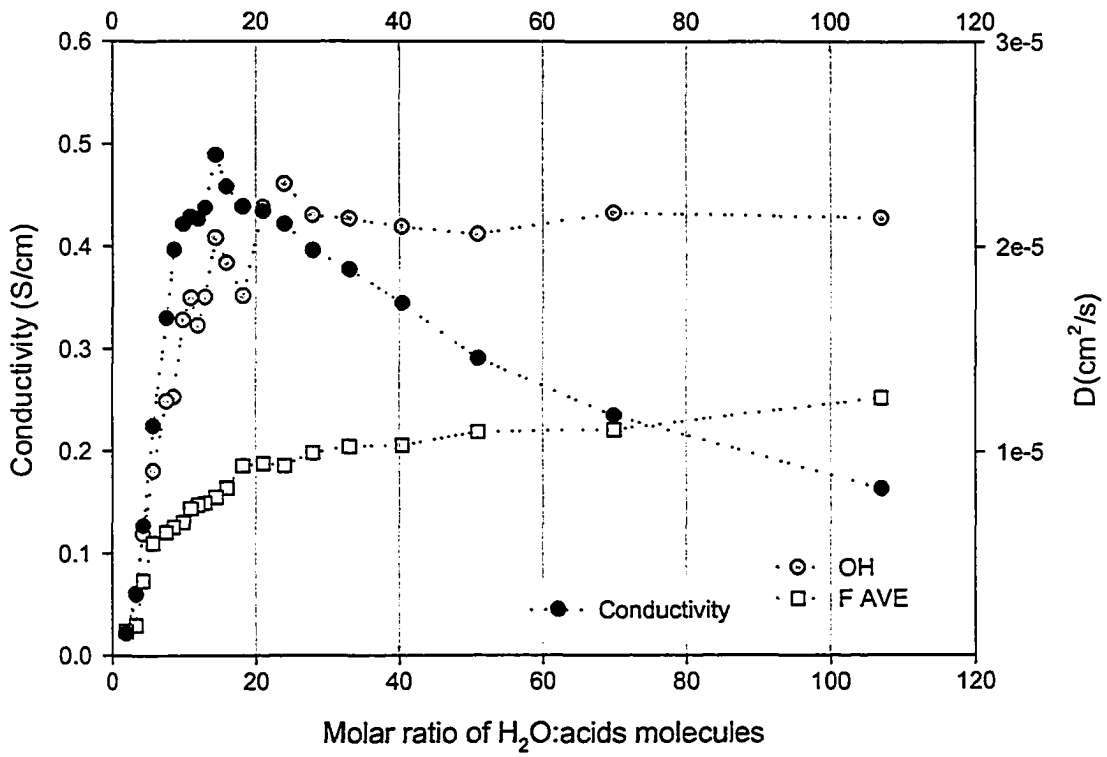

Figure 4-10(d). Conductivity and D for aqueous TFSA solutions.

4.8 TFSA Monohydrate

Measurements of D and T_1 for the TFSA monohydrate are given in Table 4.1. In its monohydrate form there is less heterolytic ($HA \rightarrow H^+ + A^-$) dissociation of the acid molecules into charged ions. Thus there is a greater amount of undissociated acid molecules that are able to solvate the cations and the anions, and ultimately play the role that water does in aqueous solutions of low to moderate acid concentrations. A comparison of D for the OH and anion groups indicates a coupled motion. In addition to this the D values for both groups are far greater than observed for aqueous solutions with MR < 5. This suggests that the undissociated acid molecules provide better screening than water as a solvent.

TFSA	D (cm^2/s) x 10^{-6}	T_1 (s)
Cation	8.0	5.17
Anion	6.6	3.47

Table 4.1. D and T_1 of TFSA monohydrate at 30°C.

4.9 TFSI

D and T_1 results for TFSI are shown in Figures 4-11(a) and (b) respectively.

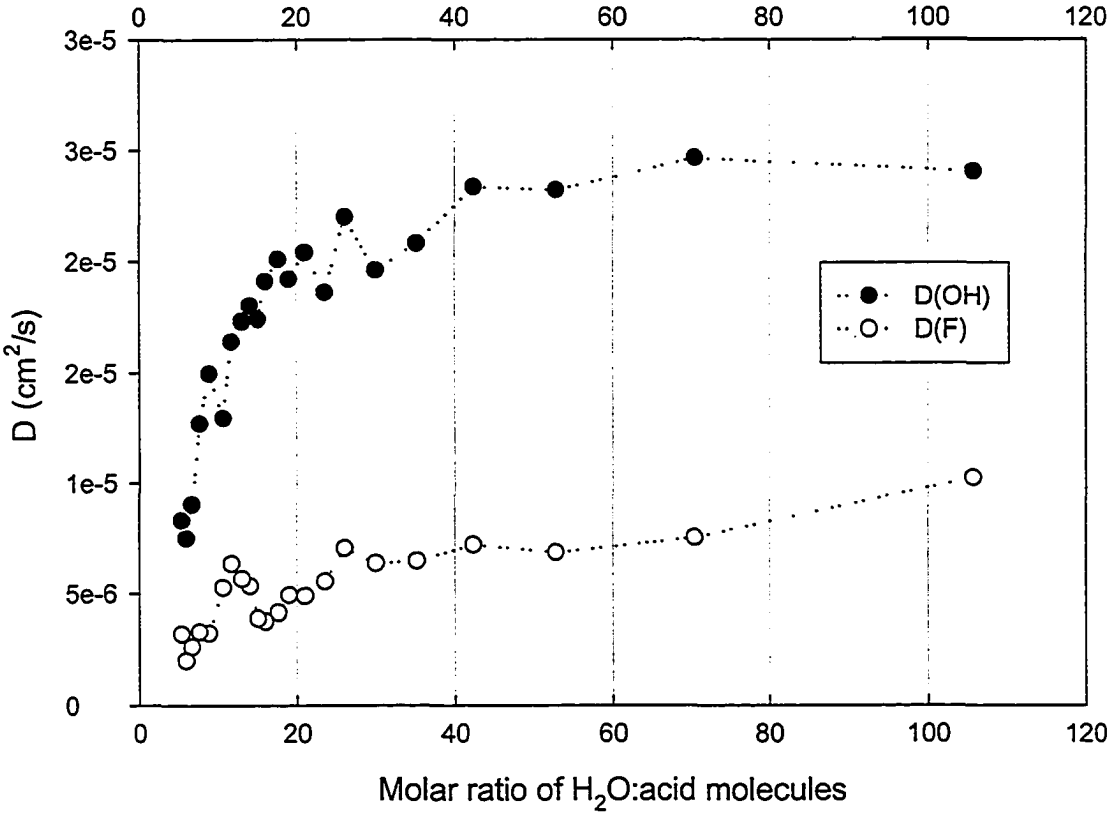

Figure 4-11(a). Anion and OH D for aqueous TFSI solutions.

The OH D was greater than that of the anion over the entire concentration range. No merging at very high acid concentrations was observed as for the TFSA system, indicating the ability of TFSI to maintain larger distances (250 – 260 pm) [46] from the solvated protons necessary for ionic mobility. The anion D showed a broad minimum in the range of 15 - 27 MR, which corresponds with the maximum observed in the ionic conductivity, as shown in Figure 4-11(c). The OH D did not show this feature, however, the T_1 results at both 300 and 500 MHz displayed fluctuations.

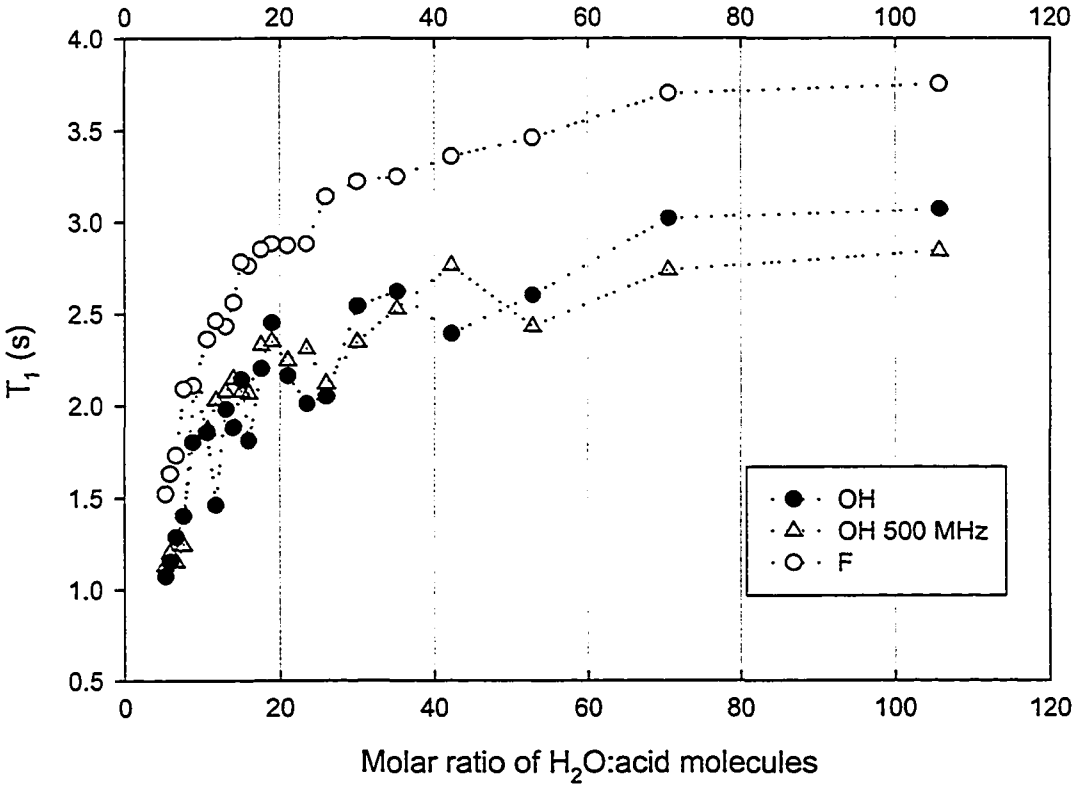

Figure 4-11(b). Anion and OH T_1 for aqueous TFSI solutions.

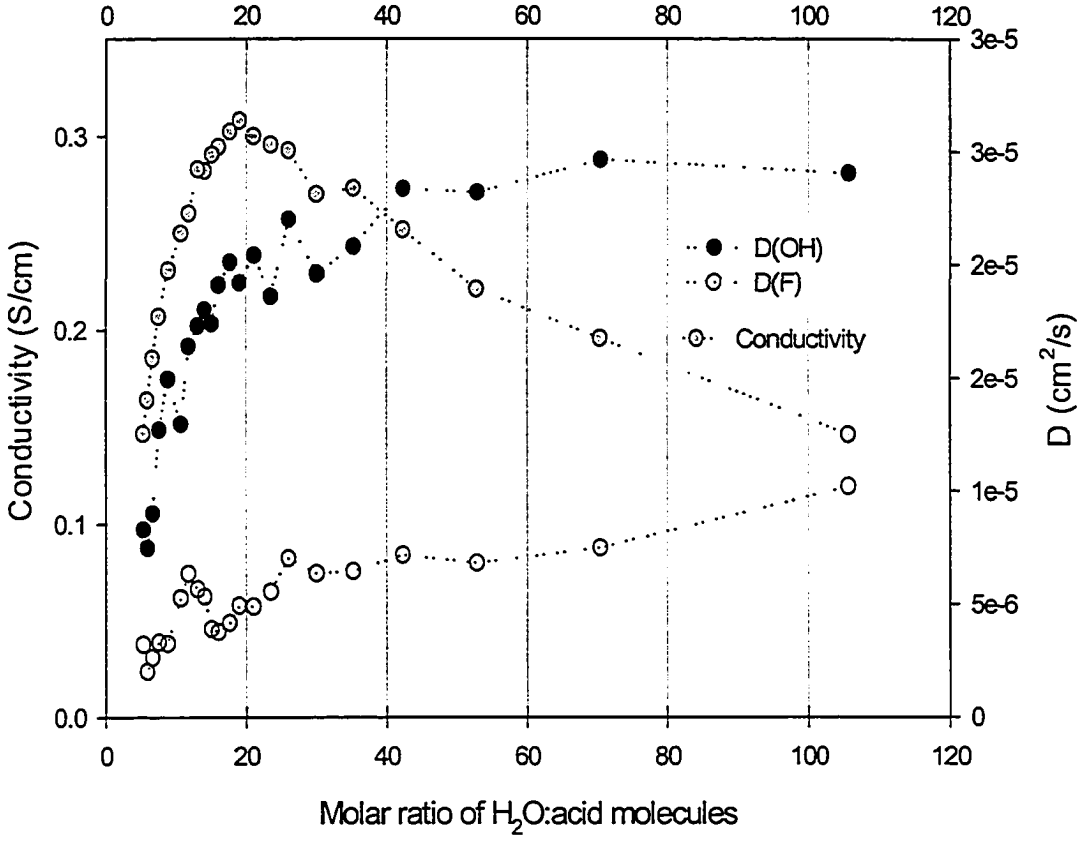

Figure 4-11(c). Ionic conductivity and D for aqueous TFSI solutions.

4.10 PTSA

Results for D and T_1 are shown in Figures 4-12(a) and (b) respectively. As with TFSA and TFSI, the OH D was greater than that of the anion, except at the very high acid concentrations.

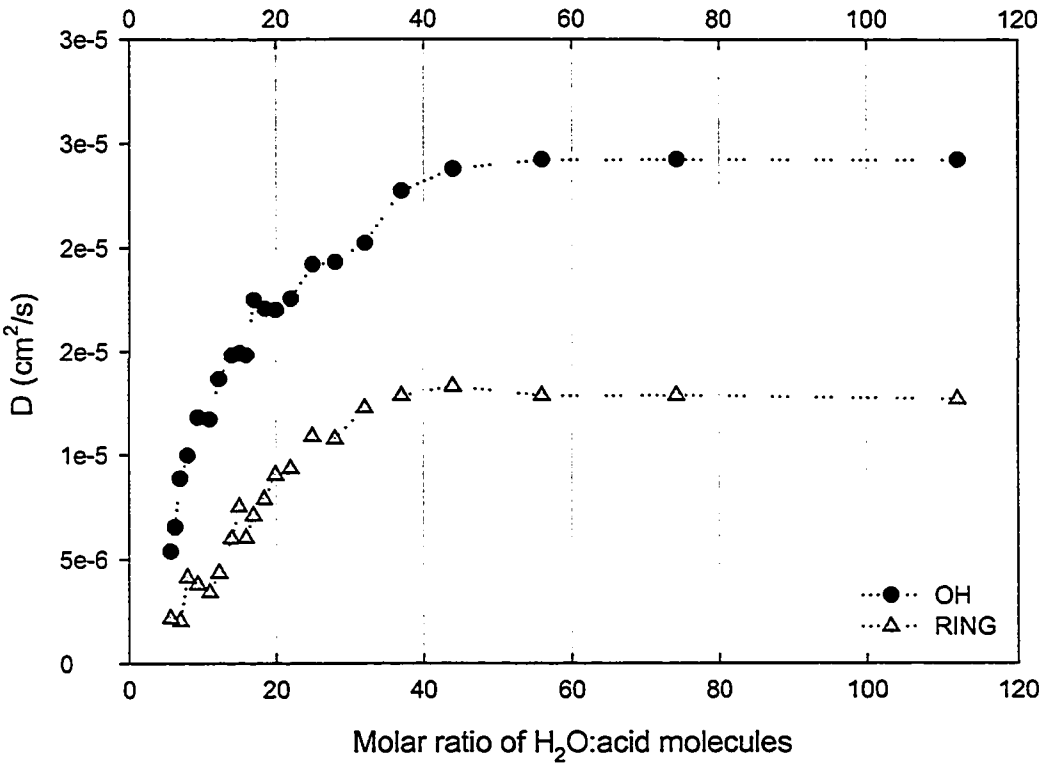

Figure 4-12(a). Anion and OH D for aqueous PTSA solutions.

The difference in D between the anion and OH in this range was less than that of the TFSI system. This is again an indication of the TFSI's ability to maintain larger separation distances between the solvated protons and the anions over both TFSA and PTSA.

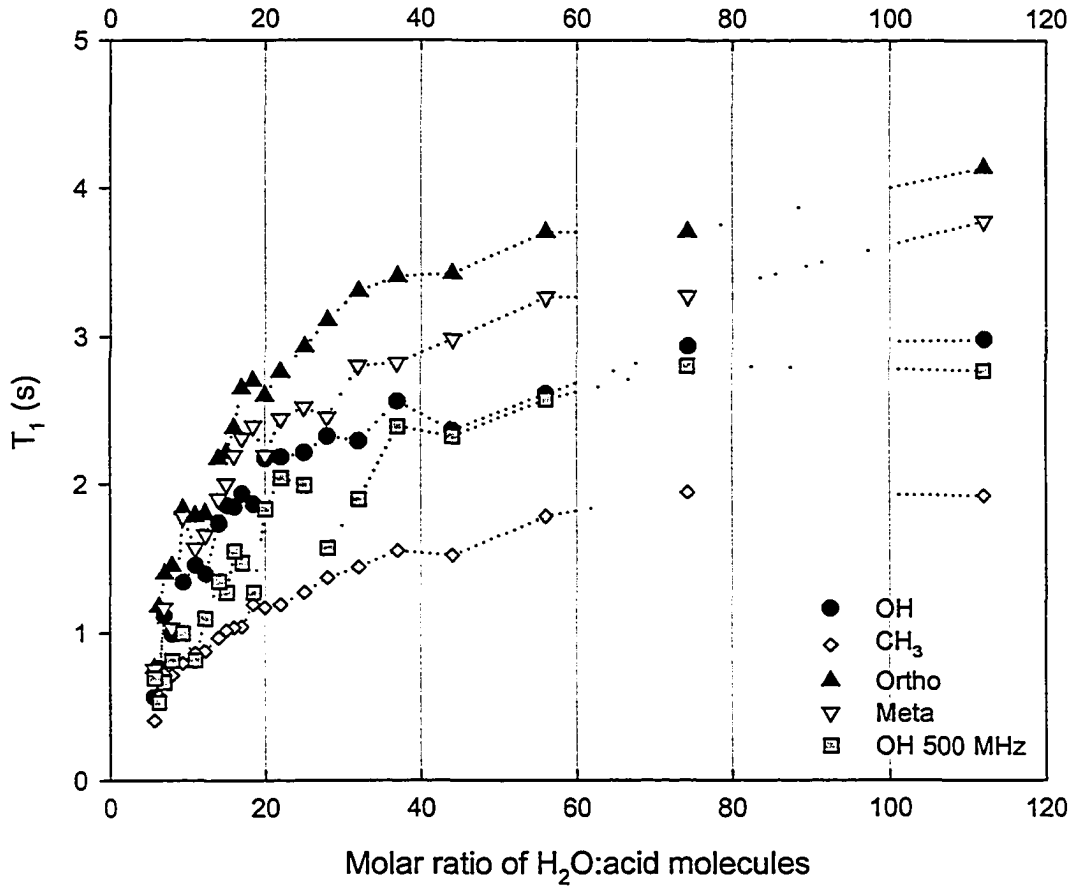

Figure 4-12(b). Anion and OH T_1 for aqueous PTSA solutions.

In region 1 there was very little change in both the OH and anion D. However that changed in regions 2 and 3, where the OH and anion D's went from about 2.5 to 0.5 $x10^{-5}$ and 1.2 - 0.2 x 10^{-5} cm^2/s respectively. Plateaus were observed in the OH D's between 10 - 25 MR and corresponds with those observed in both the anion and OH T_1's, and D as shown in Figures 4-12(b) and (c).

The ring protons of the anion had longer T_1's than both the OH and CH_3 groups, except at the very high concentrations, where they merged. The CH_3 group T_1 appeared insensitive to much of the changes in the anion's local environment, and showed just a

general decrease with concentration. This is due to the rotation motion of the methyl group, which averages the local fluctuations, thus is unaffected for most of the concentration range. This changed however at the higher concentrations when the motion of the methyl group becomes hindered from the increasing viscosity and reduced dielectric screening. One exception to this behavior was the very high acid concentration where it gave similar value as that of the ring protons and the OH groups. This is evidence that at the very high concentrations the OH groups and anions are not well separated to prevent their interaction.

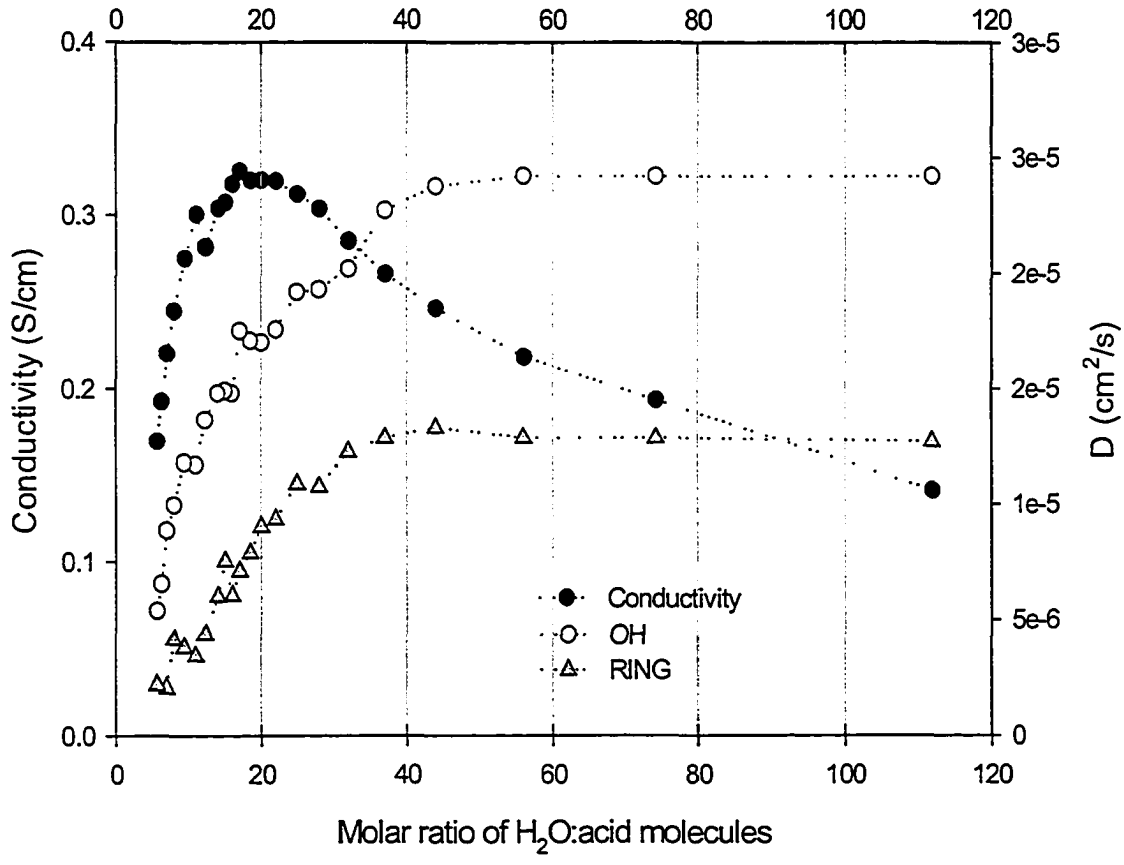

Figure 4-12(c). Ionic conductivity and D for aqueous PTSA solutions.

4.11 Discussion

The focus of this discussion will be to answer the questions asked in Chapter 1, namely what is the nature of the transport and relaxation mechanisms for aqueous superacid solutions? The transport mechanism of the ions is by way of both the Grotthuss and Vehicle mechanisms. This is supported by σ and D data as shown in Figures 4-10(d), 4-11(c), and 4-12(c) for aqueous TFSA, TFSI and PTSA solutions respectively. D is a measure translational mass transport while σ is a measure of ion

transport by whatever mechanism allowed. Correlation between D and σ is an indication of increasing Vehicular transport. For all three superacids the correlation between D and σ is observed above the maximum in σ, where the OH chemical shift and η showed significant increase, while D and T_1 experienced their greatest decrease. This may be viewed as the turning point for ionic mobility, facilitated by changes in the effective dielectric constant of the solvent.

The behavior of σ appears to be more reflected in the OH D as opposed to that of the anion. This along with the magnitude of the OH D compared with that of the anion indicates that the protons contribute more to the ionic conductivity than the anions. Due to the size of the anions their expected transport is by way of the Vehicle mechanism. The protons however may be transported by either mechanism or a combination of both. It is expected that before the turning point protons are being transported by both the Grotthuss and Vehicle mechanisms. However, this changes beyond the turning point where the decrease in D becomes more pronounced, indicating the Vehicle mechanism is being hindered by the increasing viscosity and reduced dielectric shielding. This is expected however as the Vehicle mechanism is hindered by strong bonds, and therefore will not play a significant role in reduced solvent environments. To support this point the ratio of the OH and anion D were calculated for all three superacids, the results are shown in Figure 4-13.

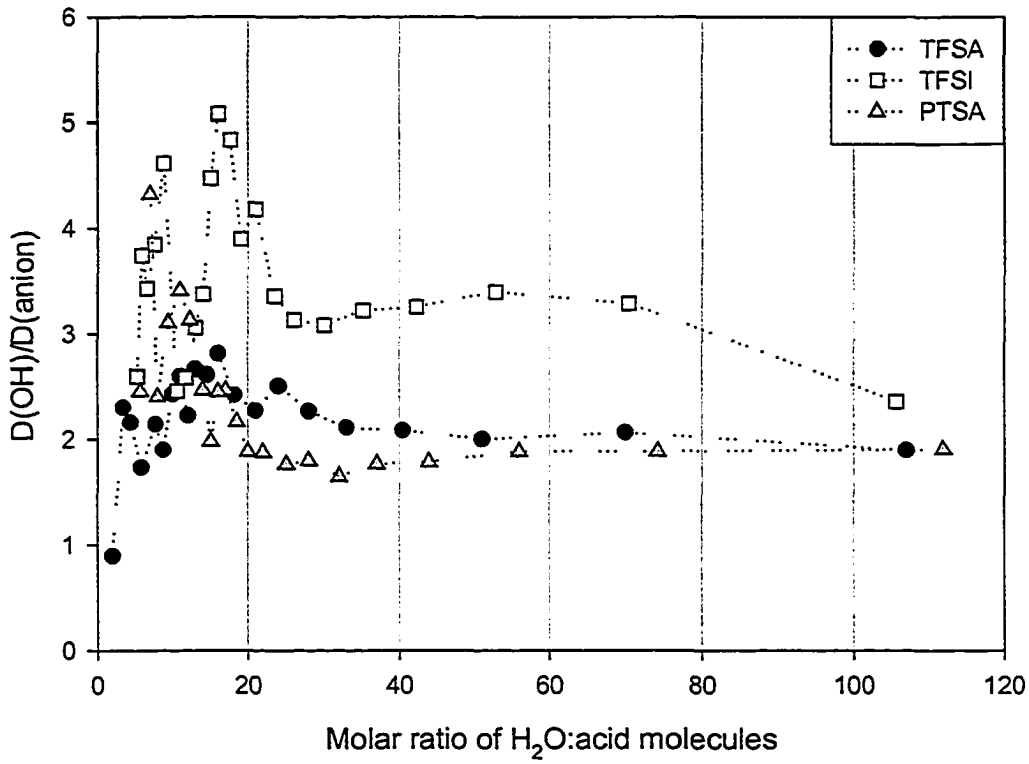

Figure 4-13. Ratio of OH and anion D for TFSA, TFSI and PTSA.

As the results show this ratio is greater than 1 except for MR< 3 obtained for the TFSA system. A ratio greater than 1 indicates a Grotthuss dominated transport mechanism [48], while a ratio of 1 supports a Vehicle mechanism. Based upon this, the Grotthuss mechanism appears more dominant.

The relaxation mechanism for spin - 1/2 nuclei are: dipole-dipole, chemical shift anisotropy, spin rotation and translational diffusion. T_1 measurements for the OH groups were done at both 300 and 500 MHz. The T_1's at 300 MHz were somewhat longer than those at 500 MHz in regions 1 and 2 and for all three acids the T_1 curve appears to be

shifted with the field. ^1H variable temperature (VT) study of 5MR PTSA at 300MHz from 0 - 60°C in 5° increment (results not shown) gave increasing T_1 with temperature. This indicates that one is one the motionally narrowed side of the T_1 minimum curve. Due to the limited temperature range of the VT study for all three superacids, proper determination of the relaxation mechanism was not possible. Despite this it can be speculated that it is a combination of all the above mentioned relaxation mechanisms.

For all three acids the behavior observed in T_1 correlates with that of D. From this it could be assumed that whatever re-arrangement taking place between the ions and solvent molecules at or beyond the turning point is long-lived (on the order of ms). This behavior of a maximum in σ has been observed for aqueous $CsCH_3COO$ solutions of varying concentrations [49]. In this system the maximum observed in σ was associated with the breakdown of the bulk water tetrahedral structure with dielectric coefficient of ~ 70-80 and coincided with the increase observed in η. Beyond this point it was shown by various spectroscopic techniques (X-rays, dielectric spectroscopy) that ionic structures and ion-water clusters were being formed as a result of the decreasing dielectric coefficient, which resulted with the system appearing glasslike. While the results presented here offer no detailed evidence of the possible ionic clusters that may be formed beyond the turning point, the fluctuations observed for both the OH groups and anions T_1 and D are an indication of local ordering in the solutions that results from the reducing dielectric constant. As previously mentioned only a single peak was observed for all OH containing groups, therefore the resulting T_1 is an average of all such contributions. Thus any fluctuation that is observed in the OH T_1 is an indication of any

changes that is taking place within the cation, ion-water and bulk water solvation network.

Based upon the information presented, the initially proposed model of aqueous acid solutions: $HA + (n+m+l)(H_2O) \rightarrow H^+\cdot(H_2O)_n + A^-\cdot(H_2O)_m + l(H_2O)$, where the protons and anions are solvated by water molecules and affords no interaction between them, must be modified. The above model is applicable below (MR > 20) the maximum in σ, which is referred to as the concentration turning point. Beyond the turning point however, the formation of ionic structure has a greater effect on the charge transport than does the increase in the number of charge carriers with increasing acid concentration. In this region the presence of ionic structures such as ion pairs, and higher aggregates is also suggested. This is supported by MD simulation results for TFSA, TFSI, and PTSA [27, 45, 46] where it was shown that the proximity between the solvated dissociated protons and anions was dependent upon the number of solvating water molecules present and increased accordingly. Beyond the turning point the separation distances are reduced, which allows for electrostatic interactions. The model may now be augmented as follows:

$$HA + (n+m+l)(H_2O) \rightarrow H^+\cdot(H_2O)_n + A^-\cdot(H_2O)_m + l(H_2O) \qquad MR > 20$$

$$HA + (n+m)(H_2O) \rightarrow [H^+\cdots(H_2O)_{n'}\cdots A^-](H_2O)_{m+n-n'} \qquad MR < 20$$

where n' decreases with decreasing n+m.

Chapter 5. Nano Porous -PCM's Results and Discussion

The goal of this research was to investigate the diffusivity of both the water (D(OH)), which is correlated with proton conductivity, and undissociated fuel molecules ($D(CH_{2,3})$), correlated with fuel crossover in the NP-PCM's. In addition to this, a replacement to methanol as a fuel was being sought. The replacement fuel should have lower permeability and should also be easily oxidized. The NP-PCM's consists of a poly(vinylidene) fluoride (PVDF) matrix, high surface area inorganic oxides such as silicates, aluminates, or titanates, and an aqueous acid (H_2SO_4) that fills the nano-pores. [10] The fuels investigated were dimethyl oxalate (DMO), ethylene glycol (EG) and methanol (MeOH). These results were published [56].

The goal of this investigation was to study the mobility of water and the methyl (CH_3) or methylene (CH_2) group associated with the fuel, in new proton conducting membranes equilibrated in aqueous solutions of 2M fuel in 3M acid. A typical ^1H spectrum of an NP-PCM equilibrated in aqueous $MeOH/H_2SO_4$ solution is shown in Figure 5-1. Indicated are the various diffusing components, namely that of water (OH) and the fuel (CH_3). Both components are well resolved thus allowing self-diffusion evaluation of each component.

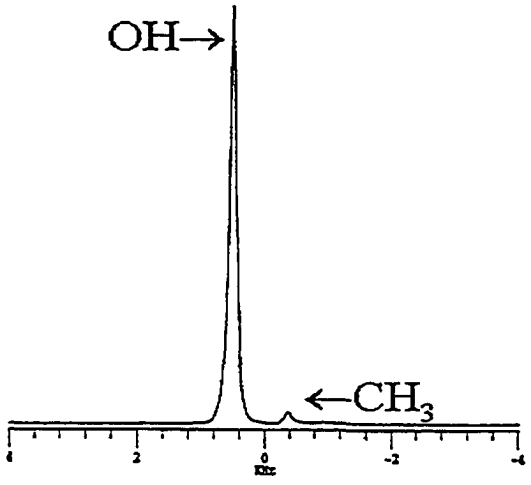

Figure 5-1. Representative ^{1}H NMR spectrum of NP-PCM B (Table 1) equilibrated in 2M MeOH in 3M H_2SO_4 solution at 303K.

Self-diffusion measurements as a function of temperature were made for three aqueous fuel/acid solutions and five NP-PCM's equilibrated in each fuel/acid solution. The aqueous solutions investigated were MeOH/H_2SO_4, EG/H_2SO_4, DMO/H_2SO_4 and the equilibrated membranes are labeled A-E. The results are arranged according to fuel type with D(OH) and D($CH_{2,3}$) representing the water and fuel diffusion coefficients. The D(OH) represents the water self-diffusion coefficient because in the 2M fuel/3M acid solutions investigated, the most dominant constituent is water, thus the major fraction of the proton signal sampled by the NMR PGSE technique is attributed to the water.

5.1. D of the aqueous solutions

Aqueous fuel/acid solutions gave the self-diffusion results higher than the NP-PCM's equilibrated in solutions. Of the three fuel/acid solutions investigated, DMO solution gave the lowest water and fuel self-diffusion coefficients for the entire temperature range, this is illustrated in Figure 5-2. At 303 K a comparison of the D(OH) for the three fuels show more than a 40% difference between DMO and that of EG and MeOH, while the $D(CH_3)$ differed by about 15%. This result is expected in DMO due to its large molecular size and correspondingly higher solution viscosity. Although it is possible that hydrolysis of DMO into oxalic acid and MeOH can occur, the consistently lower diffusivities of the DMO solution suggest that very little hydrolysis has occurred. EG solution gave D(OH) results comparable to that of methanol for the entire temperature range. $D(CH_2)$ values for EG compared with $D(CH_3)$ of MeOH are about 35% lower at 303 K and only 7% lower at 363 K.

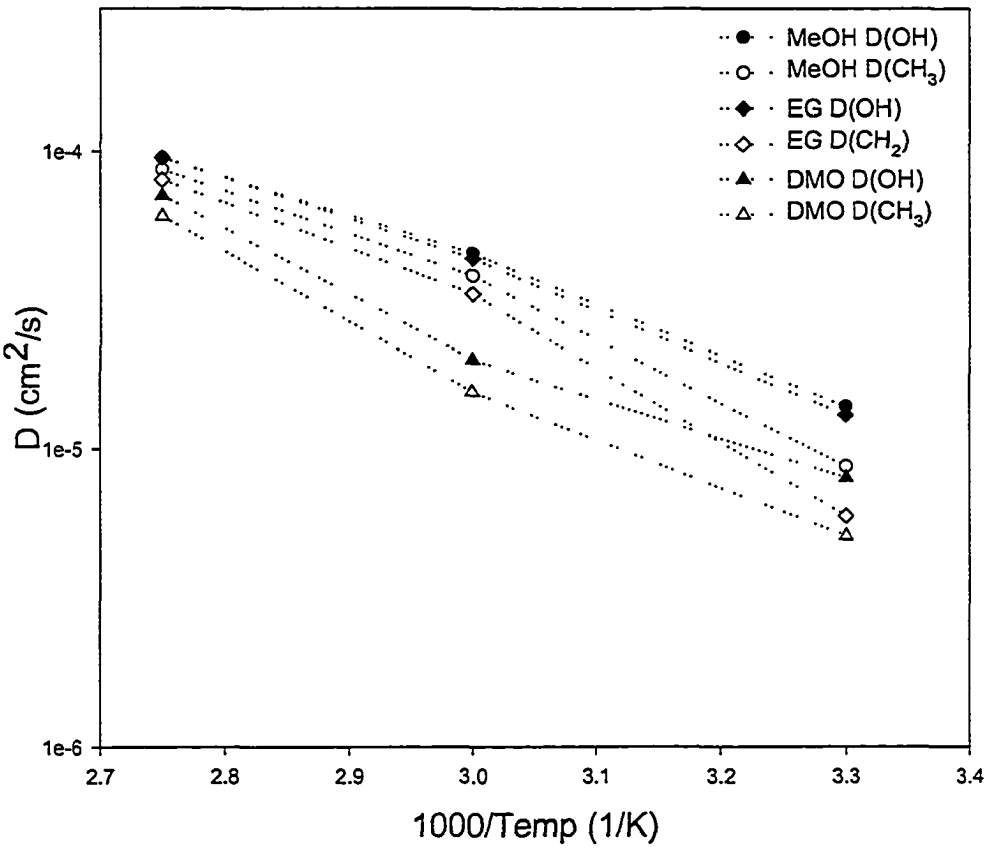

Figure 5-2. Proton D as a function of temperature in aqueous 2M fuel/3M acid solutions.

5.2 D results of the Nano Porous -PCM's

Five Nano Porous -PCM's were investigated, each in three fuel/acid mixtures. Of the five membranes, two extreme cases emerged – membrane B for giving the lowest D(OH) and $D(CH_{2,3})$ independent of fuel type, and membrane C for giving the highest D(OH) and $D(CH_{2,3})$ also independent of fuel type. Results for membranes B and C are illustrated in Figure 5-3; membrane composition data are summarized in Table 5.1. Membrane C, which gave the highest diffusion coefficients also independent of fuel type, contained 16% of the ceramic Aerosil 200. Membrane B that gave the lowest D(OH),

also independent of fuel type contained 12% of the ceramic Aerosil 130. Further comparison of the D(OH) results for the five NP-PCM's revealed that for each ceramic type the higher the concentration of ceramic the higher the D(OH). The order of membrane D(OH) results is as follows: C > A > D > E > B. This result is consistent with conductivity results, that is, proton conductivity is correlated with water mobility. A comparison of the $D(CH_{2,3})$ results yields no such pattern. The diffusivity of both the OH and $CH_{2,3}$ environments in the NP-PCM's showed very little increase in going from 333K to 363K and in some cases, the $CH_{2,3}$ diffusivity even decreased at the higher temperature. This reduction may be in part due to membrane dry out as the temperature increases despite the use of sealed NMR tubes. This dry out was more significant for NP-PCM's equilibrated in MeOH/ H_2SO_4 and EG/H_2SO_4. In any case, the very weak temperature dependence of the water diffusion coefficient (or equivalently, low activation energy) is surprising in view of the increase in conductivity, over the entire temperature range. For example, *Nafion* exhibits a strong correlation between water diffusivity and conductivity. This suggests that the Grotthuss or hopping mechanism of proton conductivity may play a significant role at elevated temperatures in these membranes.

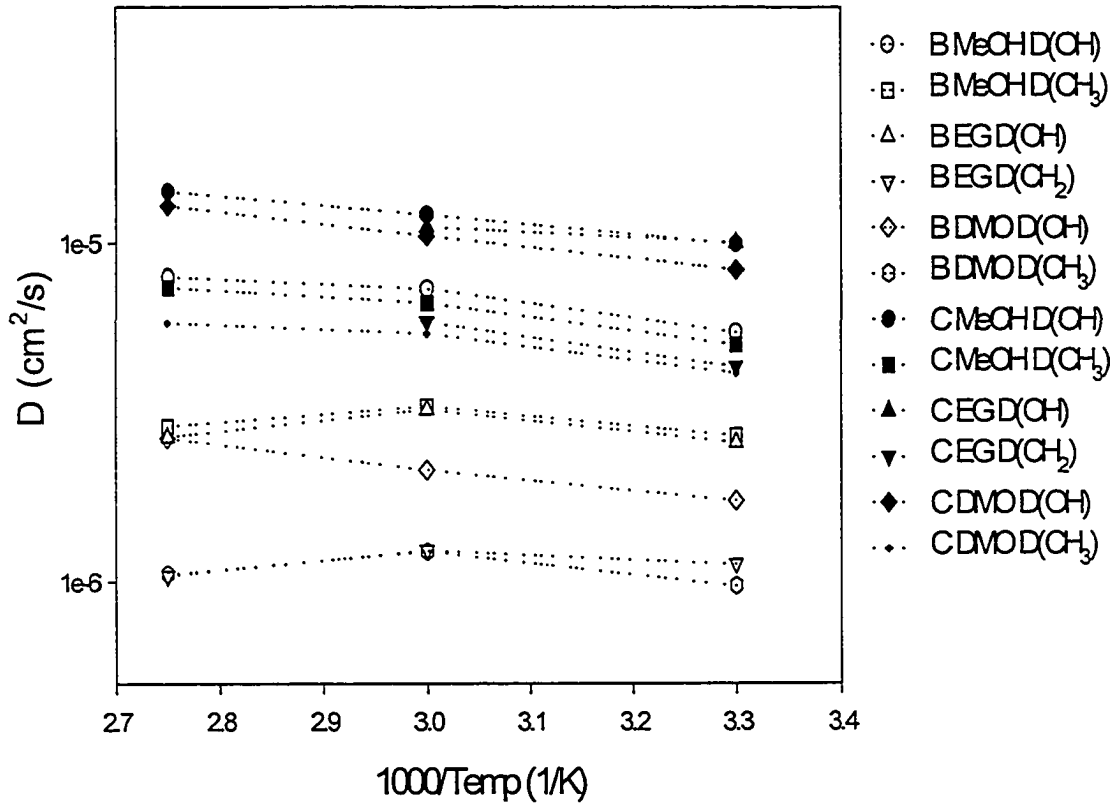

Figure 5-3. Proton D of NP-PCM membranes B and C as a function of temperature.

Table 5.1. NP-PCM's composition by volume and room temperature ionic conductivity.

NP-PCM	Ceramic	Ceramic Powder %	PVDF %	Porosity %	Conductivity RT (S/cm)
A	Aerosil 130	16	24	60	0.136
B	Aerosil 130	12	28	60	0.050
C	Aerosil 200	16	24	60	0.200
D	Aerosil 200	12	28	60	0.059
E	TiO_2	16	24	60	0.045

5.3. Uptake measurements

Solution uptake measurements given in Table 5.2, indicates greater uptake for membranes with higher ceramic concentration and greater surface area. The ceramic Aerosil 200 has a greater surface area than Aerosil 130, which when coupled with a greater concentration, may account for membrane C's greater solution uptake. Thus high water mobility and correspondingly ionic conductivity of the NP-PCM's is correlated with greater solution uptake. Of the three fuel/acid solutions, membranes equilibrated in DMO gave the highest solution weight uptake results, and yet these membranes exhibit the lowest diffusivity. This implies that DMO may be immobilized to a greater extent by the membrane structure and its larger size than EG and MeOH. It is suggested that this result of high uptake and reduced mobility may be due to the nature of the DMO molecule, which may lead to polarization effects between the DMO molecules and the membrane structure.

Table 5.2. Solution uptake results for NP-PCM's B and C at room temperature. Table entries are % weight uptake.

Aqueous Solutions	Membrane B	Membrane C
$MeOH/H_2SO_4$	11	16
EG/H_2SO_4	11	37
DMO/H_2SO_4	16	52

5.4 Selectivity Ratio results for NP-PCM's

In order to obtain more meaningful results with respect to DOFC concerns, we determined membrane selectivity as a function of temperature. Selectivity is defined as the ratio of $D(OH)/D(CH_{2,3})$. We can correlate the D(OH) with proton conductivity, while the $D(CH_3)$ is a direct measure of fuel permeability. A desirable PCM would have high selectivity indicating high proton conductivity and low fuel permeability. Selectivity results are arranged according to fuel type and are shown in Figures 5-4 (a) – (c). Of the five NP-PCM's, membrane B gave the most desirable result of high selectivity that increased with temperature. An interesting observation concerning the selectivity of membrane D is that depends strongly on fuel, increasing rapidly as a function of fuel molecular size. This could possibly be related to a particular pore size in membrane D that is just small enough to impede the DMO diffusion. However pore size in these materials have not been determined.

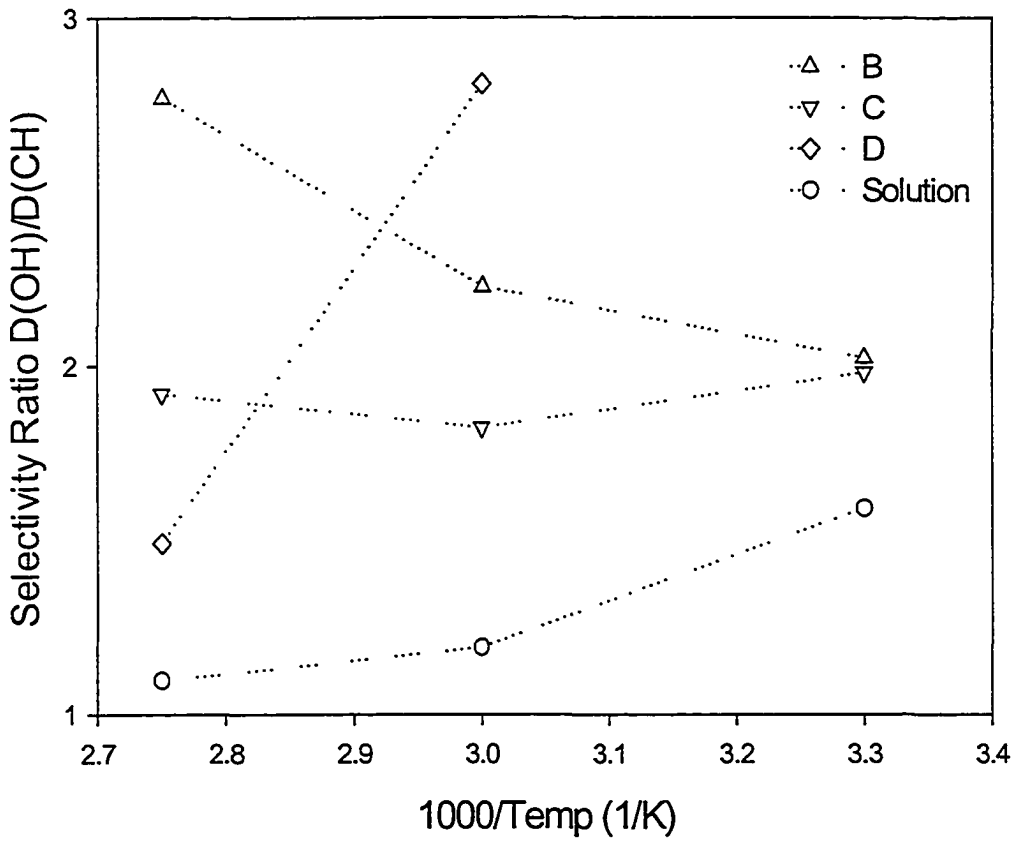

Figure 5-4 (a). Selectivity ratio of NP-PCM's equilibrated in aqueous 2M MeOH / 3 M H_2SO_4 solution.

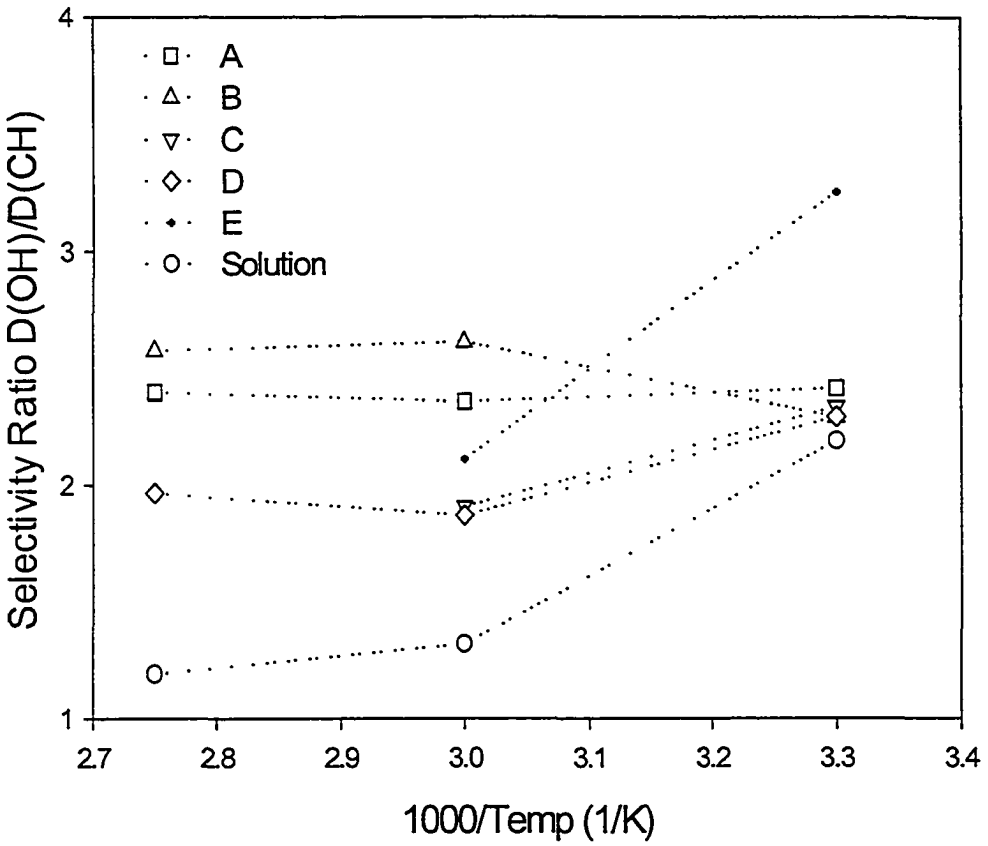

Figure 5-4(b). Selectivity ratio of NP-PCM's equilibrated in 2M EG / 3 M H_2SO_4 solution.

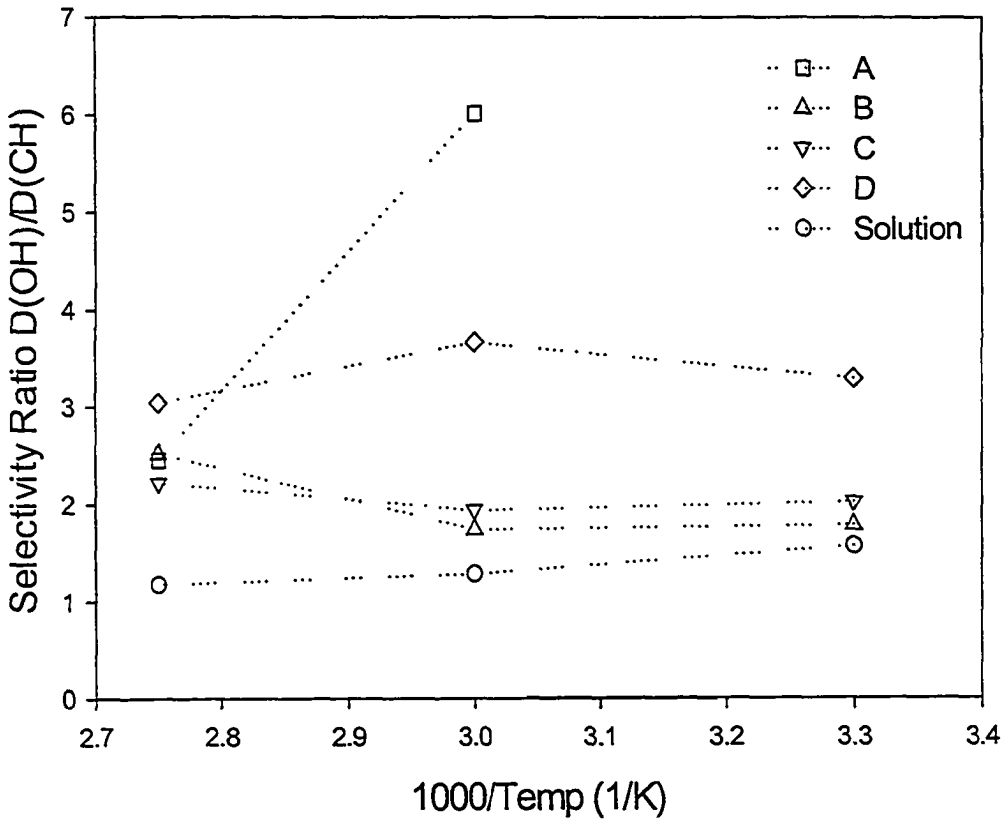

Figure 5-4(c). Selectivity ratio of NP-PCM's equilibrated in 2M DMO / 3 M H_2SO_4 solution.

5.5 Discussion

Water and fuel mobility in fuel/acid solutions and NM-PCM's equilibrated in these solutions were studied by PGSE NMR diffusion techniques. Based on these measurements, we have defined a selectivity criterion, $D(OH)/D(CH_{2,3})$, and of the five NP-PCM's, membrane B gave satisfactory results, namely high selectivity that increased with temperature, independent of fuel type. Membrane B did not have the highest D(OH) or conductivity, but it is suggested that selectivity may be a more relevant parameter for DOFC's. This awaits verification in fuel cell tests. The NP-PCM's exhibit significantly

lower activation energies for water diffusion than for conductivity, in contrast to *Nafion*, suggesting the Grotthuss mechanism may play a greater role in the former.

Chapter 6. Effect of Ceramic filler SiO_2 on $P(EO)_{20}LiBETI$

The purpose of this investigation was to study the effect of the ceramic filler SiO_2 on the transport properties of the PEO matrix. The system studied was $P(EO)_{20}LiN(SO_2CF_2CF_3)_2$ (otherwise known as $P(EO)_{20}LiBETI$) with and without the ceramic SiO_2. ^7Li and ^{19}F NMR was used to investigate the solvated cation and anion structure and dynamics over the temperature range of 20 - 100°C. These results were recently accepted for publication [57].

6.1 Spectra

^7Li and ^{19}F spectra from 20 – 100°C are shown in Figures 6-1 and 6-2, respectively. Both the filler-free and SiO_2 containing $P(EO)_{20}LiBETI$ spectra exhibit multiple components for both nuclei, which become more resolved as the temperature increases. A minor reduction in the ^7Li and ^{19}F linewidths of both polymers is observed as the temperature increases, indicating modestly increasing mobility. The addition of the filler to the polymer electrolyte induces changes in the lithium and fluorine environments as is evident by the differences observed in the ^7Li and ^{19}F NMR spectra of Figures 6-1 and 6-2. The ^7Li spectra for both polymers show only the central transition, indicating motional narrowing due to the fast Li-ion diffusion. The ^7Li spectra for the filler-free polymer electrolyte undergo somewhat less motional narrowing compared with the SiO_2 containing material, as the temperature increases.

The ^{19}F spectra for the SiO_2 containing polymer exhibit smaller linewidths at all temperatures compared with the filler-free polymer. The SiO_2 containing polymer spectra also show multi-components that become more resolved at higher temperatures.

This may be due to a combination of greater segmental mobility and a reduction in the heteronuclear dipole-dipole interactions between the fluorine and the polyether protons, caused by the interaction of the SiO_2 with the polymer matrix. This is supported by ^1H linewidth data in which the SiO_2 containing polymer had a more reduced linewidth compared with the filler-free polymer at 20°C.

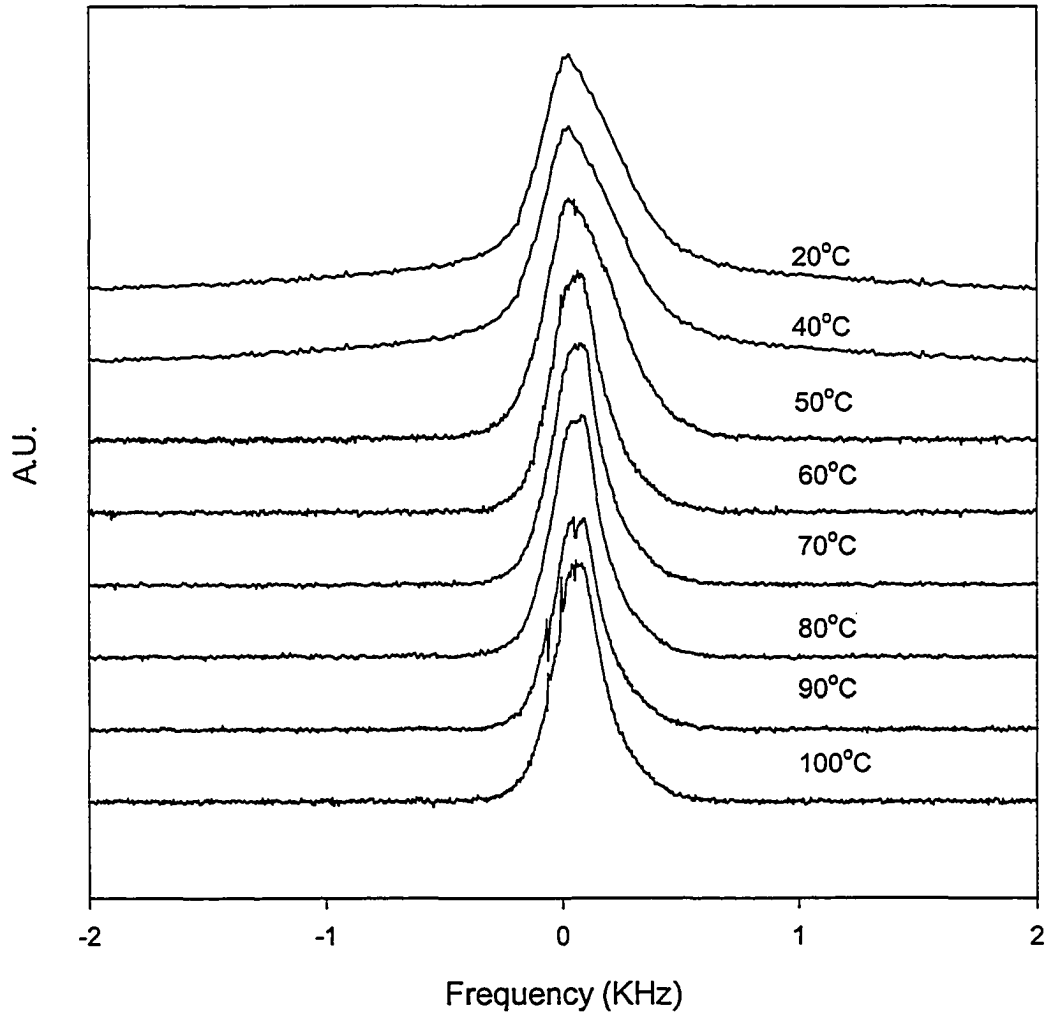

Figure 6-1 (a). ^7Li single pulse NMR spectra vs. temperature of filler-free $P(EO)_{20}LiBETI$ polymer electrolyte from 20 – 100°C.

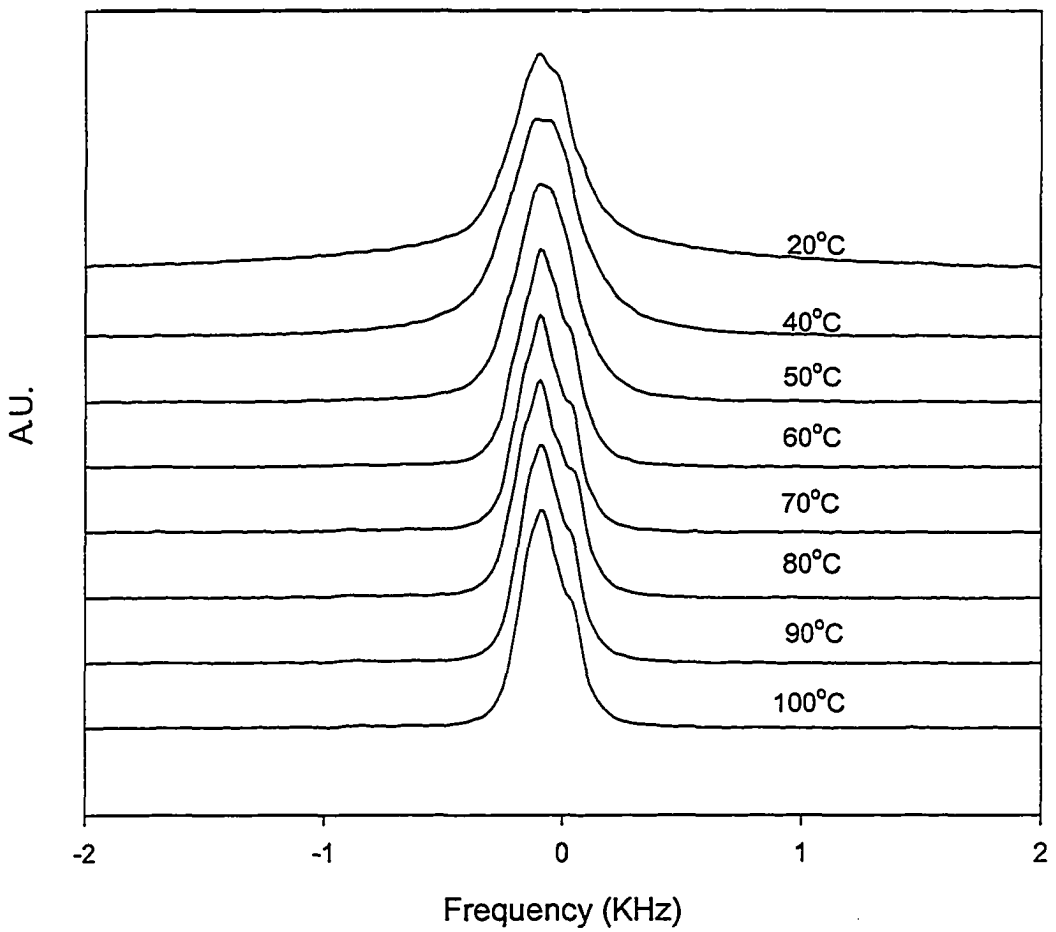

Figure 6-1 (b). ^{7}Li single pulse NMR spectra vs. temperature of 10% wt. SiO_2 $P(EO)_{20}LiBETI$ polymer electrolyte from 20 – 100°C.

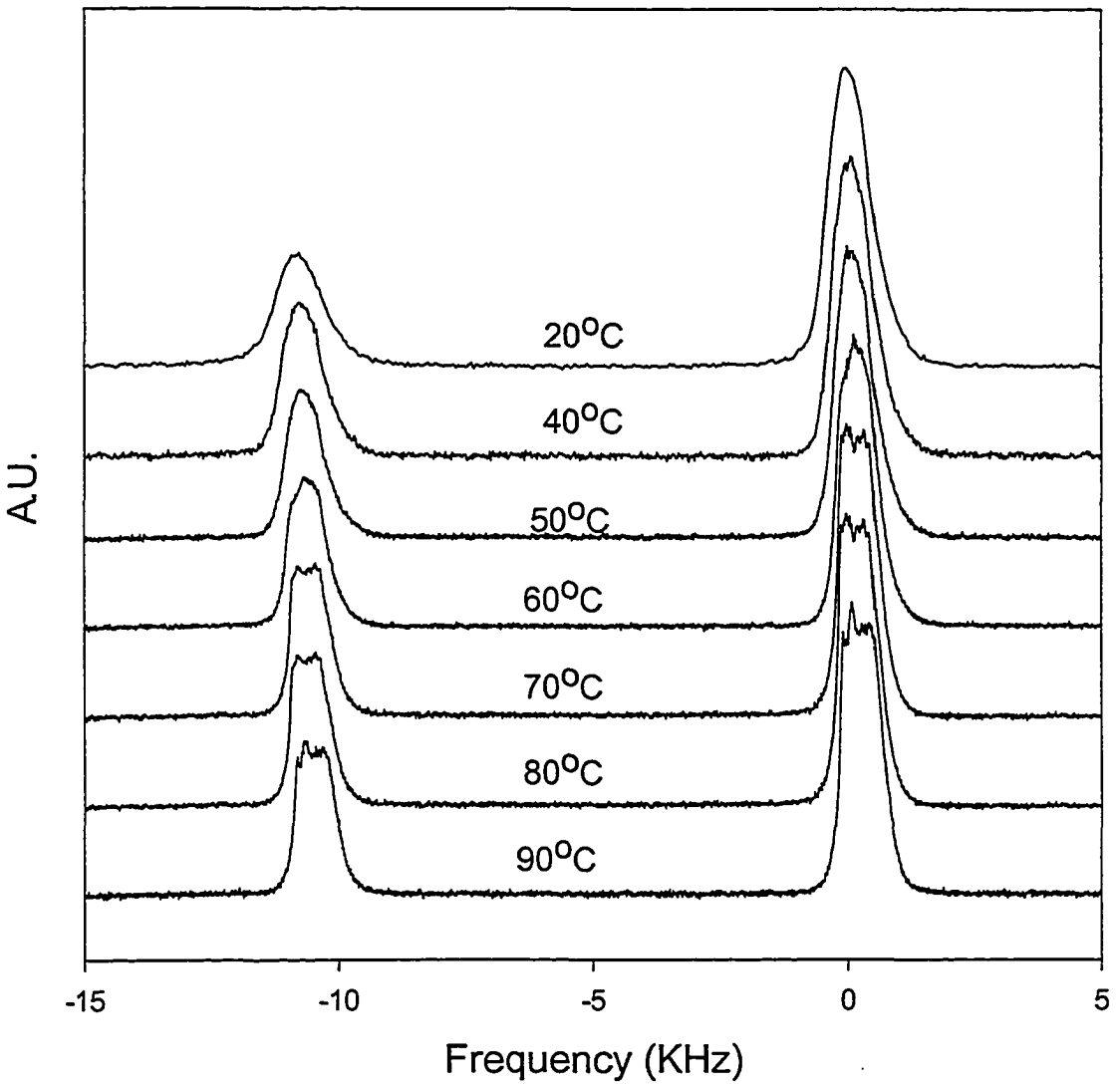

Figure 6-2 (a). ^{19}F NMR quadrupolar echo of filler-free $P(EO)_{20}LiBETI$ polymer electrolyte from 20 – 90°C.

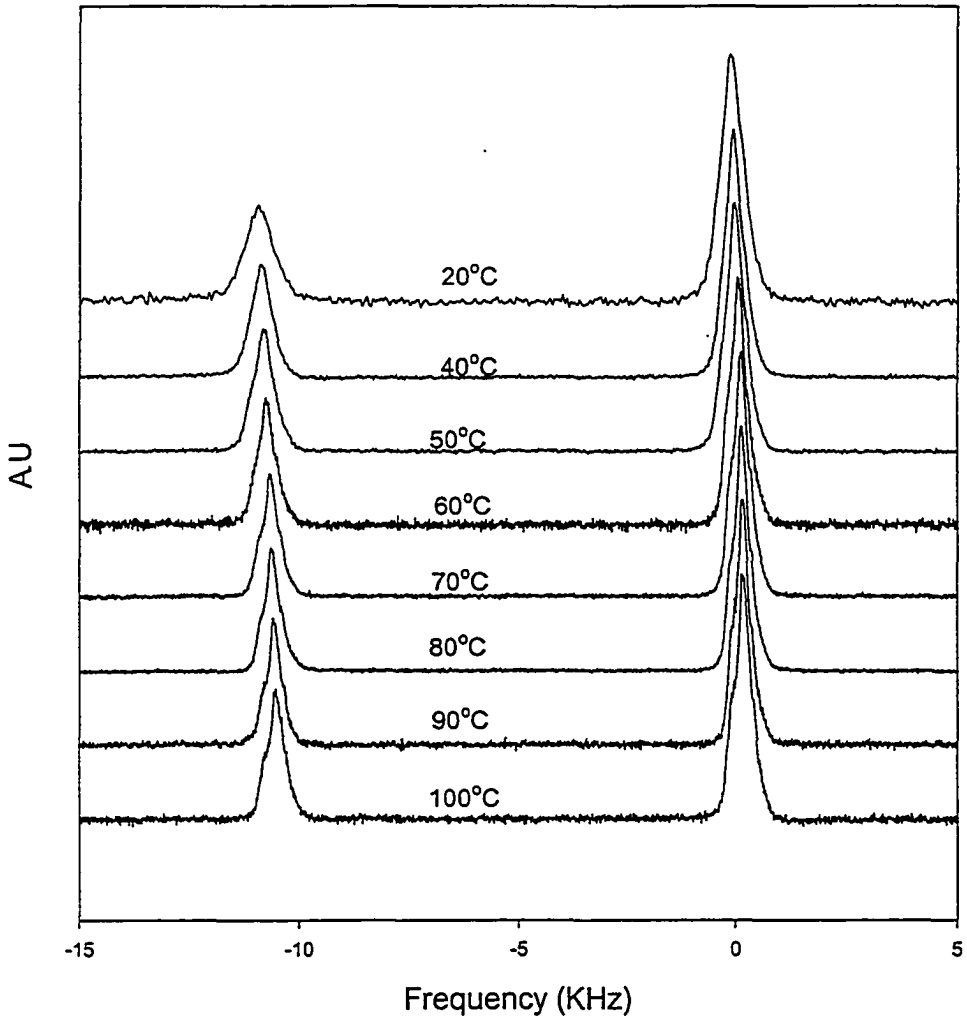

Figure 6-2 (b). ^{19}F NMR quadrupolar echo of 10% wt. SiO_2 $P(EO)_{20}LiBETI$ polymer electrolyte from 20 – 100°C.

6.2 T_1's

Arrhenius plots of the ^{7}Li and ^{19}F T_1's are displayed in Figure 6-3. Whereas the ^{7}Li T_1's show a broad minimum for both the filler-free and SiO_2 containing polymers, the ^{19}F T_1's do not. The T_1 minimum occurs when the motional correlation time is comparable to the inverse of the Larmor angular frequency. A broad T_1 minimum

indicates a distribution of correlation times, indicating the heterogeneity of the local environment, a feature that is characteristic in amorphous systems [50]. An alternative explanation of the T_1 minimum in the very special case of heterogeneous PEO complexes is that it happens to occur at around the DSC-determined melting point of the uncomplexed PEO in the materials. However this does not invalidate the use of the T_1 data above the minimum to extract an activation energy for short range Li motion (discussed shortly) or to provide at least an estimate for the motional correlation time.

The ^{19}F T_1's for the CF_3 and CF_2 environments of both polymers show a similar temperature dependence. The longer ^{19}F T_1's are assumed to occur in the motionally narrowed regime, above the T_1 minimum (which is believed to occur below the experimental temperature range in this investigation), and are an indication of less restricted motion, compared with the ^7Li environment. The T_1's of the CF_3 for both polymers are longer than that of the CF_2. This is attributed to the rotation of the CF_3 group, which averages the local fields, thereby reducing their effect and thus increasing the T_1's. The slightly longer ^{19}F T_1's for SiO_2 containing polymer correlates with the reduction in linewidth, again signifying the increase in anionic mobility in the SiO_2 containing sample. Activation energies calculated from best-fit regression lines for both ^7Li (above the T_1 minimum) and ^{19}F are listed in Table 6.2, and both are somewhat lower for the SiO_2 containing sample.

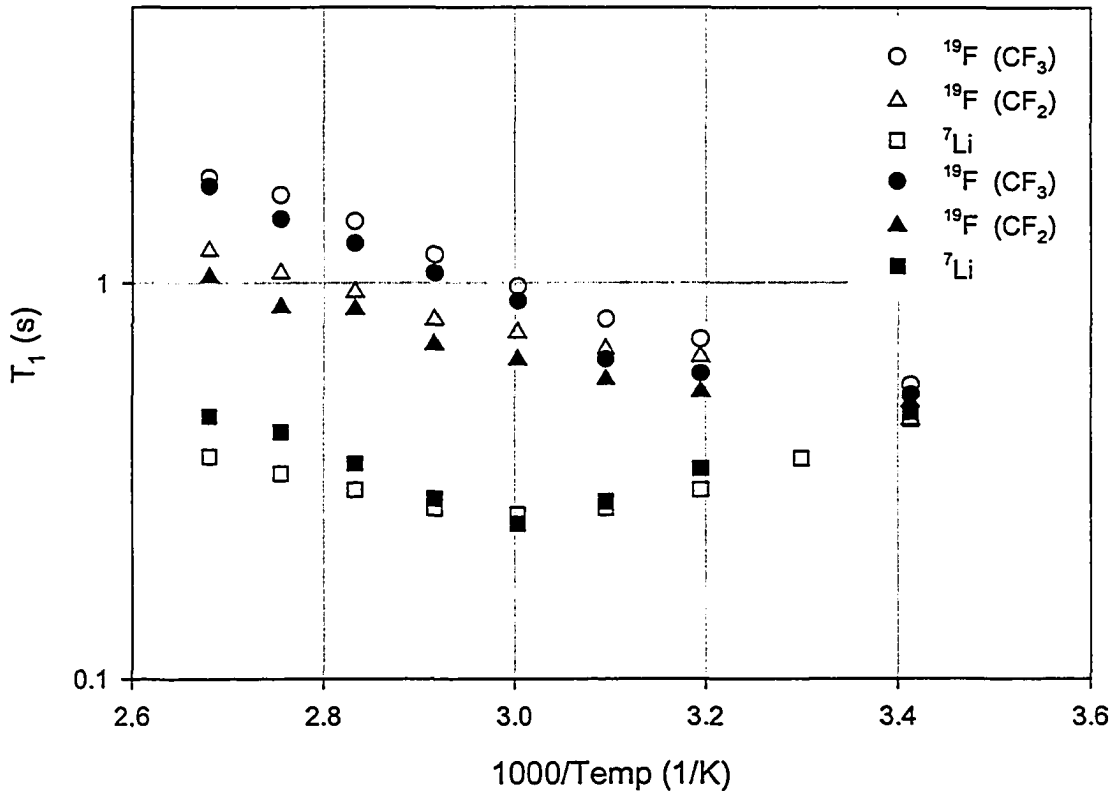

Figure 6-3. T_1 vs. temperature of filler-free (solid markers) and 10% wt. SiO_2 (empty markers) $P(EO)_{20}LiBETI$ polymer electrolytes.

6.3 D

Figure 6-4 is an Arrhenius plot of the ^{7}Li and ^{19}F self-diffusion coefficients for the filler-free and the 10 wt.% SiO_2-containing $P(EO)_{20}LiBETI$ polymer electrolytes. In the case of the ^{19}F nucleus the diffusion coefficient was evaluated for both peaks. No substantial differences were detected, however, both measurements are reported in Figure 6-4.

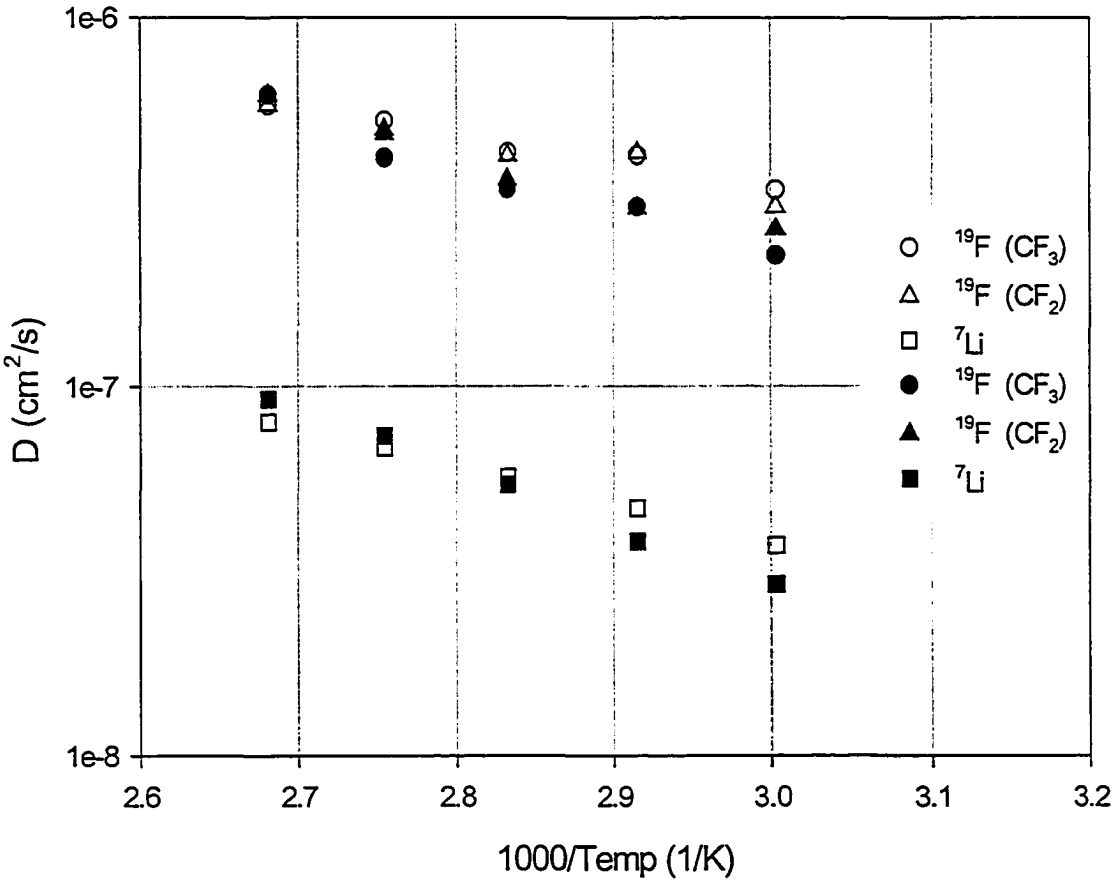

Figure 6-4. D vs. temperature of filler-free (solid markers) and 10% wt. SiO_2 (empty markers) $P(EO)_{20}$LiBETI polymer electrolytes.

As found in the PEO-LiTFSI polymer electrolyte system [51], where TFSI (bis(trifluoromethansulfonyl)imide; $(SO_2CF_3)_2N^-$) is the lighter homologue of BETI, the diffusion coefficient of the anion is larger than the one of the cation at any temperature and EO/Li ratio. This is because the cations are tightly bound to the PEO segments, thus their motion is more restricted than that of the anion.

The lithium diffusion coefficients of the filler-free and the SiO_2-containing polymer electrolytes show approximately Arrhenius behaviour and, most importantly, the presence of the filler leads to no substantial differences in values. However, close examination of the data in Figure 6-4 does reveal small differences between the filler-free and SiO_2 – containing samples at lower temperatures, with the latter being somewhat higher. This is probably due to a higher degree of disorder induced by the presence of the filler particles, whereby higher temperature behaviour is "frozen in" at lower temperature. An alternative and nearly equivalent explanation is that the filler-containing polymer electrolyte exhibits a somewhat lower activation energy than the filler-free one. The latter scenario is also consistent with a more disordered Li environment. The Arrhenius behaviour of the Li diffusion coefficient with temperature was also reported for $P(EO)_{20}LiTFSI$, using a lower molecular weight PEO, by Gorecki et al [51], however, they reported a D_{Li} that is a factor of three higher than the values measured in this work. Nevertheless, in very recent work on high MW $P(EO)_nLiTFSI$ polymer electrolytes, Oradd et al. [52] have reported a D_{Li} (at 85°C) very close to our results.

The fluorine diffusion coefficients also display approximately Arrhenius behaviour, although the fits to a single slope (activation energy) are not as satisfactory as for ^7Li. The diffusion coefficients of the SiO_2-containing sample are slightly higher than those of the filler-free material, which correlates with both the T_1 and linewidth data. Overall, the D_F values are closer to the values previously reported for $P(EO)_{20}LiTFSI$ [20, 21].

Activation energies calculated from the ^7Li and ^{19}F diffusion plots are listed in Table 6.2. Comparison with measured activation energies for the ionic conductivity [22]

is problematic at this time because of the significant change in the apparent value occurring above the uncomplexed PEO melting point. The activation energies for diffusion are somewhat higher than for spin-lattice relaxation, which is a consequence of the vastly different (~5 – 7 orders of magnitute) length and time scales probed by the two kinds of measurements. However it is noted that the presence of the filler results in lower activation energies for diffusion as well as for T_1.

From the D_{Li} and D_F values the ionic conductivity of the polymer electrolytes was calculated using the Nernst-Einstein equation:

$$\sigma_c = Ne^2(D_{Li} + D_F)/kT$$

where N is the number of cations per unit volume

$$N = N_A/V_M.$$

V_M, the molar volume of the polymer electrolyte, is given by the ratio of the $P(EO)_{20}LiBETI$ weight per cm^3 (see Table 1) and its composite molecular weight ($nMW_{PEO} + MW_{LiBETI}$=1267)

Table 6.1. Picnometric and calculated densities and composition of filler-free and SiO_2-containing polymer electrolytes. The picnometric density of fumed silica is also reported.

	$P(EO)_{20}LiBETI$	$P(EO)_{20}LiBETI$ - 10 wt% SiO_2	SiO_2
Picnometric density (gcm^{-3})	1.349	1.386	2.168
Calculated density (gcm^{-3})	-	1.397	-
PEO, wt%	69.5	63.1	-
LiBETI, wt%	30.5	27.8	-
SiO_2, wt%	-	9.1	-

Table 2. ^{7}Li and ^{19}F activation energies (eV) for the filler-free and SiO_2-containing $P(EO)_{20}LiBETI$ polymer electrolytes.

	From T_1 (eV)	**From D (eV)**	
$P(EO)_{20}LiBETI$	**^{7}Li - 0.176** **^{19}F - 0.154**	**^{7}Li - 0.320** **^{19}F - 0.215**	
$P(EO)_{20}LiBETI$ – 10 wt% SiO_2	**^{7}Li - 0.094** **^{19}F - 0.110**	**^{7}Li - 0.207** **^{19}F - 0.168**	

In Figure 6-5 are reported the calculated ionic conductivity (σ_c) values obtained for the filler-free and the 10 wt.% SiO_2-containing $P(EO)_{20}$LiBETI polymer electrolytes. For comparison, the ionic conductivity of the materials measured by A.C. impedance (σ_m) [22] is also reported in the figure. The comparison clearly shows that σ_m is always smaller than σ_c at all temperatures, with or without the presence of the filler. This deviation may be explained in terms of the validity of the Nernst-Einstein equation being applied to the polymers in our study. The premise of the Nernst-Einstein equation is that of unbounded motion within a single-phase medium. Clearly from the difference between σ_m and σ_c, this is not the case in our systems.

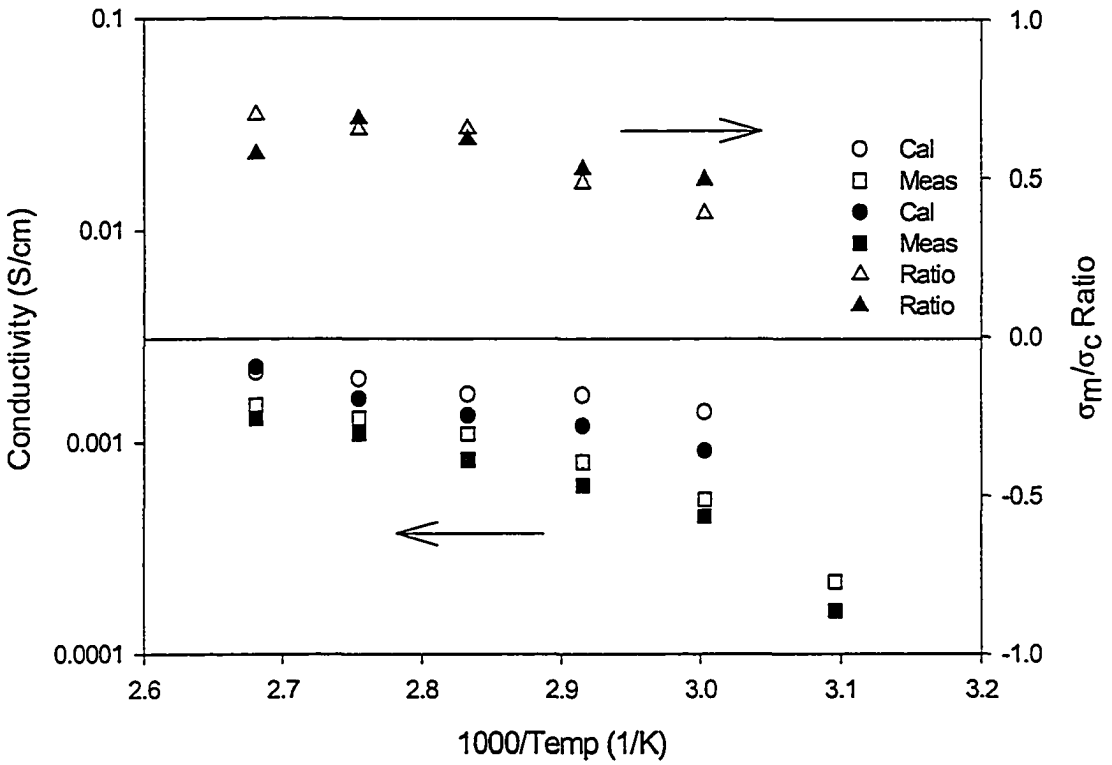

Figure 6-5. Ionic conductivity vs. temperature of filler-free (solid markers) and 10% wt. SiO_2 (empty markers) $P(EO)_{20}$LiBETI polymer electrolytes.

The σ_m/σ_c ratio ranged from 0.2 at 50°C to about 0.7 at 80°C and higher. Lower than unity σ_m/σ_c ratios have been reported by Gorecki et al. [51] for $P(EO)_n$LiTFSI and Williamson et al. [53] for the tetraglyme-$LiCF_3SO_3$ system. In both works this deviation is attributed to the correlated motions of anions and cations in neutral pairs, which contribute to the diffusion but do not contribute to the conductivity. However, it is important to note that Williamson et al [53] reported that the σ_m/σ_c ratio increases with temperature, which correlates somewhat our results (see Figure 6-5). The σ_m/σ_c for the SiO_2 containing polymer shows a modest increase with temperature, while that of the

filler-free polymer decreases above 90°C. This can be interpreted assuming that the conductivity in our system is more strongly correlated with the thermally increased local motion of the entangled polymer segments coordinating the Li^+ ions and overall chain motion than to the increased ion-pairing induced by increasing temperatures. As a matter of the fact, Edman [54] reported an almost negligible increase of the ion-pairing in $P(EO)_nLiTFSI$ ($n \geq 8$) with increasing temperature from 22°C to 70°C. In addition, the extent of the ion-pairing reported in amorphous $P(EO)_{20}LiTFSI$ at the highest temperature (70°C) was lower than 10%.

The validity of this interpretation is supported by the dependence of the fluorine self-diffusion coefficients on the gradient delay (Δ), as shown in Figure 6-6 for the filler-free polymer at both 90 and 100°C. The self-diffusion shows a dependence on Δ at both temperatures over the time scale studied. However, this dependence is greater at 90 than at 100°C. The ^7Li diffusion coefficients were also found to depend somewhat on Δ, but the fluorine diffusion results are more relevant considering the larger anionic conductivity of these materials. In an unbounded single-phase medium, D should not depend on Δ, but in heterogeneous media such a dependence on Δ is an indication of restricted motion over the length scale probed. [55] Thus at 100°C the motion is less restricted than at 90°C, and the D-value at the higher temperature is more representative of long-range transport.

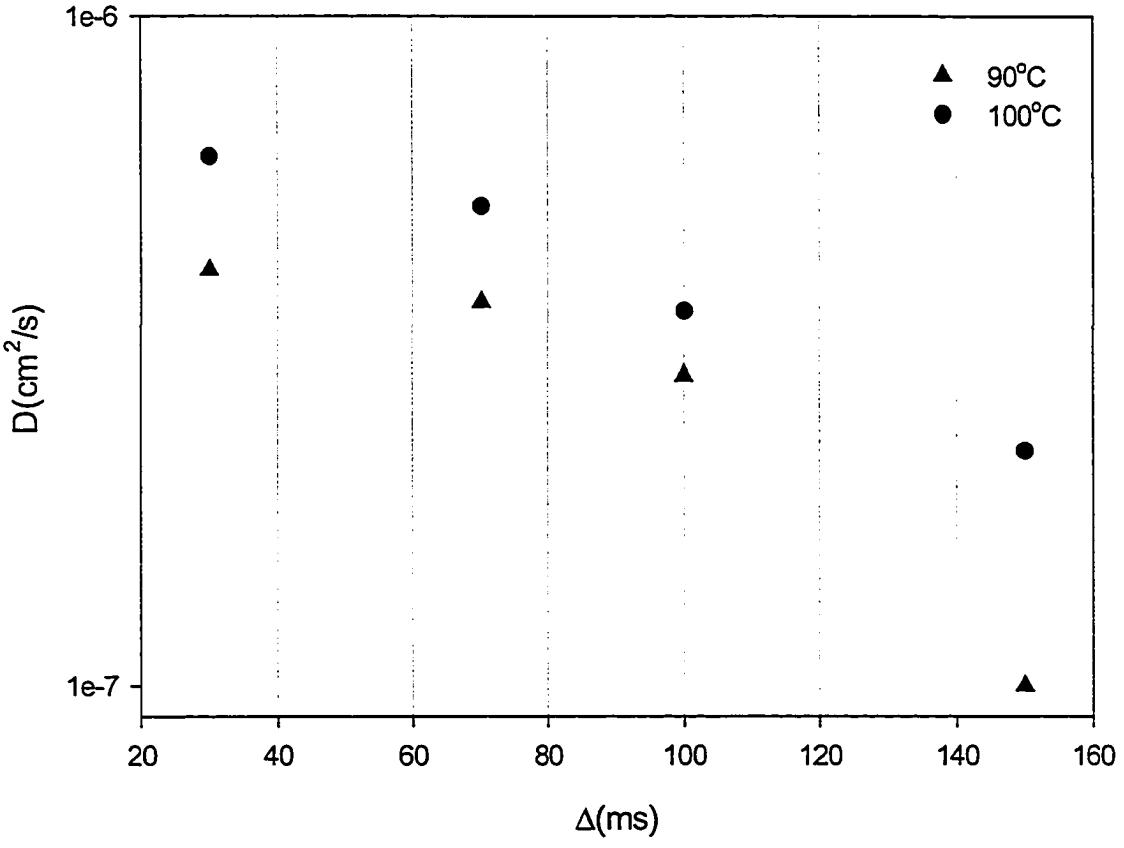

Figure 6-6. ^{19}F D vs. gradient delay for the filler-free $P(EO)_{20}LiBETI$ polymer electrolyte at two different temperature (90 and 100°C).

6.4 Conclusions

Both cation and anion mobility in $PEO_{20}LiBETI$ polymer electrolytes prepared by a solvent-free method were investigated by NMR methods over different length scales probed by spin-lattice relaxation and self-diffusion measurements. Of particular interest in this study is the effect of nanosized SiO_2 on the ion transport properties. It was found that the presence of filler does have a modest effect on both cation and anion mobility, somewhat more so for the latter. The main effect appears to be a slight decrease of

diffusion and relaxation activation energies in the filler-containing material. However the conductivity and diffusivity enhancement observed in this investigation is much less significant than reported by other work in which the polymer electrolytes were prepared by casting from solvents.

Finally, the difference between ionic conductivity calculated by the Nernst-Einstein equation and the measured value generally decreases with increasing temperature, especially for the filler-containing material. This difference is therefore attributed to variable length scale diffusion within a heterogeneous medium, rather than ion pairing effects. At higher temperatures the medium becomes less heterogeneous and the ions are less restricted.

Chapter 7. References

1. R.J. Gillespie and T.E. Peel, *Adv. Phys. Org. Chem. 9, 1 (1972).*
2. L.P. Hammett, and A.J. Deyrup, *J. Am. Chem. Soc. 54, (1932) 2721.*
3. G.A. Olah and G.K. Surya Prakash, Superacids, *John Wiley and Sons*, 1985, *Chapter 2.*
4. D.D. DesMarteau, *Science Magazine, Vol. 289, No. 5476, (2000) 72-73.*
5. J. Burgess, Metal Ions in Solution, *John Wiley and Sons, 1978, Chapter 2.*
6. T.D. Gierke, *152nd Meeting of the Electrochemical Soc., Atlanta, 1977, Abstract No. 438, J. Electrochemic. Soc., Vol. 124, No. 8, 319C (1977).*
7. R.S. Yeo and A. Eisenberg, *Polymer Preprints 16 (1975) 104-110.*
8. M. Falk, *Can J. Chem. 58 (1980) 1495-1501.*
9. G. Merisi, Y. Wang, A. Bandis, P.T. Inglefield, A.A. Jones and W.Y. Wen, *Polymer, Vol. 42, (2001) 6153-6160.*
10. E. Peled, T. Duvdevani and A. Melman, *Electrochemical and Solid State Letters. 1(5), 210 (1998).*
11. E. Peled, T. Duvdevani and A. Melman, *Electrochemical and Solid State Letters. 3(12), (2000) 525.*
12. E. Peled, T. Duvdevani, and A. Melman, *Electrochemical and Solid State Letters, Vol. 4(4), (2001) A38.*
13. J.E. Weston and B.C.H. Steel, *Solid State Ionics, Vol. 7, (1982) 75.*
14. M.C. Borghini, M. Mastragostino, S. Passerini and B. Scrosati, *J. Electrochem. Soc., Vol. 142, (1995) 2118.*

15. F. Croce, L. Persi, B. Scrosati, F. Serraino-Fiory, E. Plichta and M.A. Hendrickson, *Electrochim. Acta, Vol. 46, (2001) 2457.*

16. G.B. Appectecchi, F. Croce, L. Persi, F. Ronci and B. Scrosati, *Electrochim. Acta, Vol. 45, 1481 (2000).*

17. S.H. Chung, Y. Wang, L. Persi, F. Croce, S.G. Greenbaum, B. Scrosati and E. Plichta, *J. Power Sources, Vol. 97-98, (2001) 644.*

18. F. Croce, G.B. Appetecchi, L. Persi and B. Scrosati, *Nature, Vol. 394, (1998) 456.*

19. Capiglia, P. Mustarelli, E. Quartarone, C. Tomasi and A. Magistris, *Solid State Ionics, Vol. 118, (1999) 73.*

20. H.J. Walls, J. Zhou, J.A. Yerian, P.S. Pedkiw, S.S. Khan, M.K. Stowe and G.L. Baker, *J. Power Sources, Vol. 89, (2000) 156.*

21. Y. Liu, J.Y. Lee and L. Hong, *J. Power Sources, Vol. 109, (2002) 507.*

22. J.H. Shin and S. Passerini, *J. Electrochem. Soc., (2003) submitted.*

23. G.B. Appetecchi, F. Croce, J. Hassoun, B. Scrosati, M. Salomon and F. Cassel, *J. Power Sources, Vol. 114,(2003) 105.*

24. K.D. Kreuer, *Solid States Ionics, Vol. 94, (1997) 55.*

25. V.B.Kazansky, *Topics in Catalysis, Vol. 11/12, (2000) 55.*

26. A.A. Kornyshev, A.M. Kuznetsov, E. Spohr, and J. Ulstrup, *J. Phys. Chem. B, Vol. 107, (2003) 3351.*

27. S.J. Paddison, L.R. Pratt, T.Zawodzinski, and D.W. Reagor, Fluid Phase Equilibria, Vol. 150-151, (1998) 235.

28. N. Agmon, *Chemical Physics Letters, Vol. 244, (1995) 456.*

29. K.D. Kreuer, *Chem. Mater. Vol. 8, (1996) 610.*

30. K.D. Kreuer, W. Weppner, A. Rabenau, *Angew. Chem. Int. Ed. Engl., Vol. 21, (1982) 208.*

31. C. J. D. van Grotthuss, *Ann. Chim. (Paris) Vol. 58, (1806) 54.*

32. J.D. Bernal, R.H. Fowler, J. *Chem. Phys., Vol. 1, (1933) 515.*

33. W.L. Jorgensen, *J. Chem. Phys., Vol. 77, (1982) 4156.*

34. G.E. Walrafen, M.R. Fisher, M.S. Hokmabidi, W.-H. Yang, *J. Chem. Phys., Vol. 85, (1986) 6970.*

35. M.E. Tuckerman, K. Laasonen, M. Sprike, M. Parrinello, *J. Chem. Phys., Vol. 103, (1995) 150.*

36. M.E. Tuckerman, D. Marx, M.L. Klein, M. Parrinello, *Science, Vol. 275, (1997) 817.*

37. Y.K. Lau, and P. Kebarle, *J. Am. Chem. Soc., Vol. 104 (1982) 1462.*

38. E. Fukushima, S.B. Roeder, Experimental Pulse NMR: A Nuts and Bolt Approach, *E. Fukushima ed., Addison-Wesley Longman, 1981.*

39. C.P. Slichter, Principles of Magnetic Resonance, *Springer Verlag, 1990.*

40. A. Abragam, Principles of Nuclear Magnetism, *Oxford University Press, 1961.*

41. J. R. Macdonald, Impedance Spectroscopy, *John Wiley and Sons, New York, 1987.*

42. E.L. Hahn, *Phys. Rev., Vol. 80, (1950) 580.*

43. E.O. Stejskal, J.E. Tunner, *J. Chem. Phys.Vol. 42, (1965) 288.*

44. E.O Stejskal, *J. Chem. Phys., Vol. 43, (1965) 3597.*

45. S.J.Paddison, *J. New. Mater. Electrochem. Sys., Vol. (2001)* .

46. M. Eikerling, S.J.Paddison, T.A. Zawodzinski Jr, Preprint, publication in transit.

47. H. Chakrabarti, *J. Phys.:Condens. Matter, Vol. 8, (1996) 7019.*

48. T. Dippel and K.D. Kreuer, *Solid State Ionics, Vol. 46, (1991) 3.*

49. A.K. Lyashchenko, *J. Molecular Liquids, Vol. 91, (2001) 21.*

50. D.R. Uhlmann, N.J.Kreidl, ed., Glass: Science and Technology, *Vol. 4B., Academic Press, 1990, p. 100.*

51. W. Gorecki, M. Jeannin, E. Belorizky, C. Roux, and M. Armand, *J. Phys.: Condens. Matter. Vol. 7, (1995) 6823.*

52. G. Oradd, L. Edman, A. Ferry, *Solid State Ionics Vol. 152-153, (2002) 131.*

53. M.J. Williamson, J.P. Southall, H.V.St.A. Hubbard, S.F. Johnston, G.R. Davies and I.M. Ward, *Electrochim. Acta Vol. 43, (1998) 1415.*

54. L. Edman, *J. Phys. Chem. B Vol. 104, (2000) 7254.*

55. A. Reiche, A. Weinkaupf, B. Sandner, F. Rittig, and G. Fleischer, Electrochim. Acta, Vol. 45, (2000) 1327.

56. S. Suarez, S.H. Chung, S. Greenbaum, S. Bajue, E. Peled and T. Duvdevani, *Electrochim. Acta, Vol. 48, (2003) 2187.*

57. S. Suarez, S. Abbrent, S.G. Greenbaum, J.H. Shin and S. Passerini, *Solid State Ionics, awaiting publication.*